Chaotic Modeling and Simulation (CMSIM) 2: 303–310, 2012

Peculiarities of Transition to Chaos in Nonideal Hydrodynamics Systems

A. Yu. Shvets[1] and V. A. Sirenko[2]

[1] National Technical University of Ukraine "KPI", Kyiv, Ukraine
(E-mail: `alex.shvets@bigmir.net`)
[2] National Technical University of Ukraine "KPI", Kyiv, Ukraine
(E-mail: `sir_vasiliy@ukr.net`)

Abstract. The nonideal deterministic dynamic system "tank with a fluid–electromotor" is considered. On the basis of investigation of low-dimensional mathematical model of the given system the map of dynamic regimes is constructed. The study of scenarios of transition to deterministic chaos is carried out. Atypical peculiarities of realization of such scenarios are described.
Keywords: nonideal system, regular and chaotic attractor, scenario of transition to chaos.

1 Introduction

Many of modern machines, mechanisms and engineering devices in the capacity of constructive elements contain the cylindrical tanks partially filled with a fluid. Therefore investigation of oscillations of free surface of a fluid in cylindrical tanks is one of the main problems in hydrodynamics throughout last decades [1]. Since seventieth years of past century were constructed, so-called, "low–dimensional" mathematical models describing such oscillations [2]–[5]. The "low-dimensional" models allow to obtain adequate enough describing of a problem in cases, when power of source of excitation of oscillations considerably exceeds a power consumed by an oscillating loading (a tank with a fluid). These cases are defined as ideal in sense of Sommerfeld–Kononenko [6]. However, in real practice, the power of source of excitation of oscillations more often is comparable with a power which consume the oscillating loading. These cases are called as nonideal in sense of Sommerfeld–Kononenko. In these cases it is necessary to consider interacting between a source of excitation of oscillations and oscillating loading, that leads to essential correction of mathematical models which applied in ideal cases [7]–[9].

Nonideal, in sense of Sommerfeld–Kononenko, dynamic system "tank with a fluid–electromotor" in case of horizontal excitation of a platform of tank are considered in the given article. Investigations of such systems have been begun in work [10], where the mathematical model of such systems has been

Received: 21 July 2011 / Accepted: 31 March 2012

ISSN 2241-0503

constructed for the first time. In such model the interacting between a source of excitation of oscillations and a tank with fluid were taken into account.

The main goals of this work is detection of new peculiarities of transition to the deterministic chaos in systems "tank with a fluid–electromotor".

2 Mathematical model of hydrodynamic system "electric motor–the tank with fluid"

Let's consider rigid cylindrical tank partially filled with a fluid. We will assume that the electric motor of limited power excite horizontal oscillations of platform of tank (fig. 1). The given hydrodynamic system is typical nonideal, in sense of Sommerfeld–Kononenko [6], deterministic dynamic system. As shown in [7]–[9] mathematical model of system "tank with a fluid–electric motor" may be described by following system of differential equations:

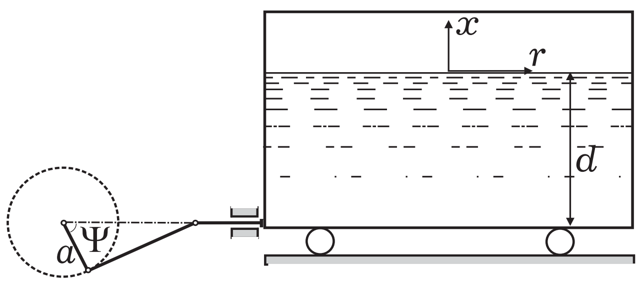

Fig. 1. The scheme of the system

$$
\begin{aligned}
\frac{dp_1}{d\tau} &= \alpha p_1 - [\beta + \frac{A}{2}(p_1^2 + q_1^2 + p_2^2 + q_2^2)]q_1 + B(p_1 q_2 - p_2 q_1)p_2;\\
\frac{dq_1}{d\tau} &= \alpha q_1 + [\beta + \frac{A}{2}(p_1^2 + q_1^2 + p_2^2 + q_2^2)]p_1 + B(p_1 q_2 - p_2 q_1)q_2 + 1;\\
\frac{d\beta}{d\tau} &= N_3 + N_1\beta - \mu_1 q_1;\\
\frac{dp_2}{d\tau} &= \alpha p_2 - [\beta + \frac{A}{2}(p_1^2 + q_1^2 + p_2^2 + q_2^2)]q_2 - B(p_1 q_2 - p_2 q_1)p_1;\\
\frac{dq_2}{d\tau} &= \alpha q_2 + [\beta + \frac{A}{2}(p_1^2 + q_1^2 + p_2^2 + q_2^2)]p_2 - B(p_1 q_2 - p_2 q_1)q_1.
\end{aligned}
\tag{1}
$$

The system (1) is nonlinear system of differential equations of fifth order. Phase variables p_1, q_1 and p_2, q_2, accordingly amplitudes of dominant modes of oscillations of free surface of fluid. The phase variable β is proportional to velocity of rotation of shaft of the electric motor. There are six parametres

$A, B, \alpha, N_1, N_3, \mu_1$ of system (1), which are defined through physical and geometrical characteristics of tank with a fluid and electric motor. α – coefficient of forces of a viscous damping; N_1, N_3 – parameters of static characteristics of the electric motor; μ_1 – coefficient of proportionality of the vibrating moment; A and B–the constants which sizes depend on diameter of a tank and depth of filling with its fluid.

In works [7]–[9] existence of the deterministic chaos in system (1) has been proved, some types of chaotic attractors are classified and shown that chaotic attractors are typical attractors of the given system. We will notice that the detailed and all-round study of chaotic dynamics of system (1) is possible only by means of a series of numerical methods and algorithms. The technique of carrying out of such researches is described in works [7]–[9], [11].

3 Numerical research of dynamic regimes

Let's begin our investigations by construction the map of dynamic regimes of system. The map of dynamic regimes represents the diagram in a plane, on which coordinate axes values of two parameters of system are marked and various colors (color shades) ploted areas of existence of the various steady-states dynamic regimes. The technique of construction the map of dynamic regimes is described in [8].

In fig. 2 the map of dynamic regimes of system "tank with a fluid–electromotor" constructed in regard to parameters N_3 and α is presented at values $A = 1.12; B = -1.531; \mu_1 = 0.5; N_1 = -1$.

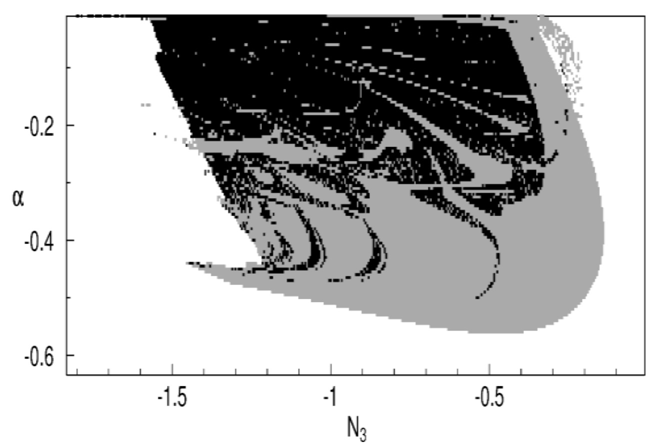

Fig. 2. The map of dynamic regimes of system.

In the received sheet of a map (fig. 2) areas of three various types of dynamic regimes are ploted. Areas of values of parameters N_3, α in which equilibrium position will be the steady-state regime of system are ploted by white color. Gray color corresponds the areas of values of parameters N_3, α at which limit cycles will be the steady-state regimes of system. At last, areas in which the steady-state regimes of system will be chaotic attractors are ploted by black color. Areas of existence of deterministic chaos (black areas) occupy the considerable space in a map of dynamic regimes. It testifies that the deterministic chaos is a typical steady-state regime of system (1).

Studying of types of the steady-state regimes of system (1) and features of realization of possible scenarios of transitions between dynamic regimes of different types we will investigate at changing of parameter N_3 along vertical section of a map (fig. 2) at $\alpha = -0.3$.

Let's consider the scenario of transition to chaos, which is realized in system at values of parameter N_3 which go out through the right boundary of a window of periodicity $-0.65269 < N_3 < -0.6296$. At each value of parameter in interval $-0.65269 < N_3 < -0.6369$ in system simultaneously exist two stable single-turn limit cycles. Their projections of phase portraits, built at $N_3 = -0.64$, are presented in fig. 3a–b. These projections are symmetrical in regard to an abscissa axis $p_2 = 0$. At parameter increasing, at value $N_3 = -0.6368$, happen a period-doubling bifurcation. In system simultaneously exist two two-turn limit cycles of the doubled period. Projections of phase portraits of cycles of doubled period at $N_3 = -0.6368$ are shown in fig. 3c–d. Projections of these cycles also are symmetrical in regard to an abscissa axis. The further increasing of value of parameter N_3 leads to arising of the symmetrical cycles of quadruple period etc. Such infinite process of periods-doubling of simultaneously existing symmetrical cycles comes to an end with arising of a chaotic attractor at $N_3 = -0.6295$ (fig. 3e–f).

The projection of the arising chaotic attractor (fig. 3e) consists of two symmetrical parts in regard to horizontal axis. Amplitudes of temporal realizations of the given chaotic attractor more than twice exceed amplitudes of temporal realizations of limit cycles of the cascade of bifurcations of period-doubling. Accordingly the chaotic attractor is localized in considerably more volume of phase space than volume of localization of any cycles of cascade of period-doubling. Moving of a typical trajectory on a chaotic attractor can be conventionally divided into two phases. In first of these phases the trajectory makes chaotic walks along coils of upper or lower parts of chaotic attractor. In an unpredictable moment of time the trajectory "jumps" from the upper or lower part of an attractor in its symmetrical part and again starts to make chaotic walks. Such process is repeated the infinite number of times. Thus transition to chaos has peculiarities which typical as for the Feigenbaum's scenario (infinite cascade of bifurcations of period-doubling of limit cycles), and as for an intermittency (an unpredictable intermittency between the upper and lower parts of arising chaotic attractor).

In fig. 4 are shown the distribution of spectrum density (Fourier–spectrums) of the constructed regular and chaotic attractors. Fourier–spectrums of single-turn limit cycles and their first bifurcation of a period-doubling (fig. 4a–b) are discrete and harmonic. It is easy to observe occurrence of a new harmonics in Fourier–spectrum in fig. 4b, that typical for the Feigenbaum's scenario. Distribution of a spectral density of a chaotic attractor at $N_3 = -0.6295$ is

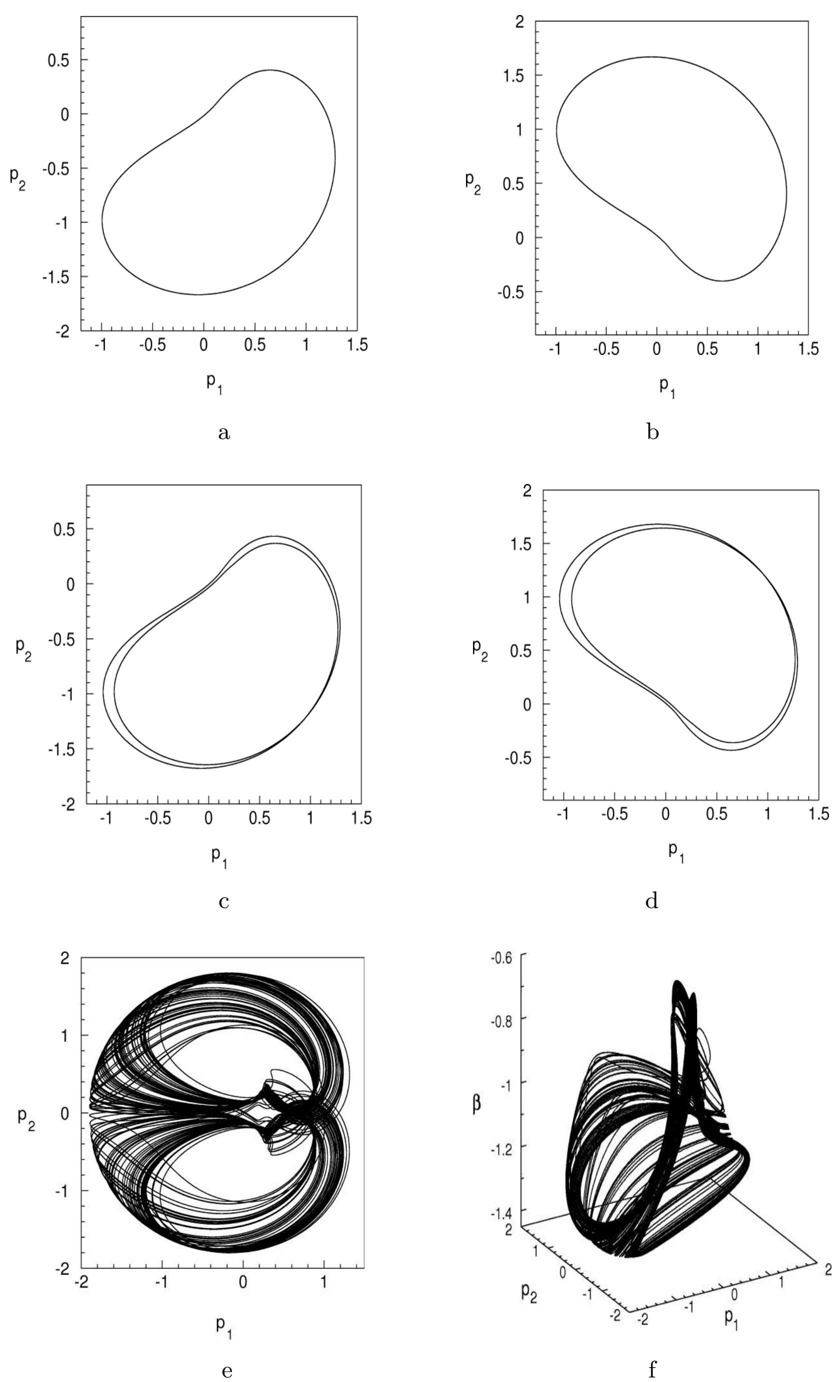

Fig. 3. Projections of phase portraits of limit cycles at $N_3 = -0.64$ (a–b), $N_3 = -0.6368$ (c–d) and chaotic attractor at $N_3 = -0.6295$ (e–f)

continuous. In its Fourier–spectrum practically completely disappear separate spectral peaks.

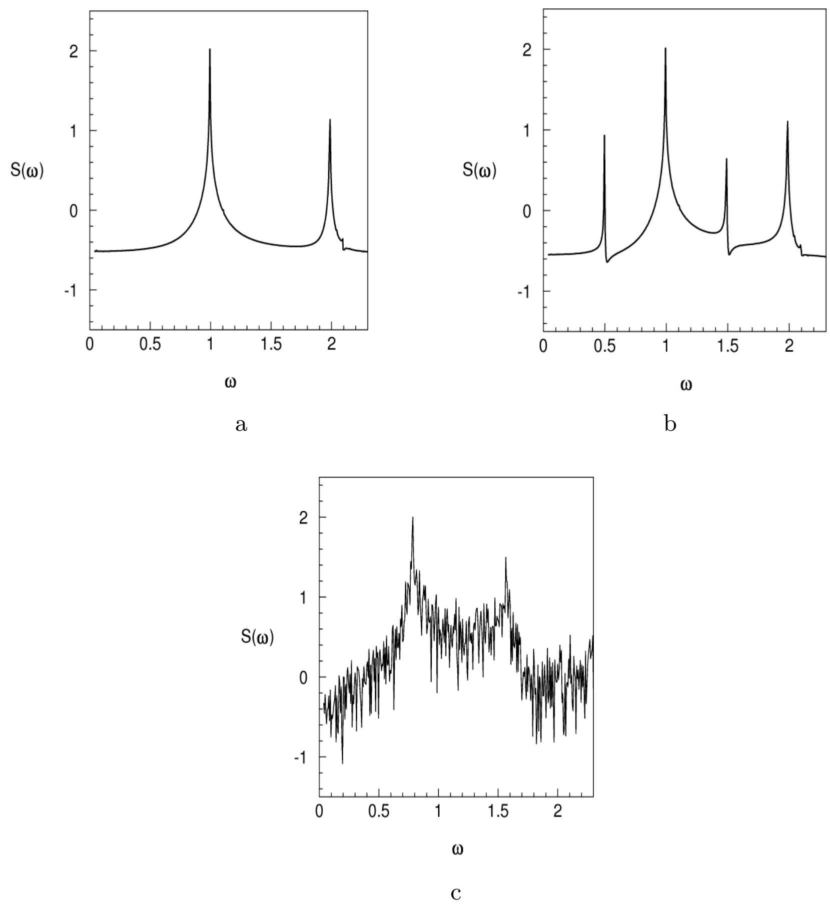

Fig. 4. Fourier–spectrum of limit cycles at $N_3 = -0.64$ (a), $N_3 = -0.6368$ (b) and chaotic attractor at $N_3 = -0.6295$ (c)

Further consider the transition to deterministic chaos through the left boundary of a window of periodicity

$$-0.65269 < N_3 < -0.6296. \tag{2}$$

As it has been told earlier, at each value of parameter in interval $-0.65269 < N_3 < -0.6369$ in system simultaneously exist two symmetrical, in regard to an abscissa axis, and stable single-turn limit cycles (fig. 3a–b). At reaching in parameter N_3 the left boundary of a window of periodicity (2), the both limit cycles are disappearing and in system arise a chaotic attractor. The projection of a phase portrait of a chaotic attractor of this kind is presented in fig. 5a. The constructed projection of this chaotic attractor is symmetrical in regard to axis $p_2 = 0$ and outwardly is similar with a projection of a chaotic attractor shown in fig. 3e.

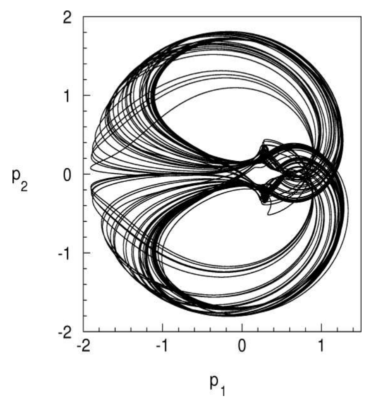

a

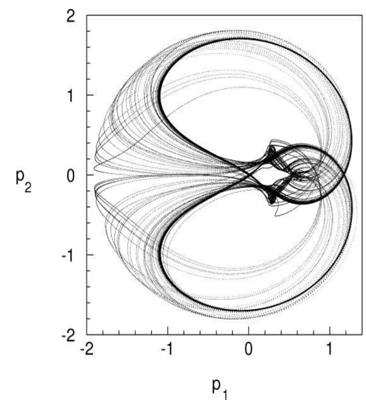

b

Fig. 5. Projections of phase portrait (a) and distribution of invariant measure (b) of chaotic attractor at $N_3 = -0.6527$

In fig. 5b distribution of an invariant measure in a phase portrait of a chaotic attractor is shown at $N_3 = -0.6527$. The constructed distribution makes clear the mechanism of arising of the given chaotic attractor. Contours of accurately traced area in fig. 5b under the shape represent two "pasted together" the symmetrical limit cycles presented in fig. 3a–b. Scenario of arising of chaos has many typical characteristics of an intermittency of Pomeau-Manneville. However, in this case the moving of trajectory in an attractor consists of three phases, two laminar phase and one turbulent.

In the first laminar phase the trajectory fulfils quasi-periodic motions in a small neighbourhood of one of "pasted together" disappeared cycles, either of "upper" or of "lower". In an unpredictable moment of time happens a turbulent cruption outburst and a trajectory leaves away from a neighbourhood of the disappeared cycle into distant phase space areas. To such turbulent phase of motion answer a more pale areas in distribution of an invariant measure in fig. 5b. After end of a turbulent phase, the trajectory can return into the first laminar phase of motion, or transfer in the second laminar phase, to which correspond quasi-periodic motions in a small neighbourhood of second of the disappeared limit cycles. Such process of motion of a trajectory in attractor of type "one of the laminar phases–a turbulent phase–one of the laminar phases" is iterate infinitely often. The moments of transition of trajectories into a turbulent phase, as and the moments of "switching" of trajectories between two laminar phases are unpredictable. Thus transition to chaos reminds the classical scenario of Pomeau-Manneville. However, unlike the classical scenario, we have not one, but two laminar phases.

4 Conclusions

Thus computer simulation and a numerical analysis of some aspects of the regular and chaotic dynamics of nonideal dynamic system "a tank with a fluid-electromotor" is carried out. The map of dynamic regimes of system is constructed. Atypical peculiarities of realization of scenarios of transition to deterministic chaos are revealed and described. The possibility of realization of the scenario of transition to deterministic chaos, which unites the Feigenbaum's scenario and an intermittency is detected. Also transition to chaos through an intermittency which consists not of one, but of two laminar phases is described.

References

1.R.A. Ibrahim. Liquid Sloshing Dynamics: Theory and Applications. Cambridge University Press, Cambridge, 2005.
2.I.A. Lukovsky. Fluid non-linear oscillations in vessels of the complex geometrical form. Kyiv, Naukova Dumka, 1975 (in russian).
3.J.W. Miles. Nonlinear surface waves in closed basins. J. Fluid Mech., vol.75, no. 3, 419–448, 1976.
4.J.W. Miles. Internally resonant surface waves in circular cylinder. J. Fluid Mech., vol.149, 1–14, 1984.
5.J.W. Miles. Resonantly forced surface waves in circular cylinder. J. Fluid Mech., vol.149, 15–31, 1984.
6.V.O. Kononenko. Vibrating system with a limited power–supply. London, Iliffe, 1969.
7.T.S. Krasnopolskaya , Yu. Shvets. Chaotic surface waves in limited power–supply cylindrical tank vibrations. J. Fluids & Structures, vol. 8, no. 1, 1-18, 1994.
8.T.S. Krasnopolskaya, Yu. Shvets. Regular and chaotic dynamics of systems with limited excitation. Moskow-Izhevsk, RCD, 2008 (in russian).
9.T.S. Krasnopolskaya , Yu. Shvets. Dynamical chaos for a limited power supply oscillations in cylindrical tanks. Journal of Sound and Vibration, vol.322, 532-553, 2009.
10.T.S. Krasnopolskaya , Yu. Shvets. Regular and chaotic surface waves in a liquid in a cylindrical tank. Sov. Appl. Mech., vol. 26, 787–794, 1990.
11.S.P. Kuznetsov. Dynamical chaos. Physmatlit, Moskow, 2006 (in russian).

Chaotic Modeling and Simulation (CMSIM) 2: 311-322, 2012

Fractal Geometry and Architecture Design: Case Study Review

Xiaoshu Lu[1,2], Derek Clements-Croome[3], Martti Viljanen[1]

[1]Department of Civil and Structural Engineering, School of Engineering, Aalto University, PO Box 12100, FIN-02150, Espoo, Finland
E-mail: xiaoshu@cc.hut.fi
[2]Finnish Institute of Occupational Health, Finland
[3]School of Construction Management and Engineering, Whiteknights, University of Reading, PO Box 219, Reading RG6 6AW, UK

Abstract: The idea of buildings in harmony with nature can be traced back to ancient times. The increasing concerns on sustainability oriented on buildings have added new challenges in building architecture design and called for new design responses. Sustainable design integrates and balances the human geometries and the natural ones. As the language of nature, it is, therefore, natural to assume that fractal geometry could play a role in developing new forms of aesthetics and sustainable architecture design. This paper gives a brief description of fractal geometry theory and presents its current status and recent developments through illustrative review of some fractal case studies in architecture design, which provides a bridge between fractal geometry and architecture design.
Keywords: Fractal geometry, Architecture design, Sustainability.

1. Introduction

The idea of buildings in harmony with nature can be traced back to ancient Egyptians, China, Greeks and Romans. At the beginning of 21st century, the increasing concerns on sustainability oriented on buildings have added new challenges in building architecture design and called for new design responses. As the language of nature [1,2], it is, therefore, natural to assume that fractal geometry could play a role in developing new forms of design of sustainable architecture and buildings.

Fractals are self-similar sets whose patterns are composed of smaller-scales copied of themselves, possessing self-similarity across scales. This means that they repeat the patterns to an infinitely small scale. A pattern with a higher fractal dimension is more complicated or irregular than the one with a lower dimension, and fills more space. In many practical applications, temporal and

Received: 29 June 2011 / Accepted 30 March 2012

ISSN 2241-0503

spatial analysis is needed to characterise and quantify the hidden order in complex patterns, fractal geometry is an appropriate tool for investigating such complexity over many scales for natural phenomena [2,3]. Order in irregular pattern is important in aesthetics as it embraces the concept of dynamic force, which shows a natural phenomenon rather than mechanical process. In architecture design terms, it represents design principle. Therefore, fractal geometry has played a significant role in architecture design.

In spite of its growing applications, such works in literature are rather narrow, i.e. they mainly focus on applications for fractal design patterns on aesthetic considerations. Few works have related to comprehensive and unified view of fractal geometry in structural design, for example, as it is intended in this study. We aim to fill in this gap by introducing fractals as new concepts and presenting its current status and recent developments in architecture through illustrative review of some fractal case studies in design. The paper shows that incorporating the fractal way of thinking into the architecture design provides a language for an in-depth understanding of complex nature of architecture design in general. This study distils the fundamental properties and the most relevant characteristics of fractal geometry essential to architects and building scientists, initiates a dialogue and builds bridges between scientists and architects.

2. Basic Theory of Fractal Geometry

2.1. Basic Theory

The mathematical history of fractals began with mathematician Karl Weierstrass in 1872 who introduced a Weierstrass function which is continuous everywhere but differentiable nowhere [4]. In 1904 Helge von Koch refined the definition of the Weierstrass function and gave a more geometric definition of a similar function, which is now called the Koch snowflake [5], see Figure 1. In 1915, Waclaw Sielpinski constructed self-similar patterns and the functions that generate them. Georg Cantor also gave an example of a self-similar fractal [6]. In the late 19th and early 20th, fractals were put further by Henri Poincare, Felix Klein, Pierre Fatou and Gaston Julia. In 1975, Mandelbrot brought these work together and named it 'fractal'.

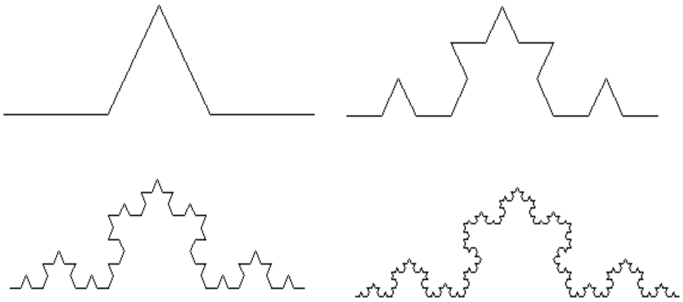

Fig. 1. Illustration of Koch Curve.

Fractals can be constructed through limits of iterative schemes involving generators of iterative functions on metric spaces [2]. Iterated Function System (IFS) is the most common, general and powerful mathematical tool that can be used to generate fractals. Moreover, IFS provides a connection between fractals and natural images [7,8]. It is also an important tool for investigating fractal sets. In the following, an introduction to some basic geometry of fractal sets will be approached from an IFS perspective. In a simple case, IFS acts on a segment to generate contracted copies of the segment which can be arranged in a plane based on certain rules. The iteration procedure must converge to get the fractal set. Therefore, the iterated functions are limited to strict contractions with the Banach fixed-point property.

Let (X, d) denotes a complete metric space and $H(X)$ the compact subsets of X, the Hausdorff distance is defined as

$$h(A,B) = \max\{d(A,B),\, d(B,A)\} \quad \forall\, A, B \in H(X) \tag{1}$$

It is easy to prove that h is a metric on $H(X)$. Moreover, it can be proved that $(H(X), h)$ is also a complete metric space [7] which is called the space of fractals for X.

A contraction mapping, or contraction w: $X \mapsto X$ has the property that there is some nonnegative real number $k \in [0,1)$, contraction factor k, such that

$$d(w(x),\, w(y)) \le k\, d(x,y) \tag{2}$$

In non-technical terms, a contraction mapping brings every two points closer in the metric space it maps. The Banach fixed point theorem guarantees the existence and uniqueness of fixed points of contract maps on metric spaces: If w: $X \mapsto X$ is a contraction, then there exists one and only one $x \in X$ such that $w(x) = x$.

The Banach fixed point theorem has very important applications in many branches of mathematics. Therefore, generalisation of the above theorem has been extensively investigated, for example, in probabilistic metric spaces. The theorem also provides a constructive method to find fixed-point.

An IFS [9] is a set of contraction mappings w_i defined on (X, d) with contraction factors k_i for $i = 1,2,\ldots, N$. We denote it as $\{X; w_i, i = 1,2,\ldots, N\}$ and contraction factor $k = \max\{k_i, i = 1, 2,\ldots, N\}$. Hutchinson [9] proved an important theorem on a set of contraction mappings in which IFS is based: Let $\{X; w_i, i = 1,2,\ldots, N\}$ be an IFS with contraction factor k. Then W: $H(X) \mapsto H(X)$ defined as

$$W(B) = \bigcup_{i=1}^{N} w_i(B) \quad \forall\ B \in H(X) \tag{3}$$

is a contraction mapping on $(H(X), h)$. From Banach's theorem, there exists a unique set $A \in H(X)$, the attractor of IFS, such that

$$A = W(A) = \bigcup_{i=1}^{N} w_i(A) \tag{4}$$

It can be seen that A is self-similar since it is expressed as a union of transformations (copies) of itself. The attractor A can be taken as a definition of deterministic fractals.

2.2. Fractal dimensions

Mandelbrot [2] proposed a simple but radical way to qualify fractal geometry through fractal dimension based on a discussion of the length of the coast of England. The dimension is a statistical quantity that gives an indication of how completely a fractal appears to fill space, as one zooms down to finer scales. This definition is a simplification of Hausdorff dimension that Mandelbrot used to based. We focus on this one and briefly mentions box-counting dimension because of its widely practical applications. However, it should be noted that there are many specific definitions of fractal dimensions, such as Hausdorff dimension, Rényi dimensions, box-counting dimension and correlation dimension, etc, none of them should be treated as the universal one.

For $A \in H(X)$, let $n(A,\varepsilon)$, ε<0, denote the smallest number of closed balls of radius ε needed to cover A. If

$$D = \lim_{\varepsilon \to 0} \frac{\log n(A,\varepsilon)}{\log \frac{1}{\varepsilon}} \tag{5}$$

exists, then D is called the fractal dimension of A.

So $n(A,\varepsilon)$ is proportional to ε^{-D} as $\varepsilon \to 0$ or the exponent D is in $n(A,\varepsilon) = \varepsilon^{-D}$ which is the power law relationship. A power law describes a dynamic relationship between two objects which portrays a wide variety of natural and man-made phenomena. A key feature of the power law is that the power law relationship is independent of scales. A good example of intuition of fractal dimension is a line with the length of ε, where ε is the measuring length. Assume the line is divided in 3 equal parts and $\varepsilon = \frac{1}{3}$ then the simplified $n(A,\varepsilon) = \varepsilon^{-D}$ gives $3 = (1/3)^{-D}$ with $D = 1$. Similarly, the Koch curve's fractal dimension is $D = \frac{\log 4}{\log 3} = 1.26$.

Practically, the fractal dimension can only be used in the case where irregularities to be measured are in the continuous form. Natural objects offer a lot of variation which may not be self-similar. The Box-counting dimension is much more robust measure which is widely used even to measure images. To calculate the box-counting dimension, we need to place the image on a grid. The number of boxes, with size s_1, that cover the image is counted (n_1). Then the number of a smaller grid of boxes, with size s_2, is counted (n_2). The fractal dimension between two scales is then calculated by the relationship between the difference of the number of boxed occupied and the difference of inverse grid sizes [10]. In more chaotic and complex objects such as architecture and design, more flexible and robust measures, such as range analysis, midpoint displacement, etc, can be employed. For more detailed information, readers may refer to Bovill's book [10].

2.3. Examples of IFS applications

Fractal geometry is at the conceptual core of understanding nature's complexity and IFS provides an important concept for understanding the core design of the natural objects as well as approximating the natural design. In this subsection we outline the evolution of the idea of IFS with our calculation examples.

We know that the Banach's fixed-point theorem forms the basis of the IFS applications. However, applying the theorem in practiced raises two central questions. One is to find the attractor for a given IFS. The other is to find IFS for a given attractor, an inverse problem of the first.

For the first problem, the attractor can be obtained by successive approximations from any starting point theoretically. From a computational point of view, two techniques, deterministic and stochastic, can be applied. The deterministic algorithm starts with an arbitrary initial set to reach the attractor. The stochastic algorithm is often more complex but more efficient. A stochastic algorithm associates to the IFS system a set of probabilities by assigning a probability to each mapping, which is used to generate a random walk. If we start with any point and apply transformations iteratively, chosen according the probabilities attached, we will come arbitrarily close to the attractor. The associated probabilities determine the density of spatially contracted copies of the attractor. Therefore, the probabilities have no effect on the attractor but influence significantly the rendering of its approximations.

The second problem, the inverse problem, can be solved by Barnsley's Collage Theorem, a simple consequence of Banach's fixed point theorem. Such procedure was illustrated nicely through the 'Barnsley fern' in [9] and [11] using four-transformation IFS with associated probabilities. Figure 2 shows our calculation examples of fractals using four-transformation IFS with variations and their associated probabilities produced by Matlab, where 20000 iterations were set. These fractals actually have more than one attractor. In Figure 2, the four-transformation matrices are

$$A=\begin{bmatrix}0&0&0\\0&0.18&0\\0&0&1\end{bmatrix}\ B=\begin{bmatrix}0.19&-0.25&0\\0.22&0.23&1.7\\0&0&1\end{bmatrix}\ C=\begin{bmatrix}-0.15&0.28&0\\0.24&0.25&0.44\\0&0&1\end{bmatrix}\ D=\begin{bmatrix}0.76&0.04&0\\-0.05&0.95&1.7\\0&0&1\end{bmatrix} \quad (6)$$

D has the probability 0.75 and others 0.083.

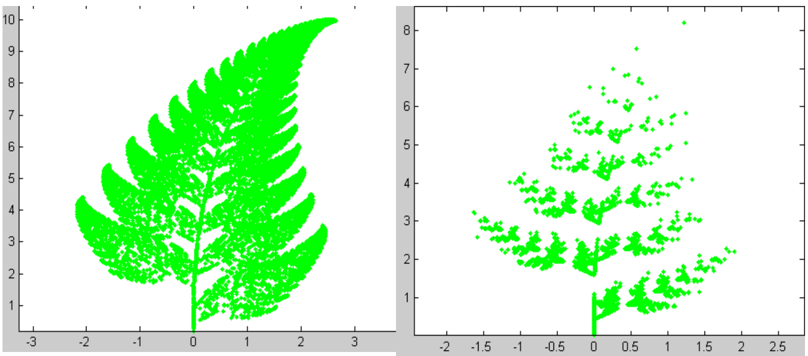

Fig. 2. Calculation examples of fractals using IFS with variations.

3. Applications of Fractal Geometry to Architecture Design

3.1. Applications of IFS

IFS provides wide range of architecture design applications in patterns and structures. Very often, IFS codes are used to generate fractals. For example, topology (layout) optimization has been proposed and is based on IFS representations with various applications [12]. Chang [13] proposed a hierarchical fixed point-searching algorithm for determining the original coordinates of a 2-D fractal set directly from its IFS code. The IFS code cane be modified according to the desired transformation. Figure 3 shows the Castle with different reflection directions generated by the modified IFS codes.

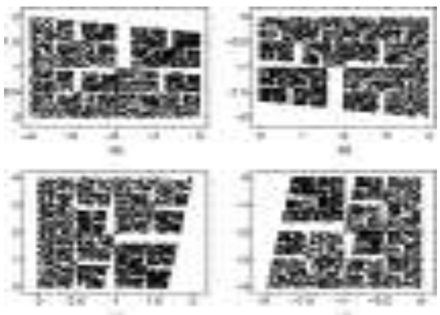

Fig. 3. Castle example generated by the modified IFS codes [13].

3.2. Applications of fractal geometry

Fractal geometry has been applied in architecture design widely to investigate fractal structures of cities [14] and successfully in building geometry [15,16] and design patterns [10].

Early fractal building patterns can be traced to ancient Maya settlement. Brown et al. analysed fractal structures of Maya settlement and found that fractals exhibit both within communities and across regions in various ways: at the intra-site, the regional levels and within archaeological sites. Moreover, spatial organisation in geometric patterns and order are also fractals, which presents in the size-frequency distribution, the rank-size relation among sites and the geographical clustering of sites [17]

In Europe, fractals were found in the early 12th century buildings. The floor of the cathedral of Anagni in Italy built in 1104 is adorned with dozens of mosaics in a form of a Sierpinski gasket fractal (See Figure 4).

Fig. 4. The floor of the cathedral of Anagni in Italy [18].

Fractals have been applied to many elevation structures to exclusively address power and balance. Some very excellent examples of classical architecture can be seen in many parts of the Europe, in the Middle East and Asia which have effects of fractal elevations, for example, Reims' cathedral and Saint Paul church in France, Castel del Monte in Italy and many palaces in Venice (ca' Foscari, Ca' d'Oro, Duke Palace, Giustinian Palace) in Italy. Venice has been one of the most talked about fractal Venice [18] (see Figure 5). More vital evidence shows that fractals exist in Gothic cathedral in general. The pointed arch, an impression of elevation, appear in entrance, at windows and the costal arch with many scales and details [19]. Figure 6 displays the elevations of a five-floor tenement building in the historical part of Barcelona which shows self-organisation structure.

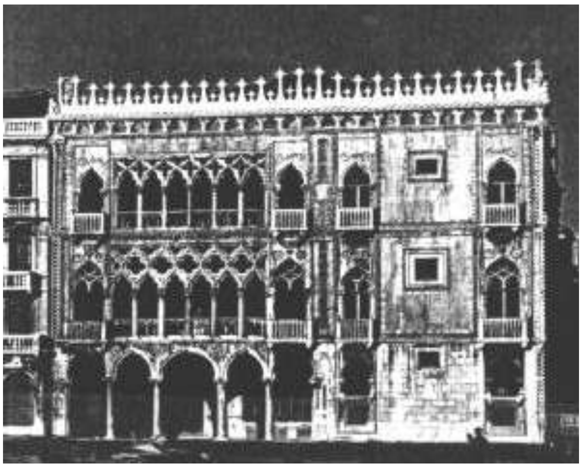

Fig. 5. Fractal building in Venice [18].

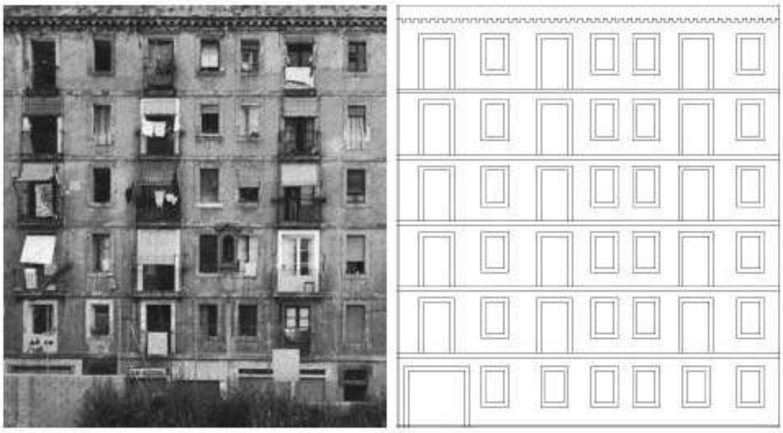

Fig. 6. A tenement house in the historical part of Barcelona, Spain: the elevation's photograph from the 90-s (left part); the geometric synthesis shows the original architecture design (middle part) [20].

In the Middle East, fractal patterns have been adopted widely in designing stucco, a typically Persian art form for the decoration of dome interiors. In Figure 7, the pattern in the dome interior has four attractors surrounding the main one at the center (Sarhangi).

Fig. 7. Stucco dome interior in a private house in Kashan [21].

In Asia, architectures with fractal structures have also been found in Humayun's Mausoleum, Shiva Shrine in India and the Sacred Stupa Pha That Luang in Laos. Fractals have been used to study Hindu temples. In China, some mosques in the west were more likely to incorporate such domes which are fractals. One important feature in Chinese architecture is its emphasis on symmetry which connotes a sense of grandeur [22].

Besides geographical localities, in recent times, the concept of fractals has been extended in many well known architectures including Frank Lloyd Wright's 'Robie House', 'Fallingwater', 'Palmer house' and 'Marion County Civic', which demonstrate that fractals have universal appeal and are visually satisfying because they are able to provide a sense of scale at different levels. Wright is one of the most representatives of organic architects. His designs grew out of the environment with regards to purpose, material and construction [10]. Fractals have inspired many great modern designers such as Zaha Hadid, Daniel Liebeskind, Frank Gehry and others with many notable fractal architectures [20]. Indeed, according to Ibrahim et al, architects and designers started to adopt fractals as a design form and tool in 1980th [10]. Yessios et al. was among the first utilising fractals and fractal geometry design in architecture [23]. They developed a computer program to aid architecture using fractal generators. In 1990th, Durmisevic and Ciftcioglu applied fractal tree as an indicator of a road infrastructure in the architecture design and urban planning [24].

Wen et al. established the fractal dimension relations matrix table analysis to classify architecture design style patterns for the masterpieces of three modern architecture masters: Frank Lioyd Wright, Le Corbusier and Mies van der Rohe [25]. Figure 8 shows the results. It can be seen that the temporal trends of individuals vary. The fractal dimensions of Frank Lioyd Wright are average with low beginning in the early 1900th and end in the mid 1930th. The trend of Le Corbusier goes downside with gentle slope from mid 1900th to mid 1950th. For the period shown in the grape, the trend of Mies van der Rohe has the same trend as that of Frank Lloyd Wright from the early 1900th to the mid 1930th. The average trend of these three masters goes down in general starting from 1930th.

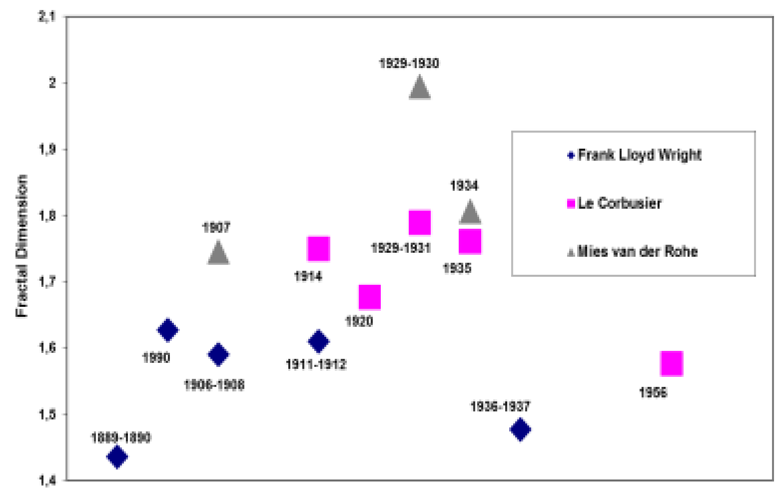

Fig. 8. Fractal dimensions for the masterpieces of three modern architects.

4. Conclusions

This paper has illustratively reviewed the fundamental concepts and properties of fractal geometry theory essential to architecture design, as well as the current state of its applications. Fractal geometry has important implications for buildings. The representative review shows that architecture design is not made to be isolated but to anticipate changes in the environment. Accumulation of technological modernisations, destroying, adapting and many changes have caused the design temporal and spatial diversity and complex. More specifically, sustainable development in a building can be looked upon as adaptability and flexibility over time when it comes to responding to changing environment. Chaos and many other nonlinear theories have explained that extremely deterministic and linear processes are very fragile in maintaining stability over a wide range of conditions, whereas chaotic and fractal systems can function effectively over a wide range of different conditions, thereby offering adaptability and flexibility. In this context, fractal geometry theory offers prescriptive for architecture design. This paper provides a bridge between building engineering and architecture and fractal geometry theory.

References

1. B. Mandelbrot. *Fractals, Form, Chance and dimension*, Freeman, San Francisco, 1977.
2. B.Mandelbrot. *The Fractal Geometry of Nature*. W.H. Freeman and Company, 1982.
3. P.A. Burrough. Fractal dimensions of landscapes and other environmental data. *Nature* 294: 240–242, 1981.
4. K. Weierstrass, On continuous functions of a real argument that do not have a well-defined differential quotient, in G. Edgar, ed *Classics on Fractals*, Addison-Wesley, Reading, Massachusetts, 3-9, 1993.
5. H. von Koch. On a continuous curve without tangents constructible from elementary geometry, in G. Edgar, ed *Classics on Fractals*, Addison-Wesley, Reading, Massachusetts, 25-45, 1993.
6. G. Cantor. On the Power of Perfect Sets of Points. in G. Edgar, ed *Classics on Fractals*, Addison-Wesley, Reading, Massachusetts, 11-23, 1993.
7. M. Barnsley. *Fractals Everywhere*. Academic Press, 1988.
8. H.O. Peitgen.1988. Fantastic Deterministic Fractals, in: H.O. Peitgen, D. Saupe. *The Science of Fractal Images*, 202, Springer, New York, 1988.
9. J.E. Hutchinson. Fractals and self similarity. *Indiana Univ. Math. J.* 30: 713–747, 1981.
10. C. Bovill. *Fractal Geometry in Architecture and Design*, Birkhauser, Boston, 1996.
11. M. Ebrahimi, E.R. Vrscay. Self-similarity in imaging, 20 years after "Fractals Everywhere", http://ticsp.cs.tut.fi/images/3/3f/Cr1023-lausanne.pdf.
12. H.T. Chang. Arbitrary affine transformation and their composition effects for two-dimensional fractal sets. *Image and Vision Computing* 22: 1117-1127, 2004.
13. H. Hamda, F. Jouve, E. Lutton, M. Schoenauer, M. Sebag, Compact unstructured representations for evolutionary topological optimum design. *Appl Intell* 16: 139-155, 2002.
14. M. Batty, P. Longley. *Fractal Cities*, London: Academic Press, 1994.
15. K. Trivedi. Hindu temples: models of a fractal universe. *The Visual Computer* 5: 243-258, 1989.
16. N. Sala. The presence of the Self-similarity in Architecture: some examples. Emergent Nature - Patterns, Growth and Scaling in the Sciences, World Scientific 273-282, 2002.
17. C.T. Brown, W.R.T. Witschey. The fractal geometry of ancient Maya settlement. *Journal of Archaeological Science* 30: 1619-1632, 2003.
18. N. Sala. Fractal models in architecture: a case of study. http://math.unipa.it/~grim/Jsalaworkshop.PDF.
19. W.E. Lorenz. *Fractals and Fractal Architecture*, Mater Thesis, Vienna, 2003.
20. P. Rubinowicz. Chaos and geometric order in architecture and design. *Journal for Geometry and Graphics* 4: 197-207, 2000.
21. http://en.wikipedia.org/wiki/Islamic_architecture.
22. J.S. Cowen. Muslims in China: The mosque. *Saudi Aramco World. Retrieved 2006-04-08*, 30-35, 1985.
23. C.I. Yessios. A fractal studio. *ACADIA '87 Workshop Proceedings*, 1987.
24. S. Durmisevic, O. Ciftcioglu. Fractals in architectural design. *Mathematics and Design*. Javier Barrallo the university of the Basque Country, 1988.
25. K-C. Wen, Y-N. Kao. An analytic study of architectural design style by fractal dimension method, *22nd International Symposium on Automation and Robotics in Construction ISARC 2005*, Italy, 2005, http://www.iaarc.org/publications/fulltext/isarc2005-63wen.pdf

Chaotic Modeling and Simulation (CMSIM) 2: 323-335, 2012

A Sub Microscopic Description of the Formation of Crop Circles

Volodymyr Krasnoholovets[1] and Ivan Gandzha[2]

Indra Scientific, Square de Solbosch 26, Brussels, B-1050, Brussels, Belgium
(E-mail: [1] v_kras@yahoo.com, [2] gandzha@iop.kiev.ua)

Abstract: We describe a sub microscopic mechanism that is responsible for the appearance of crop circles on the surface of the Earth. It is shown that the inner reason for the mechanism is associated with intra-terrestrial processes occurring in the outer core and the mantle of the terrestrial globe. We assume that magnetostriction phenomena should take place at the boundary between the liquid and the solid nickel-iron layers of the terrestrial globe. Our previous studies showed that at the magnetostriction a flow of inertons takes out of the striction material (inertons are carriers of the field of inertia, they represent a substructure of the matter waves, or the particle's psi-wave function; they transfer mass properties of elementary particles and are able to influence massive objects changing their inner state and behaviour). At the macroscopic striction in the interior of the Earth, pulses of inerton fields are irradiated, and through non-homogeneous channels of the globe's mantle and crust they reach the surface of the Earth. Due to the interaction with walls of these channels, fronts of inerton flows come to the surface as fringe images. These inerton flows affect local plants and bend them, which results in the formation of the so-called crop circles. It is argued that the appearance of crop circles under the radiation of inertons has something in common with the mechanism of formation of images in a kaleidoscope, which happens under the illumination of photons.

Keywords: Crop circles, Inertons, Mantle and Crustle channels, Magnetostriction of rocks.

1 Introduction

Crop circles attract attention of many researchers. Studies (see, e.g. Refs. 1-3) show that in these circles stalks are bent up to ninety degrees without being broken and something softened the plant tissue at the moment of flattening. Something stretches stalks from the inside; sometimes this effect is so powerful that the node looks as exploded from the inside out. In many places crop formation is accompanied with a high degree of magnetic susceptibility, which is caused by adherent coatings of stalks with the commingled iron oxides, hematite (Fe_20_3) and magnetite (Fe_30_4) fused into a heterogeneous mass [2].

Researchers [2-4] hypothesized that crop formations involve organised ion plasma vortices, which deliver lower atmosphere energy components of

Received: 18 July 2011 / Accepted 30 March 2012
 ISSN 2241-0503

sufficient magnitude to produce bending of stalks, the formation of expulsion cavities in plant stems and significant changes in seedling development.

It should be noted that an idea of the origin of crop circles associated with the atmosphere energy and/or UFO is generally accepted.

On the other hand, researchers who study geophysical processes and the earthquakes note about possible regional semi-global magnetic fields that might be generated by vortex-like cells of thermal-magmatic energy, rising and falling in the earth's mantle [5]. Another important factor is magnetostriction of the crust – the alteration of the direction of magnetization of rocks by directed stress [6,7].

Moreover, recent study [8] has suggested a possible mechanism of earthquake triggering due to magnetostriction of rocks in the crust. The phenomenon of magnetostriction in geophysics is stipulated by mechanical deformations of magnetic minerals accompanied by changes of their remanent or induced magnetization. These deformations are specified by magnetostriction constants, which are proportional coefficients between magnetization changes and mechanical deformations. A real value of the magnetostriction constant of the crust is estimated as about 10^{-5} ppm/nT, which is a little larger than for pure iron. Yamazaki's calculation [8] shows that effects connected to the magnetostriction of rocks in the crust can produce forces nearly 100 Pa/year and even these comparatively small stress changes can trigger earthquakes.

Of course, weaker deformations associated with magnetostriction of rocks also take place. These are the magnetostriction deformations that we put in the foundation of the present study of field circles.

2 Preliminaries

Our theoretical and experimental studies have shown that the phenomenon of magnetostriction is accompanied with the emission of inerton fields from the magnetostrictive material studied. What is the inerton field?

Bounias and one of the authors [9-12] proposed a detailed mathematical theory of the constitution of the real physical space. In line with this theory, real space is constrained to be a mathematical lattice of closely packed topological balls with approximately the Planck size, $\sqrt{\hbar G/c^3} \approx 10^{-35}$ m. It was proven that such a lattice is a fractal lattice and that it also manifests tessellation properties. It has been called a tessel-lattice. In the tessel-lattice volumetric fractalities of cells are associated with the physical concept of mass. A particle represents a volumetrically deformed cell of the tessel-lattice. The motion of such a particle generates elementary excitations of the tessel-lattice around the particle. These excitations, which move as a cloud around the particle, represent the particle's force of inertia. That is why they were called inertons [13,14]. The corresponding submicroscopic mechanics developed in the real space can easily be connected to conventional orthodox quantum mechanics constructed in an abstract phase space. Submicroscopic mechanics associates the particle's cloud of inertons with the quantum mechanical wave ψ-function of this particle. Thus, the developing concept turns back a physical sense to the wave ψ-function: this function represents the field of inertia of the particle under consideration. Carriers of the field of inertia are inertons. A free inerton, which is released from the particle's cloud of inertons, possesses a velocity that exceeds the velocity of light [15].

In condensed media entities vibrating at the equilibrium positions periodically irradiate and absorb their clouds of inertons back [16]; owing to such a behaviour the mass of entities varies. This means that under special conditions the matter may irradiate a portion of its inertons. Lost inertons then can be absorbed by the other system, which has to result in changes of physical properties of the system.

One of such experiments was carried out in work [17]. Continuous-wave laser illumination of ferroelectric crystal of $LiNbO_3$ resulted in the production of a long-living stable electron droplet with a size of about 100 μm, which freely moved with a velocity of about 0.5 cm/s in the air near the surface of the crystal experiencing the Earth's gravitational field. The role of the restraining force of electrons in the droplet was attributed to the inerton field, a substructure of the particles' matter waves, which was expelled from the surface of crystal of $LiNbO_3$ together with photoelectrons by a laser beam. Properties of electrons after absorption of inertons changed very remarkably – they became heavy electrons whose mass at least million of times exceeded the rest mass of free electrons. Only those heavy electrons could elastically withstand their Coulomb repulsion associated with the electrical charge, which, of course, is impossible in the case of free electrons.

We have shown [16] that in the chemical industry inerton fields are able to play the role of a field catalyst or, in other words, inerton fields can serve to control the speed of chemical reactions. In the reactive chamber we generated inerton fields by using magnetostriction agents: owing to the striction the agents non-adiabatically contract, which is culminated in the irradiation of sub matter, i.e. inertons, from the agents. Then under the inerton radiation, the formation of a new chemical occurred in several seconds, though usually these chemical reactions last hours.

Therefore, these results allow us to involve inerton fields, which originate from the ground, in a study of the formation of crop circles.

The thickness of the crust is about 20 km. The mantle extends to a depth above 3000 km. The mantle is made of a thick solid rocky substance. Due to dynamical processes in the interior of the Earth, magnetostrictive rocks contract with a coefficient of about 10^{-5} [8], which is a trigger mechanism for the appearance of a flow of inerton radiation. This flow of inertons shoots up from a depth by coming through the mantle and crust channel. Such channels are usual terrestrial materials with some non-homogenous inclusions down to tens or hundreds of kilometers from the surface of the terrestrial globe (compare with bio-energy channels in our body: the crude morphological structure is the same, but the fine morphological structure is different, which allows these bio-energy channels to display a higher conductivity).

A mantle-crust channel can be modeled as a cylindrical tube, which has a cross-section area equal to A, along which a flow of inertons travels out from the interior of the globe. The inner surface of the channel has to reflect inerton radiation, at least partly, so that the flow of inertons will continue to follow along the channel to its output, i.e. the surface of the Earth.

3 Elastic rod bending model

Let us evaluate conditions under which the stalks of herbaceous plants will bend affected by mantle insertions.

A stalk of a plant can be modeled for the first approximation by an elastic rod (Fig. 1). We suppose that it is deformed by an external force distributed uniformly over the rod length. This external force is a force caused by a flow of inertons going from the ground due to a weak collision of the mantle and crust rocks as described above. The rod profile in the projections to the horizontal and vertical axes is described as follows [18].

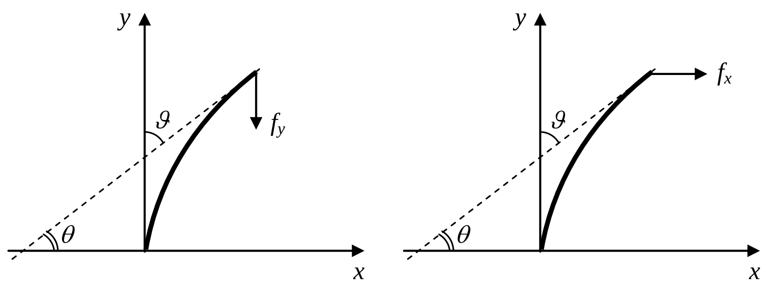

Fig. 1. Elastic rod model.

I. Vertical force f_y (Fig. 1a)

$$x = \sqrt{\frac{2IE}{f_y}}\left(\sqrt{1-\cos\vartheta_l} - \sqrt{\cos\vartheta - \cos\vartheta_l}\right), \quad y = \sqrt{\frac{IE}{2f_y}}\int_0^{\vartheta} \frac{\cos\vartheta \, d\vartheta}{\sqrt{\cos\vartheta - \cos\vartheta_l}}. \quad (1)$$

Here $I = \pi R^4/4$ is the rod's moment of inertia, R is the rod's radius, and E is the Young's modulus of the rod's material. The length of the rod is explicitly given as

$$l = \sqrt{\frac{IE}{2f_y}}\int_0^{\vartheta_l} \frac{d\vartheta}{\sqrt{\cos\vartheta - \cos\vartheta_l}}. \quad (2)$$

At the maximum bending we have $\vartheta_{\max} = \vartheta_l = \pi/2$, so that

$$l = \sqrt{\frac{IE}{2f_y}}\int_0^{\pi/2} \frac{d\vartheta}{\sqrt{\cos\vartheta}} = \sqrt{\frac{IE}{f_y}}\,K(1/2), \quad (3)$$

where $K(1/2) \approx 1.854$ is the complete elliptic integral of the first kind. Hence, we come to an expression for the force required to bend the rod by a $\pi/2$ angle:

$$f_y = \frac{IE}{l^2} K^2(1/2) \approx 3.44 \frac{IE}{l^2}. \tag{4}$$

II. Horizontal force f_x (Fig. 1b)

$$x = \sqrt{\frac{IE}{2f_x}} \int_0^{\vartheta} \frac{\sin\vartheta d\vartheta}{\sqrt{\sin\vartheta_l - \sin\vartheta}}, \qquad y = \sqrt{\frac{2IE}{f_x}} \left(\sqrt{\sin\vartheta_l} - \sqrt{\sin\vartheta_l - \sin\vartheta}\right) \tag{5}$$

The length of the rod is explicitly given as

$$l = \sqrt{\frac{IE}{2f_x}} \int_0^{\vartheta_l} \frac{d\vartheta}{\sqrt{\sin\vartheta_l - \sin\vartheta}}. \tag{6}$$

In this case the maximum bending angle should be smaller than $\pi/2$ (no such a force exists that can bend the rod by this angle). So, we select the maximum bending angle at $\vartheta_l = \pi/3$ and write the corresponding relationship between the rod's length and the acting force:

$$l \approx \sqrt{\frac{IE}{2f_x}}\, 2.61 \quad \text{or} \quad f_x \approx 3.41 \frac{IE}{l^2}, \tag{7}$$

which is nearly the same as in the previous case (4).

Now let us evaluate the value of the breaking force $f_{\text{break}} = f_x \cong f_y$. We have to substitute numerical values $l = 0.5$ m, $R = 1.5\times 10^{-3}$ m for the rod and the value of elasticity (Young's) modulus E to expressions (4) or (7). The value of E has been measured for many different grasses, see, e.g., Refs. 19-23. According to these data, E varies approximately from (0.8 to about $1)\times 10^9$ kg/(m·s^2). For instance, in the case of wheat we can take $E \approx 3\times 10^9$ kg/(m·s^2), which gives for the horizontal breaking force (7)

$$f_{\text{break}} = f_x \approx 3.41 \frac{IE_{\text{Young}}}{l^2} \approx 0.163 \text{ N}. \tag{8}$$

Besides, the authors [19-23] emphasize that for grassy stalks in addition to the elasticity modulus one has to take into account the bending stress, the yield strength (tensile strength) and the shearing stress. These parameters range from 7×10^6 to about 50×10^6 kg/(m·s^2) and, hence, significantly decrease the real value of f, which is capable to bend stalks. For example, putting for E the value of the maximal tensile stress 50×10^6 kg/(m·s^2) we obtain for the bending non-breaking force

$$f_{\text{bend}} = f_x \approx 3.41 \frac{IE_{\text{tens}}}{l^2} \approx 0.0027 \text{ N}. \tag{9}$$

The gravity force acting on the rod is

$$f_{\text{grav}} = mg = \rho V g = \pi \rho R^2 l g \approx 0.033 \text{ N}. \tag{10}$$

where ρ is the rod's material density about $\rho = 10^3$ kg/m^3, m and V are its mass and volume, and $g = 9.8$ m/s^2 is the acceleration due to gravity.

Thus we may conclude that any extraneous force F applied to a grassy stalk will be able to fold the stalk to the ground if the value of the force satisfies inequalities

$$f_{\text{bend}} \le F \le f_{\text{break}} \tag{11}$$

4 Motion of the rotating central field

The inner surface of a mantle-crust channel can be described by a retaining potential U, which is holding a flow of inertons spreading along the channel from an underground source. Let μ be the mass of an effective batch of terrestrian inertons from this source, which interact with a grassy stalk. The planar motion of such a batch of inertons in the central field is described by the Lagrangian

$$L = \frac{\mu}{2}\left(\dot{r}^2 + r^2\dot{\varphi}^2\right) - U(r, \dot{\varphi}) \tag{12}$$

which is here written in polar coordinates r and φ; dot standing for the derivative with respect to time. To model a spreading inerton field, the potential should include a dependence on the angular velocity, $U(r, \dot{\varphi})$, which means that we involve the proper rotation of the Earth relative to the flow of inertons. For instance, the potential can be chosen in the form of the sum of two potentials:

$$U(r, \dot{\varphi}) = \frac{\alpha}{2} r^2 + \frac{\beta}{2} r^2 \dot{\varphi}. \tag{13}$$

In the right hand side of expression (12) the first term is a typical central-force harmonic potential, which describes an elastic behaviour of the batch of inertons in the channel and the surrounding space; the second term includes a dependence on the azimuthal velocity, which means that it depicts the rotation-field potential. The introduction of this potential allows us to simulate more correctly the reflection of inertons from the walls of the mantle channel, which of course only conditionally can be considered round in cross-section.
The equations of motion are then written as

$$\frac{d}{dt}\frac{\partial L}{\partial \dot{q}_i} - \frac{\partial L}{\partial q_i} = 0, \quad i = 1,\ 2, \quad q_1 \equiv \rho, \quad q_2 \equiv \varphi \tag{14}$$

or in the explicit form

$$\ddot{r} - r\dot{\varphi}^2 + \frac{\alpha}{\mu} r + \frac{\beta}{\mu} r\dot{\varphi} = 0, \tag{15}$$

$$r\ddot{\varphi} + 2\dot{r} \cdot \left(\dot{\varphi} - \frac{\beta}{2\mu}\right) = 0. \tag{16}$$

These equations can be integrated explicitly or solved numerically at the given initial conditions $r(0)$, $\dot{r}(0)$, $\varphi(0)$, $\dot{\varphi}(0)$, and the trajectory of motion can be plotted in rectangular coordinates $\{r\cos\varphi,\ r\sin\varphi\}$. The second equation represents the conservation of the angular momentum M:

$$\frac{d}{dt}\left[\mu r^2 \cdot \left(\dot{\varphi} - \frac{\beta}{2\mu}\right)\right] = 0 \ \text{ or } \ M = \mu r^2 \cdot \left(\dot{\varphi} - \frac{\beta}{2\mu}\right) = \text{const}. \tag{17}$$

Figures 2 and 5 show two possible trajectories at particular values of the parameters. The radius of the inner circle is governed by the parameter β/μ.

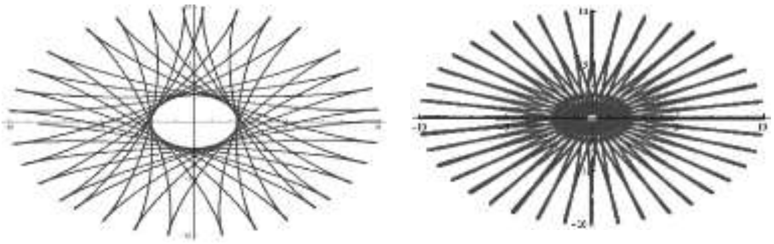

Fig. 2. Trajectories of the motion of inertons in the rotating central field. Parameters for the left figure: $\alpha/\mu = 1\ \mathrm{s}^{-2}$, $\beta/\mu = 0.5\ \mathrm{s}^{-1}$; $r(0) = 10$ m, $\dot{r}(0) = 0$, $\varphi(0) = 0$, $\dot{\varphi}(0) = 0.01\ \mathrm{s}^{-1}$.

Parameters of the right figure: $\alpha/\mu = 1\ \mathrm{s}^{-2}$, $\beta/\mu = 0.1\ \mathrm{s}^{-1}$; $r(0) = 10$ m, $\dot{r}(0) = 0$, $\varphi(0) = 0$, $\dot{\varphi}(0) = 0.01\ \mathrm{s}^{-1}$.

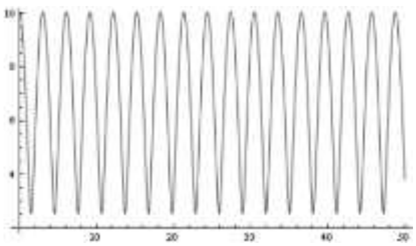

Fig. 3. Velocity $|\dot{\vec{r}}| = \sqrt{\dot{r}^2 + r^2\dot{\varphi}^2}$ of the batch of inertons versus time for the case of the trajectory shown in Fig. 2 (left). The max. velocity is $\upsilon_{\max} = 10$ m/s.

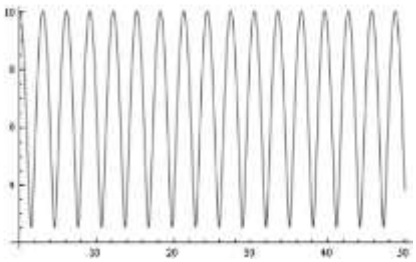

Fig, 4. Acceleration $|\ddot{\vec{r}}| = \sqrt{(\ddot{r} - r\dot{\varphi}^2)^2 + (2\dot{r}\dot{\varphi} + r\ddot{\varphi})^2}$ of the batch of inertons versus time for the case of the trajectory shown in Fig. 2 (left). The maximal acceleration is $a_{\max} \approx 10$ m/s^2.

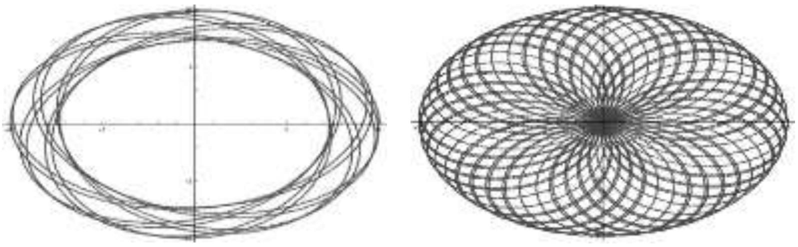

Fig. 5. Trajectory of the motion of inertons in the rotating central field. Parameters for the right figure: $\alpha/\mu = 1$ s^{-2}, $\beta/\mu = 0.5$ s^{-1}; $r(0) = 10$ m, $\dot{r}(0) = 0$, $\varphi(0) = 0$, $\dot{\varphi}(0) = 1$ s^{-1}. Parameters for the left figure: $\alpha/\mu = 1$ s^{-2}, $\beta/\mu = 2$ s^{-1}; $r(0) = 10$ m, $\dot{r}(0) = 0$, $\varphi(0) = 0$, $\dot{\varphi}(0) = 1$ s^{-1}.

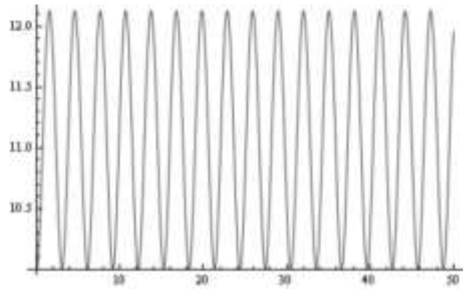

Fig. 6. Velocity $|\dot{\vec{r}}| = \sqrt{\dot{r}^2 + r^2\dot{\varphi}^2}$ of the batch of inertons versus time for the case of the trajectory shown in Fig. 5 (left). The max. velocity is $\upsilon_{\max} \approx 12$ m/s.

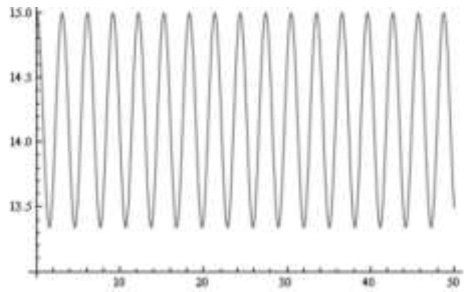

Fig. 7. Acceleration $|\ddot{\vec{r}}| = \sqrt{(\ddot{r} - r\dot{\varphi}^2)^2 + (2\dot{r}\dot{\varphi} + r\ddot{\varphi})^2}$ of the batch of inertons
versus time for the case of the trajectory shown in Fig. 5 (left). The maximal acceleration is $a_{\max} \approx 15$ m/s^2.

In the case of the Newton-type potential, expression (13) changes to

$$U(r,\dot{\varphi}) = -\frac{\gamma}{r} + \frac{\beta}{2} r^2 \dot{\varphi}. \tag{18}$$

Then the equations of motion for the Lagrangian (14) become

$$\ddot{r} - r\dot{\varphi}^2 + \frac{\gamma}{\mu r^2} + \frac{\beta}{\mu} r\dot{\varphi} = 0, \tag{19}$$

$$\ddot{r} - r\dot{\varphi}^2 + \frac{\gamma}{\mu r^2} + \frac{\beta}{\mu} r\dot{\varphi} = 0. \tag{20}$$

the solution to these equations is shown in Fig. 8.

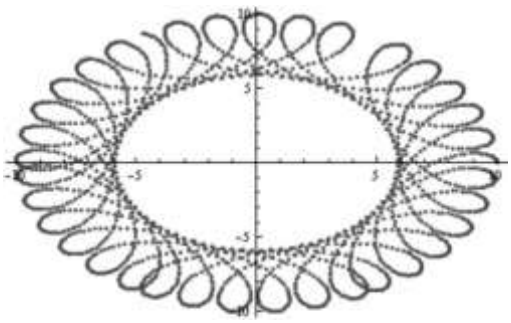

Fig. 8. Trajectory of the motion of inertons in the rotating central field with parameters $\gamma/\mu = 1$ m^3 s^{-2}, $\beta/\mu = 0.1$ s^{-1}; $r(0) = 10$ m, $\dot{r}(0) = 0$, $\varphi(0) = 0$, $\dot{\varphi}(0) = 0.01$ s^{-1}.

In Fig. 9 we show the solution to the equations of motion of a batch of inertons for the case of simplified potential (18), namely, when it is represented only by the Newton-type potential $U(r) = -\gamma/r$.

Figures 4 to 7 give an estimate for the acceleration a of the batch of inertons: $a = 10$ to 15 m/s^2.

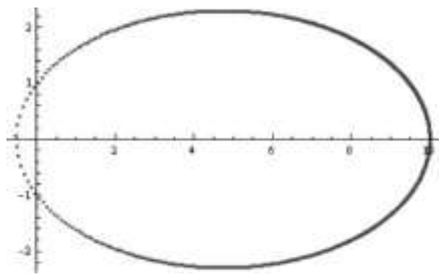

Fig. 9. Elliptic trajectory of the motion of inertons in the Newton-type potential with parameters $\gamma/\mu = 1$ m^3·s^{-2}, $\beta/\mu = 0$ s^{-1}; $r(0) = 10$ m, $\dot{r}(0) = 0$, $\varphi(0) = 0$, $\dot{\varphi}(0) = 0.01$ s^{-1}.

Figures 2, 4, 8 and 9 depict possible patterns of crop circles generated by flows of the mantle-crust inertons.

Let us estimate now the intensity of inerton radiation needed to form a crop circle of total area $A \approx 100$ m^2. Let M_{rocks} be the mass of the mantle-crust rocks that generate inertons owing to their magnetostriction activity. We have to take into account the magnetostriction coefficient C, which describes an extension strain of rocks. In view of the fact of that low frequencies should accompany geophysical dynamical processes, we can assume that the striction activity of a local group of rocks occurs at a low frequency ν (i.e. rocks collide N times per a time Δt of radiation of inertons). Having these parameters, we can evaluate a flow of mass μ_{Σ} that is shot in the form of inerton radiation at the striction of rocks: $\mu_{\Sigma} \approx N\,C\,M_{\text{rocks}}$.

If we put $M \sim 10^7$ kg, $C \sim 10^{-5}$, and $N = 5$ we obtain $\mu_{\Sigma} \approx 500$ kg. This mass μ_{Σ} is distributed along the area of A in the form of a flow of the inerton field. Let each square metre be the ground for the growth of 1000 stalks. Then 10^5 stalks can grow in the area of $A = 100$ m^2. This means that each stalk is able to catch an additional mass $\mu = \mu_{\Sigma}/10^5 = 5$ g from the underground inerton flow; this value is of the order of the mass of a stalk itself.

Knowing the mass $\mu = 5 \times 10^{-3}$ kg of the batch of inertons which interacts with a stalk and the acceleration of this inerton batch $a = 10$ to 15 m/s^2, we can rate the force of inertons that bends and breaks up stalks in the large area A: $F = \mu a \approx 0.05$ to 0.075 N. This estimation exceeds not only the threshold bending force f_{bend} (9), but also the gravity force f_{grav} (10). At the same time the inerton force F does not break physically the stalk, because the value of F still satisfies inequalities (11). Therefore, the model developed in this work is plausible.

A flow of mass, which is coming as a pulse of inertons from the interior of the Earth to its surface, partly compensates the gravitational acceleration at the Earth surface $g = GM_{\text{Earth}}/R^2_{\text{Earth}} = 9.81\,\text{m·s}^{-1}$. This statement can be verified in places where crop circles appear most frequently.

5 Kaleidoscope model

This kaleidoscope model gives a static description of inerton structures. We assume that a bunch of inertons depicted in the centre of Fig. 10 is reflected from the walls, whose geometry was selected rectangular in this particular example. Multiple reflections from the walls produce the pattern shown in Fig. 10. This model can be assumed as an analogy of geometrical optics with light reflecting from the mirrors. Uniting the rotating central field model described in the previous section and the kaleidoscope model can generate yet more complex patterns.

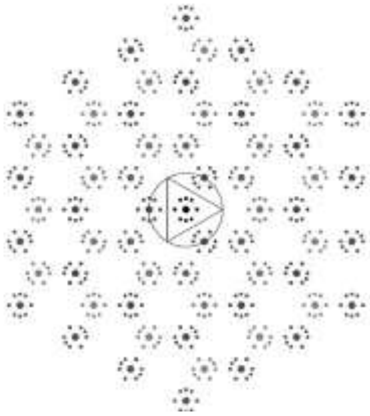

Fig. 10. Kaleidoscope mode

6 Conclusions

In this study we have shown a radically new approach to the conception and description of crop circles. The theory developed is multi-aspect and based on first submicroscopic principles of fundamental physics. The theory sheds light also on fine processes occurring in the crust and the mantle of the terrestrial globe.

The investigation will allow following researchers to improve the mathematical model of the description of shapes of crop circles, to correctly concentrate on biological changes in plants taken from crop circles, to reach more progress in understanding a subtle dynamics of the earth crust, and to contemplate a more delicate approach to the development of new methods of earthquake prediction.

Acknowledge

The authors thank greatly Prof. Christos H. Skiadas for the invitation to take part in the 4th Chaotic Modelling and Simulation International Conference (CHAOS 2011, Agio Nicolaos, Crete, May-June 2011) at which this work was presented.

References

1. W. C. Levengood. Anatomical anomalies in crop formation plants, *Physiologia Plantarum* 92:356-363, 1994.

2. W. C. Levengood and J. Bruke. Semi-Molten Meteoric Iron Associated with a Crop Formation, *J. Scient. Exploration* 9:191-199, 1995. C. H. Skiadas. Two simple models for the early and middle stage prediction of innovation diffusion. *IEEE Trans Eng Manage* 34:79–84, 1987.
3. J. A. Bruke. The physics of crop formations, *MUFON Journal*, October, 3-7, 1998.
4. W. C. Levengood and N. P. Talbott, Dispersion of energies in worldwide crop formations, *Physiologia Plantarum* 105:615-624, 1999. A sigmoid stochastic growth model derived from the revised exponential. In: Janssen J, Skiadas CH (eds) *Applied Stochastic Models and Data Analysis*. World Scientific, Singapore, pp 864–870, 1993.
5. J.-C. Pratsch. Reative motion in geology: some philosophical differences, *J. Petroleum Geology* 13:229–234, 1990.
6. W. H. Munk and G. J. F. Macdonald. *The Rotation of the Earth. A Geophysical Discussion*, Cambridge University Press, London, 1975.
7. H. Jeffreys. *The earth. Its origin, history and physical constitution*, Cambridge University Press, London, 1976.
8. K. Yamazaki. Possible mechanism of earthquake triggering due to magnetostriction of rocks in the crust, *American Geophysical Union, Fall Meeting 2007*, abstract #S33B-1307, Dec. 2007.
9. M. Bounias and V. Krasnoholovets. Scanning the structure of ill-known spaces: Part 1. Founding principles about mathematical constitution of space, *Kybernetes: The Int. J. Systems and Cybernetics* 32:945-975, 2003; arXiv.org: physics/0211096.
10. M. Bounias and V. Krasnoholovets. Scanning the structure of ill-known spaces: Part 2. Principles of construction of physical space, *ibid*. 32:976-1004, 2003; arXiv: physics/0212004.
11. M. Bounias and V. Krasnoholovets. Scanning the structure of ill-known spaces: Part 3. Distribution of topological structures at elementary and cosmic scales, *ibid*. 32:1005-1020, 2003; arXiv: physics/0301049.
12. M. Bounias and V. Krasnoholovets. The universe from nothing: A mathematical lattice of empty sets. *Int. J. Anticipatory Computing Systems* 16:3-24, 2004; arXiv.org: physics/0309102.
13. V. Krasnoholovets. Submicroscopic deterministic quantum mechanics, *Int. J. Computing Anticipatory Systems* 11:164-179, 2002; arXiv: quant-ph/0109012.
14. V. Krasnoholovets. Inerton fields: Very new ideas on fundamental physics, *American Inst. Phys. Conf. Proc*. – Dec. 22, 2010 – Volume 1316, 244-268. Search for fundamental theory: The VII International Symposium Honouring French Mathematical Physicist Jean-Pierre Vigier (12-14 July 2010, Imperial College, London); doi:10.1063/1.3536437.
15. V. Krasnoholovets and J.-L. Tane. An extended interpretation of the thermodynamic theory including an additional energy associated with a decrease in mass, *Int. J. Simulation and Process Modelling* 2:67-79, 2006; also arXiv.org: physics/0605094.
16. V. Krasnoholovets. Variation in mass of entities in condensed media, *Applied Physics Research* 2:46-59, 2010.
17. V. Krasnoholovets, N. Kukhtarev and T. Kukhtareva. Heavy electrons: Electron droplets generated by photogalvanic and pyroelectric effects. *Int. J. Modern Phys. B* 20:2323-2337, 2006; arXiv.org: 0911.2361[quant-ph].

18. L. D. Landau and E. M. Lifshits, *The theory of elasticity*, Nauka, Moscow, 1987, pp. 106-107 (in Russian).
19. G. Skubisz. The dependence of the Young's modulus of winter wheat stalk in various phenological phases, *Proceedings of the 2nd International Conference on physical properties of agricultural materials*, Godollo, Hungary, 26-28 August 1980, Vol. 2., 1980, p. 9.
20. G. H. Dunn and S. M. Dabney. Modulus of elasticity and moment of inertia of grass hedge stems, *Transactions of the ASAE* 39:947-952, 1996.
21. M. Nazari Galedar, A. Jafari, S. S. Mohtasebi, A. Tabatabaeefar, A. Sharifi, M. J. O'Dogherty, S. Rafiee and G. Richard. Effects of moisture content and level in the crop on the engineering properties of alfalfa stems, *Biosystems Engineering* 101: 199-208, 2008.
22. H. Tavakoli, S.S. Mohtasebi and A. Jafari. Effects of moisture content, internode position and loading rate on the bending characteristics of barley straw, *Research in Agricultural Engineering* 55:45-51, 2009.
23. A. Esehaghbeygi, B. Hoseinzadeh, M. Khazaei and A. Masoumi, Bending and shearing properties of wheat stem of alvand variety, *World Applied Sciences J*. 6:28-1032, 2009.

.

Chaotic Modeling and Simulation (CMSIM) 2: 337-344, 2012

Construction of Dynamical Systems from Output Regular and Chaotic Signals

Evgeniy D. Pechuk [1]
Tatyana S. Krasnopolskaya [2]

[1] Institute of Hydromechanics NASU, Kyiv, Ukraine
(E-mail: uzuzun@i.ua)
[2] Institute of Hydromechanics NASU, Kyiv, Ukraine
(E-mail: t.krasnopolskaya@tue.nl)

Abstract: The problem of construction of the deterministic dynamical system from output signals (reconstruction) is very important. Two reconstruction methods have been used and compared. First one is the method of successive differentiation and the second is based on delay coordinates. It was firstly suggested to choose time delay parameter from the stable region of a divergence of the reconstructed system. Results show that both methods can capture regular and chaotic signals from reconstructed systems of the third order with nonlinear terms up to sixth order. Types of signals were examined with spectral methods, construction of phase portraits and Lyapunov exponents.
Keywords: Reconstruction, Dynamical system, Chaotic regime, Successive differentiation, Delay time.

1 Introduction

The problem of reconstruction of deterministic dynamical system from output signals is of great importance in studying of properties of experimental signals such as acoustic signals, ECG, EEG and so on. Reconstructed dynamical system may add a significant qualitative information to chaotic data analysis. Stability conditions, bifurcation curves, all types of steady – state regimes could be studied for solutions of a reconstructed system. Two reconstruction methods have been developed by Crutchfield and McNamara [1] and used for variety of signals later [2-4]. The first method is based on suggestion that the signal can be presented by a function that has at least three derivatives, so this is method of successive differentiation. Applying this method the dynamical system has a following form [1-4]:

$$\begin{aligned}\dot{x}_1 &= x_2\\ \dot{x}_2 &= x_3\\ \dot{x}_3 &= F_3(x_1, x_2, x_3)\end{aligned}$$

Received: 11 July 2011 / Accepted 30 March 2012

ISSN 2241-0503

where $F_3(x_1, x_2, x_3)$ is a nonlinear function. The second method of reconstruction is based on delay coordinates. We need to reconstruct the dynamical system from the time series of some state variable $x(t)$ with the fixed sampling step dt. We have series of $s_k = x(kdt)$, $k=0,1,2,...,N$, using value of time delay $\tau = ndt$ (which is chosen to yield optimal reconstruction [1]) we construct the dynamical system in the form [1-4]:

$$\begin{aligned} \dot{x}_1 &= F_1(x_1, x_2, x_3) \\ \dot{x}_2 &= F_2(x_1, x_2, x_3) \\ \dot{x}_3 &= F_3(x_1, x_2, x_3) \end{aligned}$$

where $x_1(t) = x(t)$; $x_2(t) = x(t+\tau)$; $x_3(t) = x(t+2\tau)$, $F_i(x_1, x_2, x_3)$ are nonlinear functions.

2 Construction of Dynamical Systems from Output Signals of Pendulum System

Reconstruction methods are applied to the signals of a deterministic dynamical system of pendulum oscillations which may have regular and chaotic regimes [5]**:**

$$\begin{aligned} \dot{y}_1 &= -0.1y_1 - y_2 y_3 - \frac{1}{8}(y_1^2 y_2 + y_2^3) \\ \dot{y}_2 &= -0.1y_2 + y_1 y_3 - \frac{1}{8}(y_2^2 y_1 + y_1^3) + 1 \\ \dot{y}_3 &= -0.5y_2 - 0.61y_3 + F \end{aligned}$$

Nonlinear functions $F_i(x_1, x_2, x_3)$ in the first and second systems have the following form:

$$F(x_1, x_2, x_3) = a + \sum_{i=1}^{3} a_i x_i + \sum_{i,j=1}^{3} a_{ji} x_j x_i + ... + \sum_{o,m,n,k,j,i=1}^{3} a_{omnkji} x_o x_m x_n x_k x_j x_i$$

with nonlinear terms up to third order for the regular signals and up to the six order for the chaotic.

The traditional way to obtain time delay parameter $\tau = ndt$ for the second method of reconstruction is to use time interval when the autocorrelation function is equal to zero [2-4]. For such chosen τ the divergence of a reconstructed system may not be negative. So that we introduce other way to choose τ . Real system is nonconservative and, the divergence of systems should be negative too. For example, for the original pendulum system div is equal to -0.81. In Figure 1 the dependence of reconstructed systems divergence on n in the steady – state regimes is shown. We choose n for time delay τ from the stable region of div .

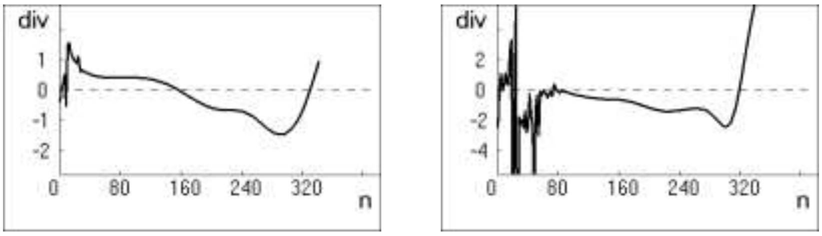

a) b)

Fig. 1. The dependence of reconstructed systems divergence on n for regular initial signal $F = 0.257$ (case a) and chaotic $F = 0.114$ (case b).

For every value of the bifurcation parameter F from the interval $0.1 \le F \le 0.3$ the reconstructed systems were built and the output signals were determined. And then the largest Lyapunov exponents [6] were calculated. For that purpose we use the fifth – order Runge – Kuttas method with the precision of $O(10^{-7})$. Initial conditions were selected in the vicinity of the original signal, and for the steady – state regime signals we choose $N = 2^{18}$, $dt = 0.004$.

The dependence of the largest Lyapunov exponent of the pendulum system on values of the bifurcation parameter F is shown in Figure 2.a. The dependences of the largest Lyapunov exponent on F for the first and the second reconstructed dynamical systems are shown in Figure 2.b – c correspondingly.

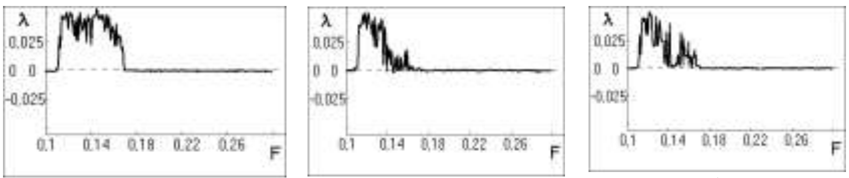

a) b) c)

Fig. 2.The largest Lyapunov exponent of the pendulum system (case a) and of the reconstructed systems (cases b and c).

,

We may see similarity of both graphs to the dependence for the original system in Figure 2.a with the exception of the region $0.15 \le F \le 0.18$ where the transition to chaos occurs.

2 Construction Systems from Regular Output Signal

As was shown in the book [5] the solution of the pendulum system would be regular if bifurcation parameter is F=0.257. We used this value and solved the system in order to get the output signal. Then we reconstruct the system using the two methods.

For the second method we reconstruct the system using small initial value for the delay parameter and build the dependence of the divergence on value n and choose n from the stable interval of the delay parameter (Figure 1.a, n=240). As the result the system get the form with nonlinear terms only to the third order of nonlinearity.

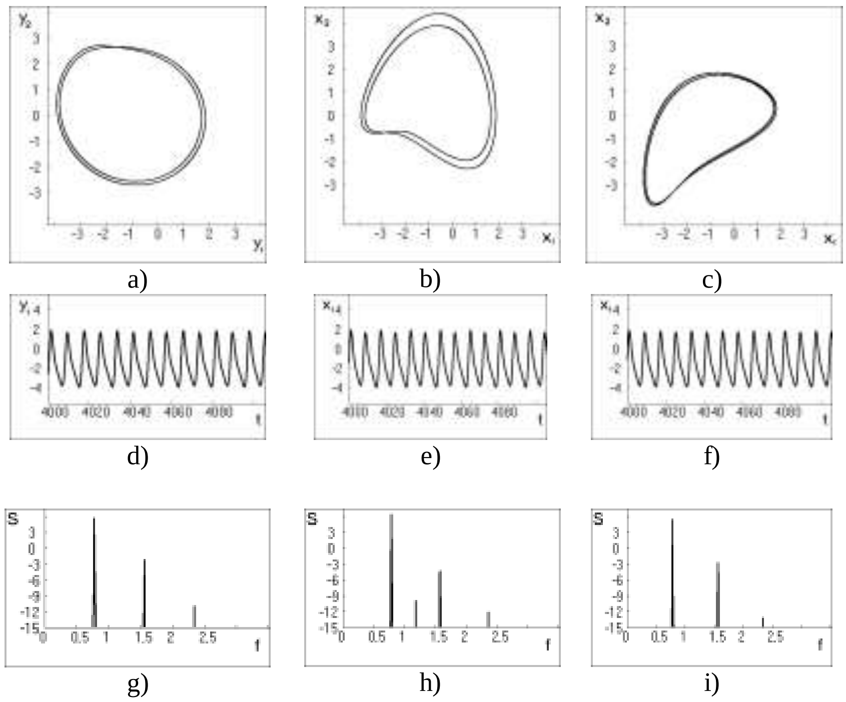

Fig. 3. The portrait of initial pendulum system (F=0.257), case a , the portraits of the reconstructed systems, cases b–c, their time realizations, cases d–f, and power spectrums, cases g–i.

Projections of the limit cycle with two loops on the plane are shown in Figure 3. a–c for the solution of the original system (Figure 3.a) and the reconstructed first and second dynamical systems (Figure 3.b–c). Since for reconstruction we use only the first variable signal phase portrait projections on the plane with the second variable only qualitatively are look like the original limit cycle with two loops. Time realizations of the first variable and their power spectrums are presented in Figure 3.d–i. Figure 3.d and Figure 3.g describes the solution of the original system, and Figure 3.e–f and Figure 3.h– i gives the information about solutions of the reconstructed dynamical systems.

Since power spectrum indicates the power contained at each frequency, the peak heights corresponds to the squared wave amplitudes (i.e. the wave energy) at the corresponding frequencies. The first method of reconstruction gives the solution which the power spectrum for the regular signals coincides with the output signal power spectrum up to 96% for the first three peaks. The second method gives the precision up to 98%. Also the second method determines the maximum Lyapunov exponent more precisely for chaotic regimes (with a precision to $O(10^{-3})$) than the first method.

3. Construction Systems from Chaotic Output Signal

Now we use such parameter F for the pendulum original system when this system has the chaotic solution, namely F=0.114. Then we reconstruct the system using the two methods of reconstruction with nonlinear function $F_i(x_1, x_2, x_3)$ with nonlinear terms up to the sixth order. For the second method we reconstruct the system using small initial value for the delay parameter and build the dependence of the divergence on value n and choose n from the stable interval of the delay parameter (Figure 1.b, n=240).

Projections of the chaotic attractor of the initial system and of the reconstructed systems are shown in Figure 4.a–c. As could be seen from Figure 4 the both methods qualitatively good approximate chaotic attractor of the original system. Time realizations of the chaotic attractors after finished transient regimes are also similar and given in Figure 4.d–f. Power spectrums for the original signal and for the signals from the reconstructed systems are shown in Figure 4.g– i and may be approximated by the same decay function $S = -6.75 - 8.5f$.

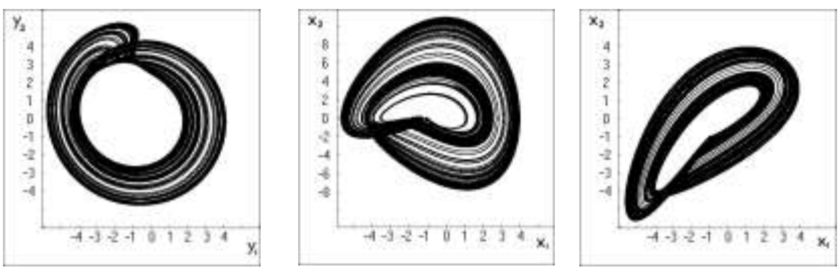

a) b) c)

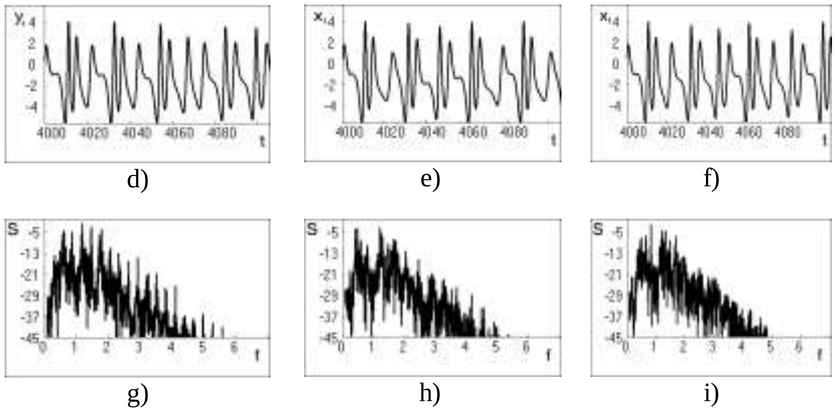

Fig. 4. The portrait of initial system (case a) (F=0.114), the portraits of the reconstructed systems (cases b –c), their time realizations (d –f) and power spectrums (g–i).

3 Construction System from Synthetic ECG Signal

As practical application of the considered methods the signal of a dynamical model for generating synthetic electrocardiogram signals [9] was used. This signal is regular and outwardly looks like the electrocardiogram of healthy man. Using the method of delay the system of eighth order was built. In Figure 5 temporal realization is represented by synthetic electrocardiogram. In Figure 6 temporal realization of the first coordinate of the solution of the reconstructed system is represented. As is obvious from graphs both signals are regular and have an identical period of oscillations.

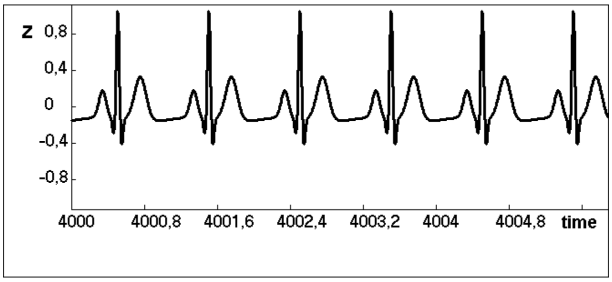

Fig. 5. Synthetic electrocardiogram signal.

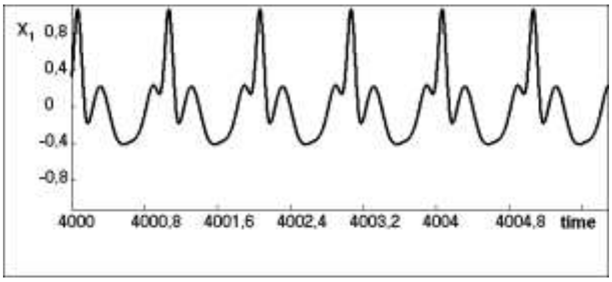

Fig. 6. Signal generated by reconstructed system.

4 Conclusions

Results show that both methods can capture regular and chaotic signals from reconstructed systems of the third order with nonlinear terms up to sixth order. Types of signals were examined with spectral methods, construction of phase portraits and Lyapunov exponents. The first method gives the solution which the power spectrum for the regular signals coincides with the output signal spectrum up to 96 % for the first three peaks. The second method gives a mistake around 2 %. And the second method determines the maximum Lyapunov exponent more precisely for chaotic regimes (with a precision to $O(10^{-3})$) than the first method.

Real systems are nonconservative and, a divergence of systems should be negative. It was suggested for the first time that the delay parameter for the second reconstruction method must be chosen from the stable region of the divergence behaviour of the reconstructed system.

The both methods qualitatively good approximate the phase portrait of chaotic attractor of the original system. Moreover, time realizations of the chaotic attractors after finished transient regimes are quiet similar. And what is more important, power spectrums for the original signal and for the signals from the reconstructed systems may be approximated by the same decay function $S = -6.75 - 8.5 f$. Calculations also show that more precisely the value of bifurcation parameter for chaotic regimes gives the second method of reconstruction.

References

1. J. P. Crutchfield, B. S. McNamara. Equations of Motion from a Data Series, *Complex Systems*, vol. 1, 417-452, 1987.
2. N. B. Janson, A. N. Pavlov, T. Kapitaniak, V. S. Anishshenko. Reconstruction of the dynamical systems from the short signals, *Letters into JTP*, vol. 25, no. 11, 7-13, 1999.
3. V. S. Anishshenko. *Acquaintance with nonlinear dynamic,*. Institute of Computer Science, Moscow-Izhevsk, 2002.
4. S. P. Kouznetsov. *Dynamic chaos*, Physmatlit, Moscow, 2001.

5. T. S. Krasnopolskaya, A. Yu. Shvets. *Regular and chaotic dynamics of the systems with limited excitation*,. Institute of Computer Science, Moscow-Izhevsk, 2008.
6. G. Benettin, L. Galgani, J. M. Strelcyn. Kolmogorov entropy and numerical experiments, *Phys. Rev.*, vol. 14, 2338-2345, 1976.
7. M. B. Kennel, R. Brown and H. D. I. Abarbanel. Determining embedding dimension for phase-space reconstruction using a geometrical construction *Phys. Rev. A.*, vol. 45, no. 6, 3403-3408, 1992.
8. V. S. Anishshenko, A. P. Pavlov. Global reconstruction in application to multichannel communication *Phys. Rev. E.*, vol. 57, no. 2, 2455-2458, 1998.
9. P. E. McSharry, G. D. Clifford, L. Tarassenko, L. A. Smith. A dynamical model for generating synthetic electrocardiogram signals, *IEEE Transactions on biomedical engineering*, vol. 50, no. 3, 289-294, 2003.

Chaotic Modeling and Simulation (CMSIM) 2: 345–354, 2012

On the Computation of the Kantorovich Distance for Images

Constantinos Alexopoulos[1] and Vassileios Drakopoulos[2]

[1] University of Athens, Panepistimioupolis, 15784 Athens, Greece
(E-mail: calexop@di.uoa.gr)
[2] University of Athens, Panepistimioupolis, 15784 Athens, Greece
(E-mail: vasilios@di.uoa.gr)

Abstract. We consider the theory and applications of the Kantorovich metric in fractal image compression. After surveying the most important approaches for its computation, we highlight its usefulness as a mathematical tool for comparing two images and improve its performance by means of more appropriate data structures.
Keywords: Fractals, Hutchinson metric, Image comparison, Kantorovich metric.

1 Introduction

In many fields of computer science like pattern recognition and image processing, it is important to have an efficient way to compare geometric objects. The natural approach to this problem is to define a metric in the space of the geometric objects and use this metric to compute the distance between them. Considering digitized images as geometric objects, we can use that metric to compare them.

The *Kantorovich* (or *Hutchinson*) *metric*, a.k.a. Wasserstein (or Vasershtein), earth mover's or match metric, takes into account the spatial structure of the compared images and, hence, corresponds more closely than other metrics to our notion of the visual differences between two images. John E. Hutchinson[6] used the Kantorovich distance to measure the distance between self-similar probability measures obtained as limiting distributions for a fairly simple type of Markov chains induced by affine, contractive mappings. He used the Kantorovich metric to prove an existence and uniqueness theorem of such limit measures.

The Kantorovich metric is also used by Michael F. Barnsley[2] and coworkers to approach the convergence of *iterated function systems*, which were introduced by Hutchinson. In trying to solve the so-called "inverse problem" or "image encoding problem", i.e. find an IFS that generates a predetermined image, it is natural to use this metric as an objective function to be minimised. Moreover, this metric appears to be a good indicator of the perceived difference between two images.

Received: 20 July 2011 / Accepted: 30 March 2012

ISSN 2241-0503

Considering digitized images as a set of pixels, the problem of computing the Kantorovich distance between them is equivalent to the formulation of a *linear programming problem* called the *balanced transportation problem*. According to Michael Werman *et al.*[9] the computational complexity of standard algorithms for transportation problems are of order $O(N^3)$, where N denotes the total number of pixels in the compared images. An algorithm for the computation of the Hutchinson metric in the case of finite one-dimensional sequences is presented in [3].

Thomas Kaijser[7] presented a variation of the primal-dual algorithm for computing the Kantorovich distance function. To decrease the computational complexity for updating the values of the dual variables for both transmitting and receiving images, he always increases them by a constant value of 1. Unfortunately, this is applicable, only if the underlying pixel distance value is the L_1-metric. Moreover, he developed two methods for fast determination of new admissible arcs, one for the L_1-metric and one for the L_2-metric. Kaijser's method was implemented by Niclas Wadströmer[8] in the context of his PhD thesis, but the data structures used to implement the above mentioned method as well as the way that the labelling procedure was implemented are not so clear.

Another work on the computation of the Kantorovich distance is the one of Drakopoulos V. *et al.*[5]. In this work the problem of computing the Kantorovich distance is transformed into a linear programming problem which is solved using the simplex method. To decrease the computational complexity of the method, they developed an approximation algorithm for "large images". Yuxin Deng *et al.*[4] give a brief survey of the applications of the Kantorovich distance in probabilistic concurrency, image retrieval, data mining and bioinformatics.

The main purpose of the present paper is to improve the algorithm presented by Thomas Kaijser for computing the Kantorovich distance function by means of more appropriate data structures. The metric we are using as the underlying distance-function between pixels is the L_1-metric. Using kd-trees we don't have to use different methods, but only to change the metric for the construction of the appropriate kd-tree.

2 Problem Formulation

We are interested in computing the *Kantorovich distance* between grey-scale images. There are three types of image models: Measure spaces, pixelated data and functions. Using this approach, we consider an image as a measure space. Therefore, by an image P with support K we mean an *integer-valued* nonnegative function $p(i,j)$ defined on K, i.e. $P = \{p(i,j) : (i,j) \in K\}$. We define as a *Borel measure* on the space of grey-scale images the *pixel value* $p(i,j)$, where i and j are the Cartesian coordinates of the pixel.

For a compact metric space (X,d), let P_1 and P_2 be two Borel probability measures on X and define $\Theta(P_1,P_2)$ as the set of all probability measures P on $X \times X$ with *fixed marginals* $P_1(\cdot) = P(\cdot \times X)$ and $P_2(\cdot) = P(X \times \cdot)$. Next, let

$$\mathrm{Lip}(X) = \{f\colon X \to \mathbb{R} \,\big|\, | f(x) - f(y) | \leq d(x,y), \forall x, y \in X\}$$

and define the distance between P_1 and P_2 as

$$B_d(P_1, P_2) = \sup \left\{ \left| \int_X f(x) P_1(dx) - \int_X f(x) P_2(dx) \right|, f \in \mathrm{Lip}(X) \right\}.$$

The images considered are sets of finite collection of pixels, so they constitute compact metric spaces.

Let K_1 and K_2 be two images, S_n, $1 \leq n \leq N$ be the pixels of K_1 and R_m, $1 \leq m \leq M$ the pixels of K_2. Using the terminology of Kaijser we call K_1 the *transmitting image* and K_2 the *receiving image*; S_n, $1 \leq n \leq N$ denote *sources* whereas R_m, $1 \leq m \leq M$ denote *sinks* or *destinations*. By a *flow* we mean the amount of goods sent from the source S_n to the sink R_m denoted by $x(n,m)$ whereas $c(n,m)$, $1 \leq n \leq N, 1 \leq m \leq M$ denote the cost of transferring goods from S_n to R_m. In our case the cost corresponds to the distance between S_n and R_m. If $a(n)$ denote the amount of goods available in a source and $b(n)$ the amount of goods needed in a sink, the Kantorovich distance between K_1 and K_2 can be formulated as a balanced transportation problem as follows:

$$\text{Minimize} \sum_{n=1}^{N} \sum_{m=1}^{M} c(n,m) \cdot x(n,m)$$

subject to $x(n,m) \geq 0, 1 \leq n \leq N, 1 \leq m \leq M$,

$$\sum_{m=1}^{M} x(n,m) = a(n), \quad 1 \leq n \leq N \tag{1}$$

$$\sum_{n=1}^{N} x(n,m) = b(m), \quad 1 \leq m \leq M \tag{2}$$

and

$$\sum_{n=1}^{N} a(n) = \sum_{m=1}^{M} b(m).$$

The distance can be any of the following distances: L_1-metric or L_2-metric. For each source and each sink we define two quantities $\alpha(n)$ and $\beta(m)$ respectively, called *dual variables*. If

$$c(n,m) - \alpha(n) - \beta(m) \geq 0, \quad 1 \leq n \leq N, 1 \leq m \leq M,$$

we call the set of dual variables *feasible*. A pair of indices (n,m), where n is an index of a source S_n and m is an index of a sink R_m, is called an *arc*. If an arc (n,m) satisfies the condition

$$d(n,m) - \alpha(n) - \beta(m) = 0, \tag{3}$$

where $d(n,m)$ is the underlying distance-function between the pixels S_n and R_m, it is called an *admissible arc*; otherwise it is called *nonadmissible*. We say that a flow is *optimal* if Equations (2) and (3) hold.

The dual version of the transportation problem, i.e. the dual formulation of the Kantorovich distance, is

$$d_K(P,Q) = \mathrm{Max}\left\{ \sum_{n=1}^{N} \alpha(n) \cdot a(n) + \sum_{m=1}^{M} \beta(m) \cdot b(m) \right\} \tag{4}$$

when the set of dual variables is feasible.

3 The proposed algorithm

Our algorithm is based on the well known *primal-dual algorithm* which solves the balanced transportation problem on the plane. We make several enhancements, however, that improve the efficiency of the algorithm. Our improvements are based on the data structures used to store image data and on the fact that the transportation cost is the distance between the pixels. The latter allows us to use some spatial data structures which facilitate the computations and minimise the complexity of the problem. Before describing our method in detail, we give the main steps of the primal-dual algorithm:

1. Determine an initial value of the dual variables, find the corresponding set of admissible arcs and their flow.
2. Check if the current admissible flow is maximal. If it is go to (4), else go to (3).
3. Update the admissible flow and go to (2).
4. Check if the current maximal flow is optimal. If it is go to (7), else go to (5).
5. Update the dual variables.
6. Find the new admissible arcs and go to (2).
7. Stop.

Let us define as *total transporting grey mass* the summation of the grey value of all pixels in the transporting image. Similarly, we define as *total receiving grey mass* the summation of the grey value of all pixels in the receiving image. In order to convert the Kantorovich distance problem between images to a balanced transportation problem on the plane, both transporting and receiving total grey values must be equal. In general, these two amounts are different and in order to make them equal we change both masses accordingly applying the following formula on every single pixel value of both images:

$$p_{new}(n) = p(n) \cdot \hat{L}(K_2), \quad \hat{L}(K_2) = \Big[\sum_{m=1}^{M} q(m) \Big] / GCD(L,Q),$$

$$q_{new}(m) = q(m) \cdot \hat{L}(K_1), \quad \hat{L}(K_1) = \Big[\sum_{n=1}^{N} p(n) \Big] / GCD(L,Q),$$

where $p(n)$ and $q(m)$ are the pixel values of the transmitting and receiving images respectively, $L = \sum_{n=1}^{N} p(n)$, $Q = \sum_{m=1}^{M} q(m)$ and $GCD(L, Q)$ is the greatest common divisor of L and Q. In the following we shall describe our algorithm as well as the data structures we use to facilitate our computations and image storage.

3.1 Dual variables and the flow of the current admissible arcs

After having made the total grey masses of both images equal we have to initialise the dual variables. We set as initial values $\alpha(n) = \min\{d(n,m), 1 \leq m \leq M\}, i \leq n \leq N$ and $\beta(m) = 0, 1 \leq m \leq M$. From the above equations we observe that the initial values of the dual variables $\alpha(n)$ associated with the transmitting image pixels are the distances of their nearest neighbour pixels in the receiving image. In order to compute this quantity we create a kd-tree structure using the coordinates of the receiving image pixels and we search for the nearest neighbour of every single transmitting pixel. So, if n is a transmitting pixel and m one of its nearest neighbours in the receiving image, then (n, m) is an admissible arc. Therefore, the initial flow along this arc is $x(n, m) = \min\{p(n), q(m)\}$, whereas the new pixel values are $p(n) - x(n, m)$ and $q(m) - x(n, m)$.

3.2 Increasing the flow along the current set of admissible arcs

We call *surplus source* a transmitting pixel with $p(n) > 0$; otherwise, it is called a *zero source*. A receiving pixel having $q(m) > 0$ is called a *deficient sink*; otherwise, it is called *zero sink*. We define as *augmenting path* a set of admissible arcs connecting sources and sinks starting from a surplus source and ending with a deficient sink running through zero sinks and sources interchangeably. Moreover, the flow along admissible arcs connecting zero sinks with zero sources must be positive. In this step we use a labelling procedure to determine augmenting paths. It is clear that we can have flow increment only along augmenting paths. The labelling procedure is described as follows.

Start by labelling all surplus sources and then label all sinks that are connected to those sources with admissible arcs. Then, using the last labelled sinks, label all sources that are not labelled yet and are connected to those sinks with admissible arcs of positive flow. Repeat the above procedure until either a deficient sink is labelled or no more nodes can be labelled. If a deficient sink is labelled, then proceed to flow augmentation along the path that has been found. If no such path is found, the current admissible flow is maximal. For faster labelling procedure, we don't use any extra data structure. We reorder the pixels of both the transmitting and the receiving image in the initial data structure depending on whether they are labelled or unlabelled. To speed up the reordering process, we store the pixel data in doubly linked lists which need $O(1)$ to move the nodes along the list.

http://www.cs.umd.edu/∼mount/ANN/

Let $\theta_1 = \min\{x(m,n)\}$ be the minimum value of the positive flows belonging to the augmenting path connecting a labelled source and a label sink directed from sink to source. We define by

$$\theta = \min\Big\{a(n) - \sum_{j=1}^{M} x(n,j), b(m) - \sum_{i=1}^{N} x(i,m), \theta_1\Big\}.$$

Then, we can increase the flow along the path by setting the value of the starting source pixel to $p(n) - \theta$, the value of the ending sink to $q(m) - \theta$, by increasing the flows directed from source to sink by θ and by decreasing the flows from sink to source by the same amount. A drawback of this labelling procedure is that, after increasing the flow along an augmenting path, we may obtain *cycles*. In order to avoid them, we change the way we apply the labelling procedure by using only positive admissible arcs during the whole procedure. In that way, however, we cannot find all the augmenting paths. So, we use a *flow tuning procedure* which finds all possible augmenting paths for the current set of admissible arcs without having to store and use all the zero flow admissible arcs.

3.3 Flow tuning procedure

We define as *surplus flow tree* a set of paths starting from a surplus source and ending to zero sinks. A *zero flow tree* is a flow tree with a zero source as starting node. The main purpose of the flow tuning procedure is to find admissible arcs that connect zero sources belonging to surplus flow trees and unlabelled deficient sinks. To do that, a kd-tree is constructed using the coordinates of the unlabelled deficient sinks. Then, using the kd-tree structure for each zero source belonging to a surplus flow tree, we locate all the deficient unlabelled sinks that lay within a distance $\alpha(n)$ from itself. After that, a new augmenting path has been located and the flow is augmented as described in the previous subsection. According to the definition of the augmenting path, there is no reason to search for arcs that connect zero sources that belong to zero flow trees with unlabelled zero sinks. In such a way we decrease the number of sinks as well as the number of considered sources. The first one leads to a faster construction of the kd-tree whereas the second one minimises the number of input points.

3.4 Dual variable update and the new set of admissible arcs

When no more augmenting paths can be located for the current set of admissible arcs, we proceed to the dual variable update procedure. The main reason for updating the dual variables associated with both sources and sinks is to create new admissible arcs in order to achieve the maximal and also the optimal flow. According to Kaijser[7], if the underlying metric is the L_1-metric, the dual variable can be changed by $\delta = 1$. In order to preserve the current flow along the current set of admissible arcs, the dual variables are changed as follows:

$$\alpha_{new}(n) = \alpha_{old}(n) + \delta, \quad n \in M_1, \quad \alpha_{new}(n) = \alpha_{old}(n), \quad n \in U_1,$$

$$\beta_{new}(m) = \beta_{old}(m) - \delta, \quad m \in M_2, \quad \beta_{new}(m) = \beta_{old}(m), \quad m \in U_2,$$

where M_1 and M_2 denote the sets of indices of labelled sources and sinks, respectively, whereas U_1 and U_2 denote the sets of indices of unlabelled sources and sinks, respectively. To improve the dual variable update, we define a new variable Δ as the running total of the dual variable changes as the algorithm evolves; see also [1]. We apply the above mentioned dual variable change routine using Δ instead of δ. Because of the way we change the dual variables, new positive flow admissible arcs are created between the labelled surplus sources and the unlabelled deficient sinks. To find out the new set of admissible arcs, a kd-tree is constructed using the coordinates of the unlabelled deficient sinks. Then, for each surplus source, we locate all the deficient sinks that lay within a distance of $\alpha(n) + \Delta$ from it. After finding out the new set of positive flow admissible arcs, the algorithm is applied again until no more surplus nodes exist.

4 Results

We now present typical results from the application of our algorithm to real images, aiming to demonstrate its applicability to the demanding problems inherent in the image compression area and its performance. The original images used as our reference point in the experiments presented here are the $256 \times 256 \times 8$ bpp Lena and Barbara images shown in Figure 1. We examine

Fig. 1. The original images of Lena (left) and Barbara (right) used in our experiments ($256 \times 256 \times 8$ bpp).

for each original image how close it is to a filtered or compressed replica of it. In other words we seek to measure the difference (i.e. the error) between two images by computing the Kantorovich distance between the original image and each of the associated filtered ones.

The compression schemes used in our simulations for the image of Lena include a *wavelet scheme* (Figure 2(a)), which represents a generic and efficient


(a) (b)

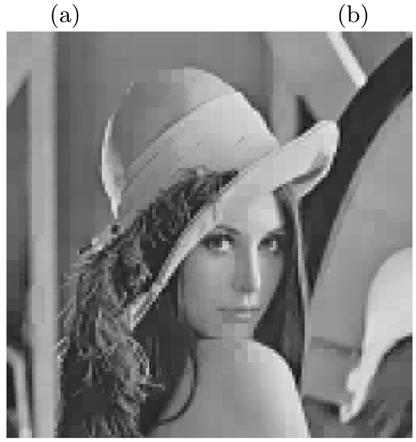

(c)

Fig. 2. $256 \times 256 \times 8$ bpp test images used in our experiments ((a)wavelet, (b) JPEG and (c) fractal 8:1 compression are used).

solution to the perfect inversion problem, a Joint Photographic Experts Group (JPEG) codec in its Corel 7 implementation (Figure 2(b)) and a fractal scheme of 8:1 compression ratio (Figure 2(c)). Figure 3 shows compressed images of

	μ, μ_1	μ, μ_2	μ, μ_3	ν, ν_1	ν, ν_2	μ, ν
d_K	2,789,456	8,562,357	4,532,730	3,125,789	8,998,678	15,853,930
t_K	26:06	40:12	39:10	29:30	42:56	1:01:46

Table 1. The Kantorovich distance d_K between the real-world images and the computation time in hour:min:sec format.

Barbara at a ratio of 64:1 using (9,7) DWT combined with RLE and JPEG coding respectively. The correspondence between the images of Lena and the indices is the following: μ = original image, μ_1 = wavelet compression, μ_2 = JPEG compression and μ_3 = 8:1 fractal compression. The correspondence

(a) (b)

Fig. 3. 256 × 256 × 8 bpp test images used in our experiments ((a) EZW Shapiro (9,7) and (b) JPEG compression are used).

between the images of Barbara and the indices is the following: ν = original image, ν_1 = 64:1 compression and ν_2 = JPEG compression. Time results are given in CPU minutes on a Core$^{\mathrm{TM}}$ 2 Duo PC with a 2.13 GHz CPU clock, 4 GB RAM and running Windows 7 Ultimate. Looking at Table 1 from left to right we can see, which of the images are closer to the originals. The runtime of our algorithm is better than the one presented in [7].

5 Conclusions

The theory and applications of the Kantorovich metric were considered. A model based on the primal-dual algorithm was formulated and developed. The results support the well known fact that the Kantorovich metric unveils the imperfections of apparently similar images.

References

1.D. S. Atkinson and P. M. Vaidya. Using geometry to solve the transportation problem in the plane. *Algorithmica* 13:442461, 1995.

2.M. F. Barnsley. *Fractals everywhere*, 2nd ed., Academic Press Professional, San Diego, 1993.

3.J. Brandt, C. Cabrelli and U. Molter. An algorithm for the computation of the Hutchinson distance. *Information Processing Letters*, 40:113–117, 1991.

4.Y. Deng and W. Du. The Kantorovich metric in Computer Science: A brief survey. *Electronic Notes in Theoretical Computer Science*, 253:73–82, 2009.

5.V. Drakopoulos and N. P. Nikolaou. Efficient computation of the Hutchinson metric between digitized images. *IEEE Transactions on Image Processing*, 13:1581–1588, 2004.

6.J. E. Hutchinson. Fractals and self similarity. *Indiana University Mathematics Journal*, 30: 713–747, 1981.

7.T. Kaijser. Computing the Kantorovich distance for images. *Journal of Mathematical Imaging and Vision*, 9:173–191, 1998.
8.N. Wadströmer. Coding of fractal binary images with contractive set mappings composed of affine transformations, *PhD thesis*, Linköping University, 2001.
9.M. Werman, S. Peleg and A. Rosenfeld. A distance metric for multidimensional histograms. *Computer Vision Graphics Image Processing*, 32:328–336, 1985.

Simulation of Content-Driven Cosmic Expansion

John F. Kastl[1]

[1] US Navy, Keyport WA USA
(email: john.kastl@navy.mil)

Abstract: The standard cosmic expansion model, in which gravity acts to decelerate the expansion, has its problems. This paper explores an alternative model, which has a content-driven mechanism, and in which gravity does not play a role in the overall expansion. Cosmic expansion was simulated with a three-step iterative algorithm, three fundamental parameters, and Planck-scale initial conditions. Model characteristics include self-regulated expansion, causal mechanisms for the Big Bang and Inflation, non-zero and non-fundamental time (t), parametric Ht (the product of t and the Hubble parameter (H)), a dynamic deceleration parameter (q), Ht lagging $(1+q)^{-1}$, and attractors in the q-Ht phase diagram. Simulation results support refinement of the standard model and open the door for similarly exploring and comparing other cosmic expansion models.
Keywords: cosmology, modeling, simulation, complex systems

1 Introduction

Proponents of the most generally accepted cosmic expansion model (the standard model) posit that gravity has acted to decelerate the expansion since the Universe burst forth from a singularity at time zero (Shu 1982). The expansion metric is the scale factor (R), which has units of length. The metric for the deceleration is the dimensionless deceleration parameter ($q \equiv -a\cdot\ddot{a}/\dot{a}^2$, where $a=R/R_{now}$).

The standard model has its issues, including singularity-generated infinities at time zero, its false premise (Gimenez 2009) that gravity plays a role in the overall expansion, and its lack of causal mechanisms for the Big Bang and Inflation. Also, accelerated expansion, as indicated by supernovae observations (Riess et al. 1998, Perlmutter et al. 1999), cannot be found in the standard model. Saul Perlmutter (2003), referring to fine tuning coincidences and the mysterious substances of dark energy and dark matter, writes that it seems likely that we are missing some fundamental physics and one is tempted to speculate that these ingredients are add-ons, like the Ptolemaic epicycles, to preserve an incomplete theory.

This paper explores a content-driven approach to cosmic expansion and argues that indications of current acceleration are in error. An iterative algorithm, which focuses on Mach's Principle, the past lightcone, and an hypothesis that the increasing content on our past lightcone provides the causal mechanism for cosmic expansion, is constructed to numerically simulate cosmic expansion. The Big Bang is simulated at Planck time and Inflation is found in the Matter Era.

Received: 21 August 2011 / Accepted 30 March 2012

ISSN 2241-0503

2 The Model and Simulations

2.1 Ansatz

The guiding principles in this effort to simulate cosmic expansion were to keep the algorithm simple and use only assumptions and mechanisms that reflect fundamental realities. This was done in part by using natural c=1 units and adhering to Mach's Principle and Einstein's Locality Principle, which in turn placed the focus on local time and the past lightcone.

Einstein coined the term Mach's Principle (MP) and, although he attempted to incorporate MP into General Relativity (GR), his attempt is believed by some theorists to have failed. This lack of a consensus is due in part to the lack of a widely accepted definition for MP. As used here, MP is a take on Mach's reference to the 'fixed stars': The content on our past lightcone defines our inertial reference frame, and that content is finite and increasing with time.

Einstein wrote 'Space without material object is inconceivable' (Jammer 1953), and Gottfried Leibniz before him wrote 'Where there is no matter, there is no space' (Harrison 2000). With MP and the past lightcone in mind, this space-content connection is extrapolated into an hypothesis that cosmic expansion is connected to the increasing amount of content (Γ) on our past lightcone, yielding $R=R_0 \cdot \Gamma^{\varepsilon}$, where ε is an expansion exponent.

2.2 Algorithm.

The algorithm for content-driven expansion (figure 1) is iterative and discreet and does not require Nature to understand complex math or perform massive computations. Time (t), which was neither in the iterative loop nor one of the three fundamental parameters, was progressed using $\Delta t=R/c$, where R is the cosmic scale factor and c is the speed of light.

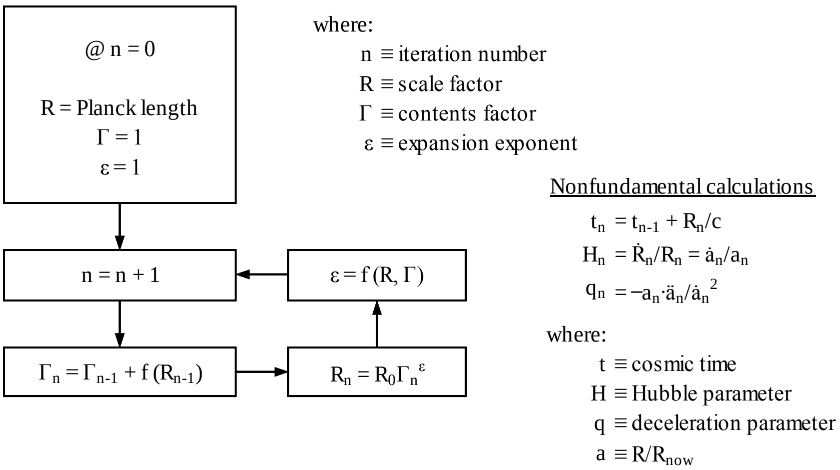

Figure 1. Iterative expansion algorithm. The three fundamental parameters (R, Γ, and ε) are in the three-step iterative loop. With R_0 set to Planck length, t_0=Planck time, $\dot{R}_0=c$, $H_0=1/t_0$, $Ht_0=1$, $\ddot{a}_0=0$, and $q_0=0$.

2.3 Progressing time with $\Delta t=R/c$

R/c is the time for light to traverse the distance R. With R_{now}=~20Mly, Δt_{now} (today's tick of the clock) is ~20My ($\Delta t=R/c$). Midway through the development of the simulation, $\Delta t=R/c$ was replaced when a more supportable method was found in $\Delta t=\Delta R/R/H$, which follows from $H\equiv\dot{R}/R$. Surprisingly, replacing $\Delta t=R/c$ with $\Delta t=\Delta R/R/H$ had no impact on the simulation, and the simpler $\Delta t=R/c$ was reinstated.

For an object with velocity (v), relavistic $\Delta t=R\cdot(1-(v/c)^2)^{0.5}/c$ would be more accurate. If v for the Solar System were 630km·s^{-1} (Jones 2004) relative to the microwave background radiation, using the relavistic Δt in place of $\Delta t=R/c$ would not have significantly altered the simulation's results.

2.4 Expansion exponent

To calculate ε, the local ε (ε_{local}) was first progressed from 1 to infinity using:

$\varepsilon_{local}(R)=10$^$((\ln(R/R_0))^3/(17000+(\ln(R/R_0))^{2.95})$

A content-allocated average of past values of ε_{local} was then calculated using:

$\varepsilon_n=(\varepsilon_{n-1}\cdot\Gamma_{n-1}+\varepsilon_{local})/\Gamma_n$

2.5 Asymptotic q_∞ and Ht_∞

Theory-connected asymptotic q_∞ and Ht_∞ were in sync with GR (figure 2). At radiation-dominated Planck time, $q_\infty=1$ and $Ht_\infty=½$. For matter-dominated expansion, $q_\infty=½$ and $Ht_\infty=⅔$. In the distant future, q_∞ approached 0 and Ht_∞ approached 1 (vacuum-dominated).

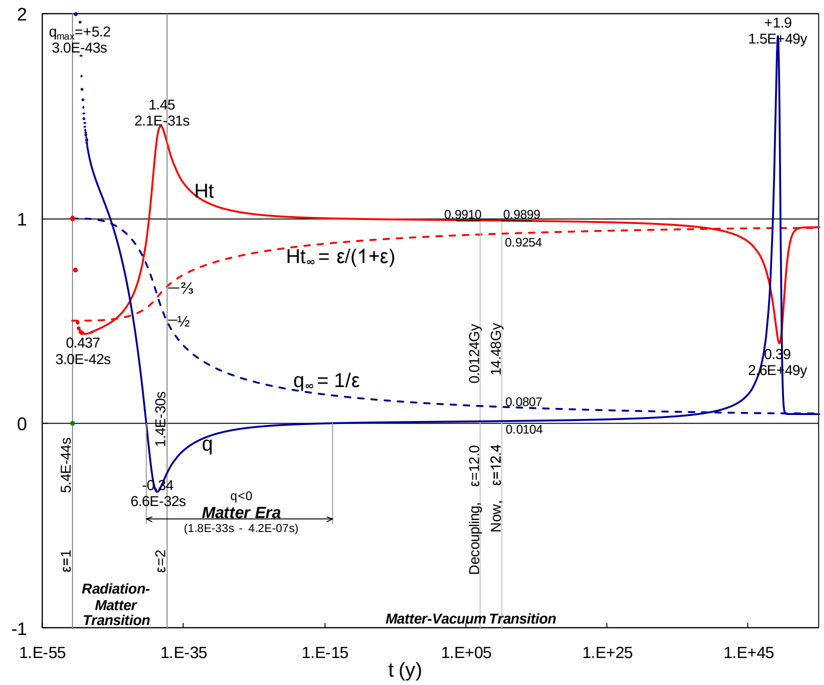

Figure 2. $q(t)$, $Ht(t)$, $q_\infty(t)$, and $Ht_\infty(t)$. Negative q defines the Matter Era. ε=2 delineates the Radiation-Matter Transition and Matter-Vacuum Transition.

2.6 Dynamic q and Ht

Distinct from theory-connected q_∞ and Ht_∞, q and Ht projected a dynamic expansion (figure 2). From the non-zero Planck-scale beginning of time, q cycles from 0 to more than 5 to –0.34 to +1.9 and back to 0, and Ht cycles from 1 to 0.437 to 1.45 to 0.39 and back to 1. In all cases, Ht_{max} lagged q_{min} and Ht_{min} lagged q_{max}. In contrast to past and future expansion, in the current epoch – defined here as the time since Decoupling at redshift z=1090.88 (Hinshaw et al. 2009) – the expansion was effectively 'coasting' with q=~0 and Ht=~1.

2.7 Inflation, the Matter Era, and era transitions

The Matter Era was initially defined as beginning with Ht_∞=0.583 (midway between 1/2 and 2/3) and ending with Ht_∞=0.833 (midway between 2/3 and 1). When a definitive time was found for ε=2 (associated with the Matter Era's Ht_∞=2/3), a line of demarcation between the Radiation-Matter Transition and the Matter-Vacuum Transition was established, and the three eras were abandoned. Later came the finding that when q was negative, Ht_∞ rose from 0.562 to 0.881 – roughly the same values previously used to define the Matter Era. Linking the Matter Era to Inflation, the three eras were reinstated.

2.8 Time of Decoupling

The simulation found the time of Decoupling (t_D) to be 12.4My by setting redshift (z) to zero at t_{now}=14.48Gy and using z_D=1090.88 (Hinshaw et al. 2009) and $z_D+1=R_{now}/R_D$, where z_D and R_D are the redshift and scale factor at Decoupling. 12.4My is in relative agreement with a coasting model's t_D=13My (Gimenez 2009). The current literature typically places t_D=0.377My (Hinshaw et al. 2009), which appears to be based on $z_D+1=(t_{now}/t_D)^{Ht}$, t_{now}=13.72Gy, and Ht=2/3. Hinshaw's $H_{now}=70.5km\cdot s^{-1}\cdot Mpc^{-1}$ (1/13.87Gy) and t_{now}=13.72Gy, however, produce Ht_{now}=0.9892, which is inconsistent with Ht=2/3.

2.9 q-Ht phase diagram

Dynamic q-Ht fluctuations appeared in the q-Ht phase diagram (figure 3) as large lobes that roughly took on the shape of the attractor rail – a line of attractors that q-Ht would gravitate to if ε were constant. Paralleling the finding that Ht_{max} lagged q_{min} and Ht_{min} lagged q_{max}, with the q-Ht trace orbiting clockwise around a moving attractor on the attractor rail, Ht lagged $(1+q)^{-1}$. Four exceptions to the Ht-Lag rule occurred when Lag=0.

Lag was found to be $\beta\cdot t^2\cdot d^2Ht/dt^2$, with Lag_{now} and Lag_D near zero and virtually unchanged (0.000177 versus 0.000165), $t^2\cdot d^2Ht/dt^2$ changed only modestly (0.00042 versus 0.00036), and β_{now}=0.421 and β_D=0.458. As evidenced by the large lobes in the Radiation and Vacuum eras, early-Radiation and late-Vacuum Lag is more dynamic.

2.10 Age of the Universe

The Simon-Verde-Jimenez (SVJ) data points (Simon et al. 2005) were used to establish the age of the Universe (t_{now}). While t_{now}=13.72Gy (Hinshaw et al. 2009) is more widely accepted, t_{now}=14.48Gy is a better fit with the SVJ data points (figure 4). $1/H_{now}$=14.63Gy (from t_{now}=14.48Gy and Ht_{now}=0.9899) is within the literature's range of 13.4Gy (Riess et al. 2005) to 15.7Gy (Sandage et al. 2006). As with calculating t_D, z was calculated here using $z=R_{now}/R-1$.

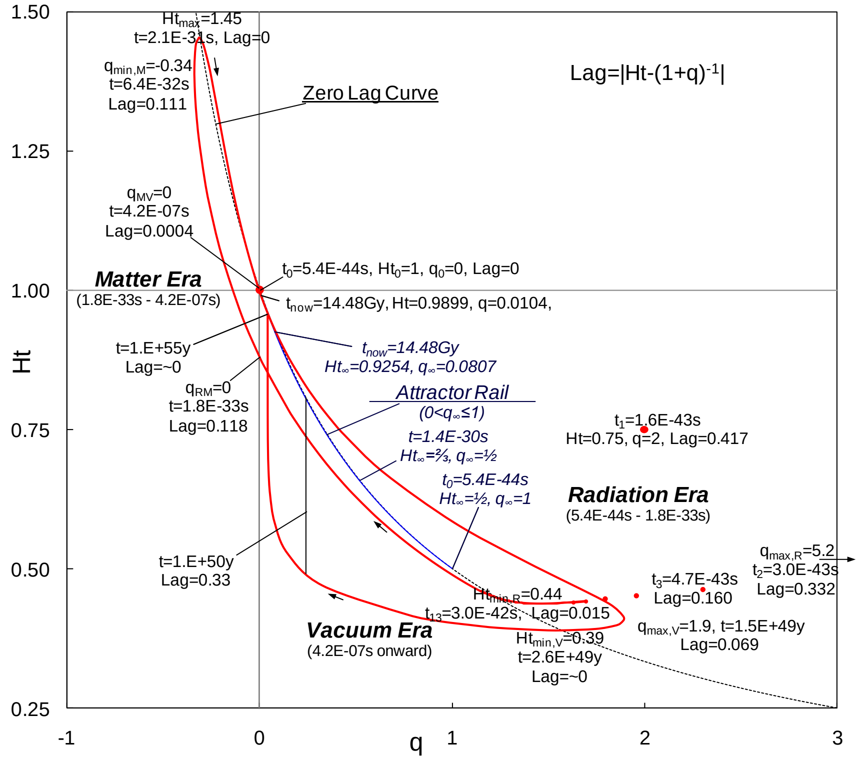

Figure 3. q-Ht phase diagram.

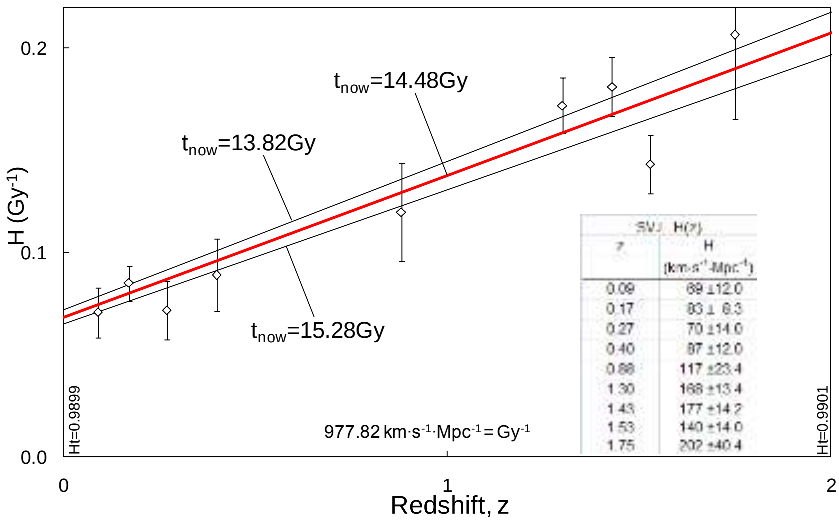

z	H (km·s⁻¹·Mpc⁻¹)
0.09	69 ±12.0
0.17	83 ± 8.3
0.27	70 ±14.0
0.40	87 ±12.0
0.88	117 ±23.4
1.30	168 ±13.4
1.43	177 ±14.2
1.53	140 ±14.0
1.75	202 ±40.4

Figure 4. H(z) for high-z radiogalaxy SVJ data points with σ=1 error bars and curves for t_{now} of 13.82Gy, 14.48Gy, and 15.28Gy.

2.11 Age-Redshift Test

The simulation passes the age-redshift test (figure 5) with a 0.80Gy formation time (t_{form}) for the worst case APM 08279+5255 at z=3.91. For t_{now}=13.7Gy, t_{form}=0.66Gy.

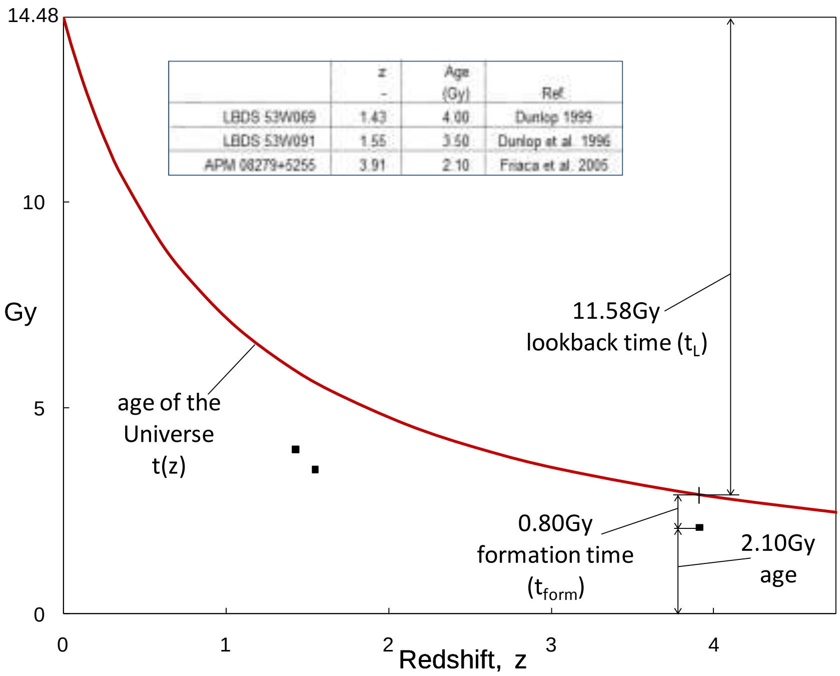

Figure 5. t(z) with age(z) for three old celestial objects.

2.12 t_L, t, t_{now}, z, and H

During work on figure 5, the following relationships were uncovered between time (t), current age of the Universe (t_{now}), Hubble parameter (H), and redshift (z) and between lookback time (t_L), current age of the Universe (t_{now}), and the Hubble parameter (H), time (t), and redshift (z).

$$(t/t_{now})^{Ht} = 1/(1+z)$$

$$(t_L/t_{now})^{Ht} = z/(1+z)$$

A search of the literature has not found anything resembling these two equations.

3 Discussions

3.1 No current acceleration

This effort to numerically simulate cosmic expansion began with the belief that any indication of a current accelerated expansion (q_{now}<0) was in error. The Cosmos was not expanding out of control, and a Big Rip was not forecast. We believed in self-regulating expansion. Not too surprisingly, we found just that.

The results of this simulation indicate that q_{now}=+0.0104. If current evidence of a negative q_{now} were to be confirmed, the results of this simulation would be refuted. It is highly doubtful, however, that q_{now} is negative, since the best estimates for H_{now} and t_{now} place Ht_{now}=0.9892 (Hinshaw et al. 2009). If Lag_{now}=~0 (as indicated by this simulation) and $Ht_{now}=(1+q_{now})^{-1}$, Ht_{now}=0.9892 would force q_{now} positive and a negative q_{now} would force Ht_{now} greater than one. If, instead, Hinshaw's Ht_{now}=0.9892 were coupled with q_{now}=–0.6 (Shapiro et al. 2005) and $Lag=|Ht-(1+q)^{-1}|$, Lag would be greater than 1.5, which would be indicative of an implausibly wild dynamic that was not seen in this simulation (Lag never exceeded 0.011 in the current epoch).

3.2 Refining values for H, t, q, t_{now}, z, and t_L

Errors in observational data – especially evident in deriving distances – have been the bane of astronomy since before the time of Hubble. The SVJ data points (figure 4) demonstrate the significance of the error and how underestimated that error typically is. As seen in section 3.1, with Lag_{now}=~0 in the current epoch (z=0 to z=1091), $Ht=(1+q)^{-1}$ can be used to good approximation to refine values for H, t, and q. Similarly, $(t/t_{now})^{Ht} = 1/(1+z)$ and $(t_L/t_{now})^{Ht} = z/(1+z)$ can be used to refine values for t, t_{now}, H, z, and t_L.

3.3 Unexpected findings

Aside from the above-mentioned bias towards a self-regulated expansion, the findings of this paper did not come from prescient expectations or deliberate attempts to address specific issues. The findings came from the computer-generated output of the simulation, where dynamic q and Ht – distinct from theory-connected q_∞ and Ht_∞ – emerged. From these findings came answers to some significant questions that confront science today.

3.4 Inflation

Perhaps first amongst these questions concern Inflation. During the simulation's initial development, with an unchanging ε, there was no Inflation. Allowing ε to increase with time created a dynamic q that turned negative (Inflation) in the Matter Era. The mechanism for both Inflation and the demise of Inflation was found in an ever-increasing ε. Helping to further explain the dynamics of Inflation, a book-balancing deflationary Ht trough and peak q occur in the Vacuum Era. One clear indicator that Inflation did occur is that Ht_{now}>0.93 – without Inflation, Ht_{now} would be less than Ht_∞ (0.93).

3.5 The inflaton

Particle physics has no place for the inflaton and this simulation has no need for it. Simplicity dictates that the inflaton does not exist.

3.6 Before Planck time

When cosmologists attempt to extrapolate cosmic expansion back to a time before Planck time, they see physics breaking down and singularities developing. Both quantum mechanics (QM) and the results of this simulation would say that there is no time before Planck time. Given our QM-based Ansatz (R_0=Planck length and t_0=Planck time), the simulation's consistency with QM is more input than output.

3.7 Nonfundamental time

This simulation does not treat time as a fundamental parameter. Like the t_0 consistency with QM discussed above, the nonfundamental nature of time is more input than output. The robustness of the simulation's results without a fundamental time, however, attests to the nonfundamental stature of time.

3.8 Entropy and the arrow of time

The low-to-high direction for both entropy and time would imply a connection. $\Delta t=R/c$ says that the tick of the cosmic clock is proportional to R. Given that R and c are both positive, $\Delta t=R/c$ does not allow for the reversibility of time. Entropy, in contrast, while generally having the same unidirectional nature as time, is related to information and thus Γ. The connection between entropy and the arrow of time is thus the connection between Γ and R.

4 Conclusions

Using a content-driven iterative algorithm that had three fundamental parameters and a three-step iterative loop, complexity arose from simplicity. The algorithm generated a forward-progressing, multifaceted representation of cosmic expansion that is self-consistent, concordant with observation, and consistent with SR, QM, and GR.

Dynamic q and Ht emerge, a book-balancing payback for Inflation is found late in the Vacuum Era, a causal mechanism is found for the Big Bang and Inflation, and a discrete and self-regulated expansion is seen. The expansion's discreteness resonates with black-hole thermodynamics, string theory, and spin networks. The expansion's emerging complexity and self-regulation hint at self-organization.

With the model's unmatched simplicity, depth and breadth of findings, and resolution of cosmological issues, the simulation of content-driven expansion supports refinement of the standard model and opens the door for exploring and comparing other cosmic expansion models.

References

1. Gimenez, J.C. 2009, Apeiron Vol. 16, No. 2
2. Harrison, E.R. 2000, Cosmology: The Science of the Universe
3. Hinshaw, G. et al. 2009, ApJ Supplement Series 180, 242
4. Jammer, M. 1953, Historical concepts of space from antiquity to modern science
5. Jones, M.H. et al. 2004, An Introduction to Galaxies and Cosmology, p. 298
6. Perlmutter, S. et al. 1999, ApJ, 517, 565
7. Perlmutter, S., 2003, Supernovae, Dark Energy, and the Accelerating Universe
8. Riess, A.G. et al. 1998, AJ, 116, 1009
9. Riess, A.G. et al. 2005, ApJ, 627, 579
10. Sandage, A. et al. 2006, ApJ, 653, 843
11. Shapiro C.A. et al. 2005, What Do We Know About Cosmic Acceleration?
12. Shu, F.H. 1982, The Physical Universe: An Introduction to Astronomy, University Science Books
13. Simon, J., Verde, L., Jimenez, R. 2005, Physics Review D, 71 123001

Chaotic Modeling and Simulation (CMSIM) 2: 363–369, 2012

Deterministic coherence resonance in systems with on-off intermittency and delayed feedback

J. Buryk, A. Krawiecki, and T. Buchner

Faculty of Physics, Warsaw University of Technology,
Koszykowa 75, PL-00-662 Warsaw, Poland

Abstract. Coherence resonance consists in the increase of regularity of an output signal of a nonlinear device for non-zero intensity of input noise. This phenomenon occurs, e.g., in stochastic systems with delayed feedback in which external noise amplifies the periodic component of the output signal with the period equal to the delay time. In this contribution it is shown that in chaotic systems with delayed feedback deterministic (noise-free) coherence resonance can occur, which consists in the maximization of the periodic component of the output signal in the absence of stochastic noise, due to the changes in the internal chaotic dynamics of the system as the control parameter is varied. This phenomenon is observed in systems with on-off intermittency and attractor bubbling, including generic maps and systems of diffusively coupled chaotic oscillators at the edge of synchronization. The occurrence of deterministic coherence resonance for the optimum value of the control parameter (e.g., of the coupling strength between synchronized oscillators) is characterized by the appearance of a series of maxima at the multiples of the delay time in the probability distribution of the laminar phase lengths, superimposed on the power-law trend typical of on-off intermittency, and by the presence of a strong maximum in the power spectrum density of the output signal.
Keywords: on-off intermittency, coherence resonance, delayed feedback.

1 Introduction

On-off intermittency (OOI) is a sort of extreme bursting which occurs in systems posessing a chaotic attractor within an invariant manifold whose dimension is less than that of the phase space [1,2]. As a control parameter crosses a certain threshold this attractor undergoes a supercritical blowout bifurcation [3] and loses transverse stability, and a new attractor is formed which encompasses that contained within the invariant manifold. Just above the blowout the phase trajectory stays for long times close to the invariant manifold and occasionally departs from it; if the distance from the invariant manifold is an observable, this results in a sequence of laminar phases and bursts. The distribution of laminar phase lengths τ obeys a power scaling law $P(\tau) \propto \tau^{-3/2}$ [1]. In the presence of additive noise chaotic bursting occurs below the blowout

Received: 29 June 2011 / Accepted: 31 March 2012

ISSN 2241-0503

bifurcation threshold; this phenomenon is known as attractor bubbling [2,4]. OOI and attractor bubbling were observed in systems as diverse as model maps with time-dependent control parameter [1], chaotic synchronization [5], spin-wave chaos [6], microscopic models of financial markets [7], etc.

The role of delayed feedback is important in many systems, e.g. optical resonators, chemical reactions and physiology [8] or chaos control [9,10]. In this paper the influence of delayed feedback on OOI is studied using generic one-dimensional maps with a time-dependent control parameter and synchronized oscillators. It is shown that addition of delayed feedback changes the threshold for the blowout bifurcation and can influence the character of the intermittent bursting: For optimum choice of the control parameter a strong periodic component in the time series above the blowout occurs, with the period equal to the delay time. This is an example of coherence resonance (CR) [11-18], a phenomenon related to the well-known stochastic resonance (SR) [19]. CR manifests itself as the peak of regularity of the output signal of certain non-linear stochastic systems for optimum intensity of the input noise and without any external periodic stimulation. In particular, CR was observed in systems with delayed fedback, including bistable [16] and excitable [17] ones and simple threshold crossing detectors [18]. Since in the models under consideration the role of external noise is played by the internal chaotic dynamics within the invariant manifold, the observed phenomenon is deterministic CR [20], a counterpart of the noise-free (deterministic) SR [21].

2 Modeling with a Logistic Map with a time-dependent control parameter and delayed feedback

As a basic model let us consider the logistic map with the time-dependent control parameter and delayed feedback

$$y_{n+1} = (1-K)\, a\zeta_n y_n \,(1-y_n) + K y_{n-k}, \tag{1}$$

where $0 < K < 1$ is the amplitude of the feedback term and $\zeta_n \in (0,1)$ denotes any chaotic process constrained to the unit interval. The map in Eq. (1) has the invariant manifold $y_n = 0$ with the chaotic attractor $(\zeta_n \in (0,1), y_n = 0)$ within it. For $a > a_c$ the variable y_n exhibits intermittent bursts, where a_c is the blowout bifurcation threshold dependent on ζ_n. For $K = 0$ Eq. (1) is the generic model for OOI [1]. The qualitative properties of OOI are independent of the details of the dynamics within the invariant manifold provided that the correlation time of the process ζ_n is negligible in comparison with the mean time between bursts, which is true just above the threshold for the blowout bifurcation; hence, ζ_n can be approximated by white noise ξ_n uniformly distributed on $(0,1)$ [1]. It should be also noted that Eq. (1) with the control parameter constant in time, i.e., with $\zeta_n \equiv 1$, (the logistic map with delayed feedback) can serve as a model for chaos control [10].

For $y_n \approx 0$ the dynamics transverse to the invariant manifold is well approximated by a linearization of Eq. (1),

$$y_{n+1} \approx (1-K)\, a\zeta_n y_n + K y_{n-k}. \tag{2}$$

Introducing new variables in the direction transverse to the invariant manifold, $y_n^{(1)} = y_n$, $y_n^{(2)} = y_{n-k}, \ldots, y_n^{(j)} = y_{n-k+j-2}, \ldots, y_n^{(k+1)} = y_{n-1}$ [10] Eq. (2) can be written as a linear transformation

$$\mathbf{y}_{n+1} = \hat{M}_n \mathbf{y}_n, \tag{3}$$

where $\mathbf{y}_n = \left(y_n^{(1)}, y_n^{(2)}, \ldots, y_n^{(k+1)}\right)^T$ (thus, $\mathbf{y}_n = 0$ is the invariant manifold), and

$$\hat{M}_n = \begin{pmatrix} (1-K)\, a\zeta_n & K & 0 & 0 & \ldots & 0 \\ 0 & 0 & 1 & 0 & \ldots & 0 \\ 0 & 0 & 0 & 1 & \ldots & 0 \\ \vdots & \vdots & \vdots & \vdots & \ddots & \vdots \\ 1 & 0 & 0 & 0 & \ldots & 0 \end{pmatrix}. \tag{4}$$

The transverse stability of the attractor within the invariant manifold is controlled by the transverse Lyapunov exponent λ_T [1-3],

$$\lambda_T = \lim_{N \to \infty} \frac{1}{N} \ln \frac{\left|\left|\hat{M}_{N-1} \ldots \hat{M}_2 \hat{M}_1 \mathbf{y}_0\right|\right|}{||\mathbf{y}_0||}, \tag{5}$$

where $\mathbf{y}_0$ is an arbitray initial vector transverse to the invariant manifold (in simulations, $\mathbf{y}_0$ is assumed as a random vector of unit length). The exponent λ_T increases with a from negative to positive values and crosses zero at the threshold for the blowout bifurcation $a = a_c$, corresponding to the onset of OOI.

The dependence of a_c on K for the map (1) with $\zeta_n = \xi_n$ and various k is shown in Fig. 1(a). The value of a_c weakly depends on k and monotonically decreases to $a_c = 2.0$ for $K \to 1$. Typical time series y_n for a just above a_c is shown in Fig. 1(b). For increasing K the character of the time series changes from intermittent bursts with high amplitude typical of OOI to frequent bursts with small amplitude. There is also a gap between the minimum value of y_n and the invariant manifold $y_n = 0$. Thus the effect of the delayed feedback on the generic model for OOI resembles that of additive noise which prevents the phase trajectory from approaching closely the invariant manifold and lowers the threshold for the occurrence of bursting, leading to attractor bubbling [2,4]. This is not surprising since the additive noise enters Eq. (1) in the same way as the feedback term; moreover, especially for long k, due to decreasing correlation, the feedback term can be treated as a sort of deterministic noise.

For $K > 0$ the distribution of laminar phase lengths $P(\tau)$ for a just above a_c exhibits a series of maxima at the values of τ equal to k and its multiples (Fig. 1(c)) superimposed on a power-law trend typical of OOI. Let us define the output signal as $Z_n = 0$ if y_n is in the laminar phase and $Z_n = 1$ if y_n is in the burst phase (such discretization is typical in the study of systems with SR). Then, a broad peak centered at the frequency $2\pi/k$ appears in the power spectrum density (PSD) of Z_n (Fig. 1(d)). Both absolute and relative (with respect to the mean value of the PSD on the interval $(\pi/k, 3\pi/k)$) height of this peak exhibit maximum as functions of a (Fig. 1(e)); these quantities

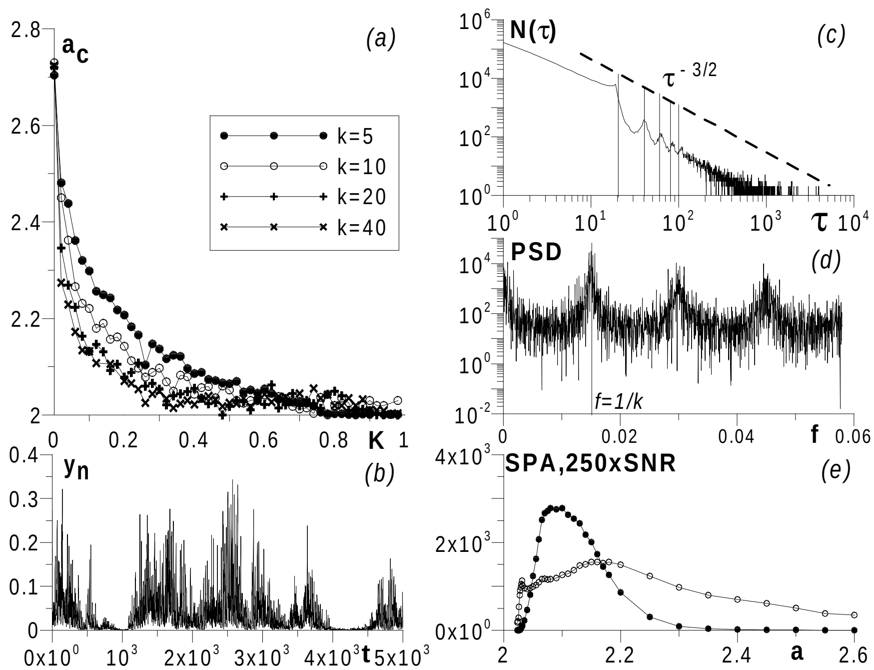

Fig. 1. For the map given by Eq. (1) with $\zeta_n = \xi_n$: (a) intermittency threshold a_c vs. K for various k (see legend); (b) time series $y_n(t)$ for $k = 20$, $K = 0.2$, $a = 2.2$ (just above a_c), the initial condition is $y_0 \in (0, 1)$, where y_0 is a random number, and $y_{-1} = y_{-2} = \ldots y_{-k+1} = 0$; (c) histogram of the number of laminar phases $N(\tau)$ of duration τ for $k = 20$, $K = 0.3$, $a = 2.1$, y_n was assumed to be in the burst phase ($Z_n = 1$) if $y_n > 0.01$, vertical lines are drawn at multiples of k; (d) PSD from the time series Z_n for $k = 64$, $K = 0.3$, $a = 2.1$; (e) SPA (dots) and 250 SNR (circles) vs. a for $k = 64$, $K = 0.3$.

correspond to the spectral power amplification (SPA) and signal-to-noise ratio (SNR) used in the studies of SR, respectively. The height of these maxima increases, their width decreases and their location approaches $a = a_c$ as $K \to 1$ since then the feedback term becomes dominant in Eq. (1) and the signal Z_n is almost periodic for a just above a_c.

These results show that CR occurs in the map (1) as the control parameter is increased above the threshold for the blowout bifurcation. In fact, systems with OOI resemble excitable ones, in particular just above the intermittency threshold when the bursts are short in comparison with the quiescent laminar phases. Thus, CR in the map (1) resembles that observed in excitable systems and threshold-crossing detectors with delayed feedback and external noise [17,18], e.g., the multiple maxima in the histogram of laminar phase lengths in Fig. 1(c) correspond to those found in the histograms of inter-spike intervals in excitable systems with CR [12]. However, CR in the map (1) appears due to changes of the internal dynamics within the invariant manifold as the control parameter is varied rather than under the influence of external noise. Thus, this phenomenon belongs to the class of deterministic CR as in Ref. [20].

3 Modeling with a system of two diffusively coupled chaotic Rössler oscillators

Similar phenomena were observed in a system of two diffusively coupled chaotic Rössler oscillators,

$$\begin{aligned}
\dot{x}_1 &= -\left(y_1 + z_1\right) \\
\dot{y}_1 &= x_1 + a y_1 + k\left(y_2 - y_1\right) + K s(\tau) \\
\dot{z}_1 &= b + z_1\left(x_1 - c\right) \\
\dot{x}_2 &= -\left(y_2 + z_2\right) \\
\dot{y}_2 &= x_2 + a y_2 + k\left(y_1 - y_2\right) - K s(\tau) \\
\dot{z}_2 &= (b + \delta b) + z_2\left(x_2 - c\right),
\end{aligned} \tag{6}$$

where $a = 0.2$, $b = 0.2$, $c = 11$, k is the strength of the diffusive coupling, $s(\tau) = y_2(t-\tau) - y_1(t-\tau) = \Delta y\,(t-\tau)$ provides delayed feedback with delay τ and amplitude K, and small $\delta b \neq 0$ can be added to model the mismatch of parameters in an experimental system. For $K = 0$ and $\delta b = 0$ the oscillators are identically synchronized for $k > k_c \approx 0.12$ and there is a chaotic attractor within the invariant synchronization manifold $x_1 = x_2$, $y_1 = y_2$, $z_1 = z_2$. For $k < k_c$ synchronization is lost (i.e., the invariant manifold loses transverse stability) and $\Delta y(t) = y_2(t) - y_1(t)$ exhibits chaotic bursts typical of OOI; thus, k is the control parameter for the supercritical blowout bifurcation. For $\delta b \neq 0$ bursts occur already for $k > k_c$ due to attractor bubbling. Similarily, the delayed feedback $Ks(\tau)$ with $K > 0$ also forces the trajectory to leave the invariant mainfold, as in Eq. (1), and causes the onset of intermittent bursts for $k > k_c$.

Typical time series $\Delta y(t)$ exhibiting OOI are shown in Fig. 2(a). If, again, the output signal is defined as $Z(t) = 0$ if $\Delta y(t)$ is in the laminar phase and $Z(t) = 1$ if $\Delta y(t)$ is in the burst phase, a broad peak centered at the frequency $2\pi/\tau$ appears in the PSD of $Z(t)$ for a range of k below and just above k_c (Fig. 2(b)). The height of this peak (SPA) exhibits maximum as a function of k, both for $\delta b = 0$ and $\delta b > 0$ (Fig. 2(c)); in the latter case only the range of the control parameter where the bursts are observed is slightly broadened toward higher values. This demonstrates that deterministic CR occurs in the system given by Eq. (6) and the output signal exhibits maximum regularity for optimum value of the parameter k which controls the internal dynamics within the invariant synchronization manifold. The maximum of the SNR vs. k is not clearly visible (Fig. 2(d)): evaluating PSD from much longer time series would probably lead to smoother curves of the SNR. Hence, the results of numerical simulations suggest that deterministic CR can be observed experimantally in systems of coupled chaotic oscillators at the edge of identical synchronization.

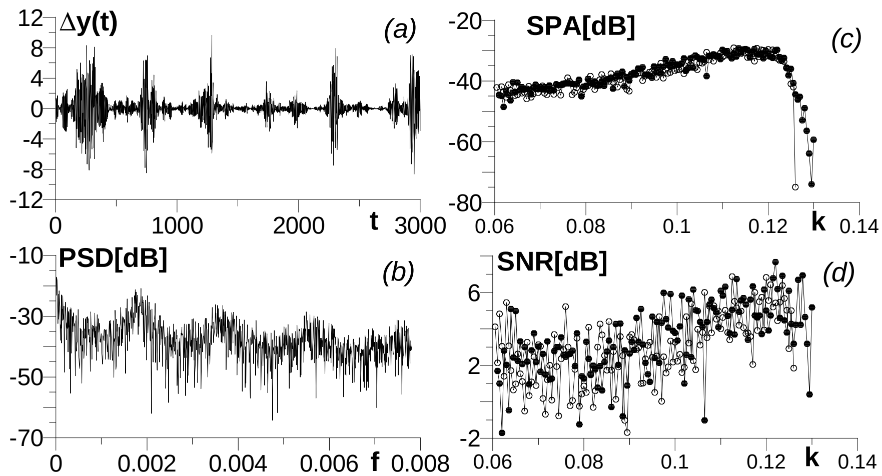

Fig. 2. For the system of diffusively coupled Rössler oscillators given by Eq. (6) with $\tau = 512$, $K = 0.05$, (a) time series $\Delta y(t)$ for $k = 0.12$, $\delta b = 10^{-4}$; (b) PSD from the time series $Z(t)$ for $k = 0.12$, $\delta b = 10^{-4}$, $\Delta y(t)$ was assumed to be in the burst phase ($Z(t) = 1$) if $\Delta y(t) > 0.1$; (c) SPA and (d) SNR vs. k for $\delta b = 0$ (circles) and $\delta b = 10^{-4}$ (dots)

4 Summary

To summarize, the influence of delayed feedback on OOI was studied using generic maps with the time-dependent control parameter and synchronized chaotic oscillators. It was found that delayed feedback can decrease the threshold for the blowout bifurcation. Deterministic CR was observed in systems under consideration, characterized by the appearance of a series of maxima at the multiples of the delay time in the probability distribution of the laminar phase lengths, superimposed on the power-law trend typical of OOI, and by the presence of a strong periodic component in the intermittent time series, with period equal to the delay time. The strength of this component exhibits maximum as the control parameter is varied, due to the changes of the internal dynamics of the system within the invariant manifold.

Acknowledgement

This work was financially supported by special funds of the Faculty of Physics, Warsaw University of Technology, under Grant No. 503 G 1050 0015 000.

References

1. N. Platt, E. A. Spiegel, and C. Tresser, *Phys. Rev. Lett.* 70:279, 1993; J. F. Heagy, N. Platt, and S. M. Hammel, *Phys. Rev. E* 49:1140, 1994; S. C. Venkataramani et al., *Physica D* 96:66, 1996.

2.P. Ashwin, J. Buescu, and I. N. Stewart, *Phys. Lett. A* 193:126, 1994.
3.E. Ott and J. Sommerer, *Phys. Lett. A* 188:39, 1994.
4.N. Platt, S. M. Hammel, and J. F. Heagy, *Phys. Rev. Lett.* 72:3498, 1994; S. C. Venkataramani et al., *Phys. Rev. Lett.* 77:5361, 1996.
5.A. Čenys et al., *Phys. Lett. A* 213:259, 1996.
6.F. Rödelsperger, A. Čenys, and H. Benner, *Phys. Rev. Lett.* 75:2594, 1995; A. Krawiecki and A. Sukiennicki, *Acta Phys. Polonica A* 88:269, 1995.
7.T. Lux and M. Marchesi, *Nature* 297:498, 1999; A. Krawiecki, J. A. Holyst, and D. Helbing, *Phys. Rev. Lett.* 89:158701, 2002.
8.G. Giacomelli et al., *Phys. Rev. Lett.* 73:1099, 1994; I. R. Epstein, *J. Chem. Phys.* 92:1702, 1990; M. C. Mackey and L. Glass, *Science* 197:287, 1977.
9.K. Pyragas, *Phys. Lett. A* 170:421, 1992; H. U. Voss, *Phys. Rev. Lett.* 87:014102, 2001.
10.T. Buchner and J. J. Żebrowski, *Phys. Rev. E* 63:16210, 2001.
11.H. Gang et al., *Phys. Rev. Lett.* 71:807, 1993; W.-J. Rappel and S. H. Strogatz, *Phys. Rev. E* 50:3249, 1994.
12.A. Longtin, *Phys. Rev. E* 55:868, 1997.
13.A. S. Pikovsky and J. Kurths, *Phys. Rev. Lett* 78:775, 1997; J. R. Pradines, G. V. Osipov, and J. J. Collins, *Phys. Rev. E* 60:6407, 1999; G. Giacomelli, M. Giudici, and S. Balle, *Phys. Rev. Lett.* 84:3298, 2000.
14.A. Neiman, P. I. Saparin, and L. Stone, *Phys. Rev. E* 56:270, 1997; I. Z. Kiss et al., *Phys. Rev. E* 67:035201, 2003; O. V. Ushakov et al., *Phys. Rev. Lett.* 95:123903, 2005.
15.C. Palenzuela et al., *Europhys. Lett.* 56:347, 2001.
16.L. S. Tsimring and A. Pikovsky, *Phys. Rev. Lett.* 87:250602, 2001; D. Huber and L. S. Tsimring, *Phys. Rev. Lett* 91:260601, 2003; D. Huber and L. S. Tsimring, *Phys. Rev. E* 71:036150, 2005; K. Panajotov et al., *Phys. Rev. A* 69:011801, 2004; M. Arizaleta Arteaga et al., *Phys. Rev. Lett.* 99:023903, 2007; Y. Jin and H. Hu, *Physica A* 382:423, 2007.
17.G. C. Sethia, J. Kürths, and A. Sen, *Phys. Lett. A* 364:227, 2007.
18.R. Morse and A. Longtin, *Phys. Lett. A* 359:640, 2006.
19.R. Benzi, A. Sutera, and A. Vulpiani, *J. Phys. A* 14:L453, 1981; L. Gammaitoni et al., *Rev. Mod. Phys.* 70:223, 1998; V. S. Anishchenko et al., *Physics — Uspekhi* 42:7, 1999 [*Usp. Fiz. Nauk* 169:7, 1999]; F. Moss, "Stochastic resonance: looking forward", in: J. Walleczek (Ed.), *Self-Organized Biological Dynamics & Nonlinear Control*, page 236, Cambridge, UK, 2000, Cambridge University Press.
20.J. F. Martinez Avila, H. L. D. de S. Cavalcante, and J. R. Rios Leite, *Phys. Rev. Lett.* 93:144101, 2004.
21.V. S. Anishchenko, A. B. Neiman, and M. A. Safanova, *J. Stat. Phys.* 70:183, 1993; V. S. Anishchenko, M. A. Safonova, and L. O. Chua, *Int. J. Bifurcation & Chaos* 4:441, 1994; E. Reibold et al., *Phys. Rev. Lett.* 78:3101, 1997; S. Matyjaśkiewicz et al., *Phys. Rev. E* 63:026215, 2001.
22.Ying-Cheng Lai, *Phys. Rev. E* 53:R4267, 1996.

Chaotic Modeling and Simulation (CMSIM) 2: 371-385, 2012

Studying Non-Linear Phenomena of Tumour Cell Populations under Chemotherapeutic Drug Influence[1]

George I. Lambrou, Apostolos Zaravinos, Maria Adamaki and Spiros Vlahopoulos

1st Department of Pediatrics, University of Athens, Choremeio Research Laboratory, Athens, Greece. e-mail: glamprou@med.uoa.gr

Abstract: Biological systems are characterized by their potential for dynamic adaptation. Such systems, whose properties depend on their initial conditions and response over time, are expected to manifest non-linear behaviour. In a previous work we examined the oscillatory pattern exhibited by leukemic cells under *in vitro* growth conditions, where the system was simulating the dynamics of growth with disease progression. Our question in a previous study evolved around the nature of the dynamics of a cell population that grows, or even struggles to grow, under treatment with chemotherapeutic agents. We mentioned several tools that could become useful in answering that question, as for example the *in vitro* models which provide information over the spatio-temporal nature of such dynamics, but *in vivo* models could prove useful too.

In the present work we have studied the non-linear effects that arise from cell population dynamics during chemotherapy. The study was performed not only in the sense of cell populations *per se* but also as an attempt of identifying sub-populations of cells, such as apoptotic cells and cells distributed within the cell cycle. The temporal transition from one state to the next was revealed to follow non-linear dynamics. We have managed to approximate the non-linear factor that influences these temporal space transitions. Such approaches could become very useful in understanding the nature of cell proliferation and the role that certain chemotherapeutic drugs play in cell growth, with emphasis given on the underlying drug resistance and cell differentiation mechanisms. Further on, we have attempted to approach this problem by using experimental data using the case of glucocorticoids. Glucocorticoids are considered to be indispensable agents in the treatment of hematologic malignancies. A critical established glucocorticoid action is the apoptotic effect that they exert on leukemic cells. However, little is known about the molecular response of malignant cells on glucocorticoid exposure. Even less is known about the cell proliferation dynamics governing leukemic cells under glucocorticoid influence. Dynamic parameters of the cell population state, like growth rate or its time derivative, are largely overlooked in cell population studies. In the present work a quantitative mathematical and modeling approach is endeavored regarding growth and metabolic dynamics. Cell populations and metabolic factors, such

[1] This study is supported in part by Norwegian, Iceland, Lichtenstein & Hellenic Ministry of Finance Grant EL0049.

Received: 14 July 2011 / Accepted 30 March 2012

ISSN 2241-0503

as glucose, lactate and lactate dehydrogenase (LDH) are measured. Growth and metabolic features are assumed to be of nonlinear nature. A model-based prediction of glucocorticoid effects is derived by applying a non-linear fitting approximation to the measured parameters.
To the best of our knowledge there are not many studies dealing with this topic, which makes it even more interesting.

Keywords: Proliferation, oscillations, non-linearity, CCRF-CEM, glucocorticoids.

1 Introduction

Population dynamics have been the subject of study among various groups. It has already been shown that even cells that grow under normal conditions can manifest proliferation dynamics of non-linear nature [1, 2]. In addition, other groups have demonstrated that this non-linear behavior can also exist under the influence of drugs [3], or similarly, under the influence of environmental factors. Any new knowledge on the mechanisms underlying cell proliferation is of major importance, and even the smallest of indications towards a certain direction could enable us to further discover differences in the mechanisms distinguishing between health and disease. This issue is especially important in tumors, the incidence of which is approaching that of an epidemic. In the present study we focused on the dynamics that were revealed through an *in vitro* cell system, and particularly on the dynamics manifested under the influence of a certain type of chemotherapeutic drug, such as glucocorticoids. Glucocorticoids (GC) are among the most important alternatives in the treatment of leukemia. Resistance to glucocorticoids represents a crucial parameter in the prognosis of leukemia [4-6], whereas it has been shown that GC-resistant T-cell leukemia cells manifest a biphasic mechanism of action or imply an inherent resistance mechanism of action to glucocorticoids [7]. New questions arise regarding the nature of the dynamics of a cell population under the influence of a drug. If certain physical measures, such as proliferation, are observed on the phenotypic level, how are they translated on the molecular / genomic level? For example, if a cell population increases its rate of proliferation, does it mean that the genes required for this effect transcribe faster than usual? An interesting report by *Mar et al. (2009*) suggested that gene expression takes place in quanta, i.e. that it happens discretely and not continuously [8, 9]. Also, in two other reports it was suggested that gene expression follows oscillatory patterns, which makes things even more complicated with regards to the proliferation rate, be it growth acceleration or deceleration [10, 11]. This means that cells cannot simply transit from one state to another in terms of growth rate. Should the hypothesis of oscillatory modulation of gene expression, which implies non-linearity, stand correct, then a much more complicated regulatory pattern is required by a cell so as to change its state, as a function of environmental stimuli. The present work provides evidence supporting this view, with respect to glucocorticoids. The answer on whether cells possess inherent mechanisms inducing GC tolerance or whether they develop resistance as a response to treatment remains elusive. In other words, do cells evolve to a certain phenotype or they already possess traits such as drug resistance?

The same applies for critical aspects of the metabolism of cancer cells and in particular, leukemic cells. Already in 1924, *Warburg et al.* observed that a shift occurred in tumors from oxidative phosphorylation to aerobic glycolysis, known as the *Warburg effect* [12]. It is known, that metabolites, or metabolic molecules, do not only participate in metabolic processes related solely with energy production and thermodynamical conservation of the cell, but also mediate numerous signal transduction related functions.

We did not give emphasis on the molecular profile of proliferating cells but rather on cell populations as they are measured during glucocorticoid treatment, in a spatio-temporal manner. Previous works have dealt with this issue, giving emphasis on the glucocorticoid receptor and the pharmacokinetics of glucocorticoids (methylprednisolone) [13, 14].

The present work uses numerical analysis methods along with fitting and modeling approximations in order to establish a mathematical model for the analysis and prediction of the effects of glucocorticoids on T-leukemic cells. Also, we attempted to demonstrate the non-linear nature of the present biological system using experimental data from both proliferation measures and metabolic factor measurements, complementary to the theoretical aspects. We have also, tried to measure and calculate physical constants, such as, growth and consumption rate and its time derivative (the analogues of velocity and acceleration) of the observed processes, if such exist. Overall, the significance of the present work relies on the effort to set up a mathematical framework for the prediction of glucocorticoid effects on leukemic cells and its connection to non-linear phenomena. To the best of our knowledge, there are no previous reports on modeling the effects of glucocorticoids on leukemic systems.

2 Materials and Methods

Cell Culture and Prednisolone Treatments

The CCRF-CEM (ALL) cell line was obtained from the European Collection of Cell Cultures (ECACC) and was used as the model cell line. The T-Lymphoblastic Leukemia CCRF-CEM cells were grown in RPMI-1640 medium supplemented with 2mM L-Glutamine and Streptomycin/Penicillin 100 U/ml (Gibco, Carlsbad, CA), 20% FBS (Gibco, Carlsbad, CA) at 37^{o}C, 5% CO_2 and ~100% humidity. Cells were allowed to grow to ~900-1.500×10^3 cells/ul for CCRF-CEM. The following concentrations of prednisolone (Pharmacia, Boston, MA) were used: 0μM (control), 10nM, 100nM, 1uM, 10μM, 100uM and 700μM [7].

Cell Population Measurements

Cell population counts were determined with the use of a NIHON KOHDEN CellTaq-α hematology analyzer. Cells were counted at the -24 h time point as well as at 0 h, 4 h, 24 h, 48 h, 72 h after having been let to grow under normal conditions. For this purpose, 200 μl of cell suspensions were obtained from each flask and counted directly with the analyzer [7].

Biochemical Measurements

Supernatants from the cell culture were taken every 24h and kept at -80°C thereafter until further processing. In brief, 1ml of cell culture media was centrifuged at 1200 rpm for 10min and the supernatant was removed and kept for further processing. Samples were then measured with a Siemens biochemical analyzer *Advia 1800*. The factors measured were Glucose (mg/dlt), Lactic Acid (mg/dlt), Lactate Dehydrogenase (LDH, IU/lt) and Alkaline Phosphatase (ALP, IU/lt).

Flow Cytometric Measurements

Flow cytometry was performed on a *Beckman Coulter* flow cytometer *FlowCount XL*. Cytotoxicity measurements were performed as previously described [7]. All experiments were performed in triplicate. The reported data constitute the average of three independent experiments.

Data Analysis

Flow cytometry and cell cycle data (cell cycle data not shown) were analyzed with *WinMDI* software version 2.8 (*The Scripps Institute, Flow Cytometry Core Facility*) and *Cylchred* version 1.0.2 (*Cardiff University, Wales)* which is based on the algorithms proposed by Watson et al. and Ormerod et al [15-17]. Raw data from cytometric studies were pre-processed in Microsoft Excel® and further data processing was performed with the Matlab® Computing environment (The Mathworks Inc.).

3 Mathematical Formulations

Generalized Cell Population Dynamics under Drug Influence

In order to establish a modeling approach to the phenomenon described above, we discriminated between different cell populations. That is, if at time t a cell population is considered to be N, then this is a mixture of cells in various stages. More specifically, we have discriminated between the cell cycle phases and cell death. The cell cycle is the path through which cells manifest proliferation. The identification of cells in specific cell cycle phases is of critical importance, since it will determine cellular proliferation, cessation or cell death. Also, in various systems the detection of cells at specific cell cycle points, denotes a mechanism of reaction to an environmental stimulus, as for example in the present case is the glucocorticoid. In Figure 1, we present the model diagrammatically.

The three phases of the cell cycle are represented. $G_{1,t}$, $G_{1,t+1}$, $G_{1,t+n}$ is the number of cells in G_1 phase at time t, $t+1$ and $t+n$ respectively, S_t, S_{t+1}, S_{t+n} is the number of cells in S phase at time t, $t+1$, $t+n$, respectively, $G_{2,t}$ is the number of cells in G_2 phase at time t, $t+1$, $t+n$, respectively and CD_t, CD_{t+1}, CD_{t+n} is the number of dead cells at time t, $t+1$, $t+n$, respectively. The arrows connecting the different cell states, denote the possibilities that a cell has to transit from one state to another. So, for example, a cell in G_1 phase has three possibilities: to remain in the G_1 phase, to transit to the *S* phase or to become apoptotic, such as cell death (*CD*). This means that it is impossible for the cell to go from the G_1 phase to G_2 phase. A very important factor shown in Figure 1, is the $K_{factor,t}$, which denotes the rate of transition from one cell state to another. Hence, the factor *k* will take the following subscripts:

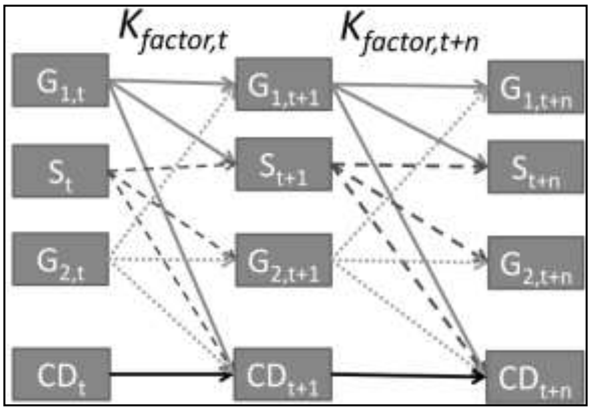

Fig. 1. A schematic representation of the model approach for cell population showing transitions between cell cycle phases and cell death.

$G_{1,t} \rightarrow G_{1,t+1}$: k_1, $G_{1,t} \rightarrow S_{t+1}$: k_2, $G_{1,t} \rightarrow CD_{t+1}$: k_3,
$S_t \rightarrow S_{t+1}$: k_4, $S_t \rightarrow G_{2,t+1}$: k_5, $S_t \rightarrow CD_{t+1}$: k_6
$G_{2,t} \rightarrow G_{2,t+1}$: k_7, $G_{2,t} \rightarrow G_{1,t+1}$: k_8, $G_{2,t} \rightarrow CD_{t+1}$: k_9
$CD_t \rightarrow CD_{t+1}$: k_{10}

The following equations describe the transitions from one state to the next:

$$N_{G_{1,t+1}} = N_{G_{1,t}} \cdot k_1 + N_{G_{2,t}} \cdot k_8$$

$$N_{S_{t+1}} = N_{S_t} \cdot k_4 + N_{G_{1,t}} \cdot k_2$$

$$N_{G_{2,t+1}} = N_{G_{2,t}} \cdot k_7 + N_{S_t} \cdot k_5$$

$$N_{CD_{t+1}} = N_{CD_t} + N_{G_{1,t}} \cdot k_3 + N_{G_{2,t}} \cdot k_9 + N_{S_t} \cdot k_6$$

Where, *N* denotes the respective cell population at time *t*. These equations could be formulated in more generalized form since each population at time *t+1* consists of two other populations at time *t*. Hence, the generalized form would be: $N_{p_x,t+1} = N_{p_y,t} k_y + N_{p_z,t} k_z$

In other words, our model shows that the next state is defined by the previous one. Each cell subpopulation consists of parts of the other subpopulations.

These equations appear to be of linear form and are simple to solve. Yet, the factor k is a non-linear factor, which can be determined only experimentally. It is dependent upon environmental factors *f(environmental)*, such as nutrient availability and space, and in the present case is a function of glucocorticoid concentration $f(C_p)$. We have reported this previously, that cell populations defined experimentally, could be described with Fourier series, with respect to the transition factor k [12].

The generalized form of the series we have used for our approach was given by:

$$f(x,y) = a_0 + a_1\cos(xy) + a_2\sin(xy)$$

Hence, the factor k for each transition, meaning from one cell state to the next would be given by the following system of equations:

$$k_1 = a_{0,1} + a_{1,1}\cos(N_{G_{1,t}} \cdot N_{G_{1,t+1}}) + a_{2,1}\sin(N_{G_{1,t}} \cdot N_{G_{1,t+1}})$$

$$k_2 = a_{0,2} + a_{1,2}\cos(N_{G_{1,t}} \cdot N_{S_{t+1}}) + a_{2,2}\sin(N_{G_{1,t}} \cdot N_{S_{t+1}})$$

$$k_3 = a_{0,3} + a_{1,3}\cos(N_{G_{1,t}} \cdot N_{CD_{t+1}}) + a_{2,3}\sin(N_{G_{1,t}} \cdot N_{CD_{t+1}})$$

$$k_4 = a_{0,4} + a_{1,4}\cos(N_{S_t} \cdot N_{S_{t+1}}) + a_{2,4}\sin(N_{S_t} \cdot N_{S_{t+1}})$$

$$k_5 = a_{0,5} + a_{1,5}\cos(N_{S_t} \cdot N_{G_{2,t+1}}) + a_{2,5}\sin(N_{S_t} \cdot N_{G_{2,t+1}})$$

$$k_6 = a_{0,6} + a_{1,6}\cos(N_{S_t} \cdot N_{CD_{t+1}}) + a_{2,6}\sin(N_{S_t} \cdot N_{CD_{t+1}})$$

$$k_7 = a_{0,7} + a_{1,7}\cos(N_{G_{2,t}} \cdot N_{G_{2,t+1}}) + a_{2,7}\sin(N_{G_{2,t}} \cdot N_{G_{2,t+1}})$$

$$k_8 = a_{0,8} + a_{1,8}\cos(N_{G_{2,t}} \cdot N_{G_{1,t+1}}) + a_{2,8}\sin(N_{G_{2,t}} \cdot N_{G_{1,t+1}})$$

$$k_9 = a_{0,9} + a_{1,9}\cos(N_{G_{2,t}} \cdot N_{CD_{t+1}}) + a_{2,6}\sin(N_{G_{2,t}} \cdot N_{CD_{t+1}})$$

$$k_{10} = 1$$

We could write this system of equations in a more generalized form, which would be:

$$k = a_0 + a_1\cos(N_{p_{y,z},t} N_{p_x,t+1}) + a_2\sin(N_{p_{y,z},t} N_{p_x,t+1})$$, [**Eq. 1**]

Where k is the transition factor, $a_{0,1,2}$ are constants, $N_{p1,t}$ and $N_{p2,t+1}$ are the populations implicated in the transition at time t and $t+1$ respectively.

Substituting the equation describing the generalized k with the equation of the generalized $N_{p,t+1}$ we obtain:

$$N_{p_{x,t+1}} = N_{p_{y,t}}\left[a_0 + a_1\cos\left(N_{p_{y,t}} N_{p_{x,t+1}}\right) + a_2\sin\left(N_{p_{y,t}} N_{p_{x,t+1}}\right)\right] + N_{p_{y,t}}\left[a_0 + a_1\cos\left(N_{p_{z,t}} N_{p_{x,t+1}}\right) + a_2\sin\left(N_{p_{z,t}} N_{p_{x,t+1}}\right)\right]$$, [**Eq. 2**]

This equation describes the transition of a cell population from one state to the next but it cannot be solved analytically. Solutions can only be found numerically, since future populations (N_x) depend on the previous ones and on the fraction of other future cell populations ($N_{y,z}$).

TABLE I
SYMBOLS AND UNITS FOR VARIABLES

Symbol	Quantity	Units
N_t	Total cell population at time *t*	cells/ul $\cdot 10^3$
N_e	Cell population under an effect, *e* can take the following values: *v: viable* *n: necrotic* *a: apoptotic* *ea: early apoptotic* *ta: total apoptotic* *td: total cell death*	cells/ul $\cdot 10^3$
N_{G1}	Cell population in G_1 phase of the cell cycle	cells/ul $\cdot 10^3$
N_S	Cell population in S phase of the cell cycle	cells/ul $\cdot 10^3$
N_{G2}	Cell population in G_2 phase of the cell cycle	cells/ul $\cdot 10^3$
k	The factor by which total population proliferates from time *t* to time *t+1*.	
$K_{e,t}$	The factor by which cell population under a certain effect proliferates from time *t* to time *t+1*. *e* takes values as mentioned above in the same table	
C_G	Glucose concentration	mg/dlt
C_{LA}	Lactic Acid concentration	mg/dlt
C_{ALP}	Alkaline Phosphatase concentration	IU/lt
C_{LDH}	Lactate Dehydrogenase	IU/lt
k_m	The factor by which metabolic factors are produced or consumed. from time *t* to time *t+1*. *m* can take the following values: *G: Glucose* *LA: Lactic Acid* *ALP: Alkaline Phosphatase* *LDH: Lactate Dehydrogenase*	
u_m	Reaction rate (reaction kinetics)	M/sec

Metabolism Dynamics under Drug Influence

Besides the generalized population model, we also attempted to model the glucocorticoid effects, as far as metabolic factors are concerned. A mathematical model was set that enabled numerical solutions for the study of their effects. As described previously in the previous section, the model presumes that the fraction of cells linked to a certain phenotypic effect can be derived from the previous total cell population so, let $N_{e,t+1}$ be the cell population under a certain effect. This effect can be, for the present analysis, either viability or cell death. Therefore, the total population estimate under the impact of a given effect will be given by:

$N_{e,(t+1)} = k_{e,t} \cdot N_{e,t}$, (1) where $k_{e,t}$ is a generalized nonlinear coefficient of the effect e in the population $N_{e,t}$ at this instance.

At the same time, apart from cell proliferation, we have to account for metabolic factors that change over time and probably influence the course of proliferation. In the case of metabolic factors, the rate of change in concentration is defined as the rate of the respective reaction which is:

$u_m = \frac{dC_m}{dt}$ [**Eq. 3**]. However, in the present case two of the substances measured are glucose and lactic acid. It is known that glucose is transformed into two lactic acid molecules based on the reaction: $C_6H_{12}O_6 \rightarrow 2CH_3CHOHCOOH$. This is due to the formation of two molecules of pyruvate from the anaerobic catabolism of glucose and the subsequent formation of two molecules of lactate in the cytosol. However, this reaction represents a lump reaction, namely one that represents the algebraic sum of many reactions. With many intermediates in between and therefore kinetic rules such as *Michaelis-Menten* or *Le Chatelier's/Van't Hoff* cannot be directly applied to these data. However, under the assumption that there is not significant biochemical cross-talk of these intermediates with other external metabolic pools, the lumping of the reactions to a single one, is plausible as is the case of lactate production through the catalysis of pyruvate. The substrates of this reaction were measured. LDH concentration can be accounted only from cells that were lysed and not from the total population. Although the LDH concentration can be numerically calculated, it would still not be a reliable numerical approximation. Therefore, we used the same principle as in the case of cell population. The concentration *C* of a metabolite or substance at time *t+1* can be written as:

$C_{m,(t+1)} = k_{m,t} \cdot C_{m,t}$, [**Eq. 4**]. Applying mass balance equations [18] for the metabolic pools with respect to time we have, $\frac{dC_m}{dt} = k_{m,t} \cdot C_{m,t}$ where $k_{m,t}$ is a generalized coefficient of the net effect observed in the pool $C_{m,t}$ at time *t*. This resembles a modification of the *Lotka-Voltera-Kolmogorov* equations which were initially used for the description of reaction dynamics and further expanded to population dynamics [19, 20]. The *Lotka-Voltera* functions were derived from the *Verhulst* logistic equation [21]. Though succinct this mathematical formulation introduces through the use of factor $k_{m,t}$, non-linearity. Coefficient $k_{m,t}$ bears a critical biological significance in the model. Presuming that the effects in this study are directly linked to glucocorticoid exposure, $k=f(C_p)$, where *p* stands for *prednisolone*, the glucocorticoid used in the present study, the effects observed depend solely on the drug's concentration. In order to approximate the values, i.e. numerically solve our functions, we have used phase-space maps of the measured data. Symbols and definitions are given in Table I.

4 Results

The major challenge of computational and systems biology is to make contributions to the description of population and reaction dynamics [22]. This is applied to both systems under no external influences but also to systems under the influence of external stimuli, such as pharmacological interventions (as in the present case) or environmental stresses. In the case of the cell system studied in the present work, the most interesting observation was that the system was resistant to GCs and therefore our attempt was in fact to model dynamics of cellular growth and metabolism in resistant cases. Future research directions could point towards describing drug effects as a function of time or concentration and towards predicting the outcome of certain treatments or even towards improving the state of treatment in such a way, that it would be more effective. We suggest that the transition of the cell system that we have studied from one state to the next, follows complicated dynamics, manifesting in almost all cases oscillatory behaviour. The use of mathematical and modelling tools for the discovery of such mechanisms is a unique method for understanding complicated biological systems. Many research efforts are dedicated to the improvement of the existing or to the development of new pharmaceuticals. In Figure 2, experimental measurements are presented as an effort to calculate the rate of population change for the total population and data were fitted with Fourier series.

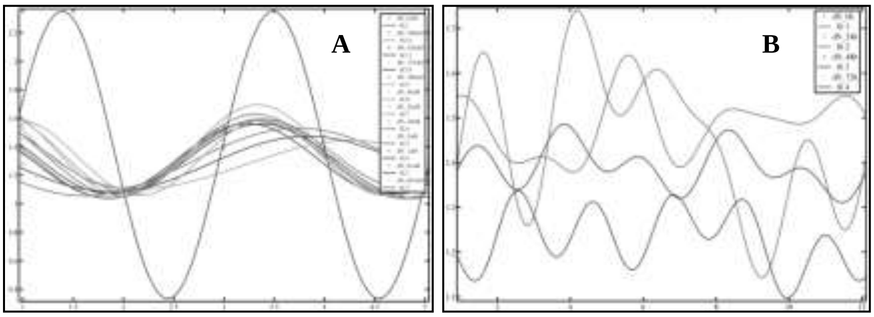

Fig. 2. Simulating the factor k in relation to time (**A**) and glucocorticoid concentration (**B**) showed that both could be fitted with Fourier series. In (**A**) the x-axis corresponds to experimental values from time point measurements of cell numbers, while each curve corresponds to the respective k factor of each glucocorticoid concentration. Similarly, in (**B**) the x-axis corresponds to the glucocorticoid concentrations and each curve corresponds to the time points measured.

Modelling approaches could assist in such efforts as they would provide with a more in-depth understanding of biological systems. The general idea is to be able to predict the future states of a system, based on the present ones. This is proved to be a difficult task, since biological systems follow nonlinear behaviour and, unlike physical systems, there are only a few generalizations that can be formulated. In Figure 3, we have performed numerical approximations of the function (Eq. 2) in order to represent this schematically. The function appeared to give interesting dynamics, as it manifested a saddle point. Also, these phenomena were time dependent, as clearly seen on the experimental level. Thus, by differentiating with respect to time we could obtain a possible role of the temporal factor in this system. Similarly, we have made numerical approximations in order to design the dynamics of the first derivative for both variables, that is $N_{p,y}$ and $N_{p,z}$. The result is presented in Figure 4.

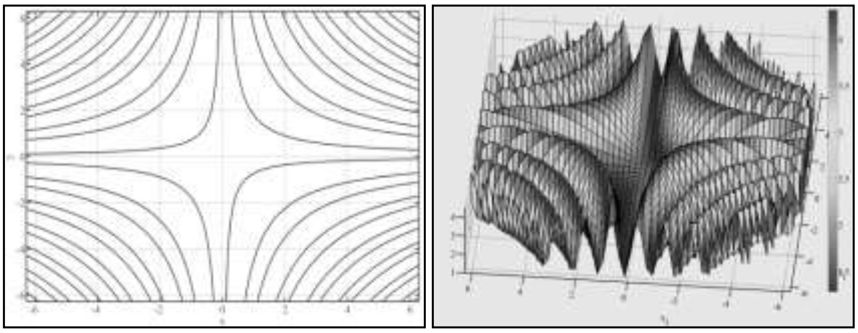

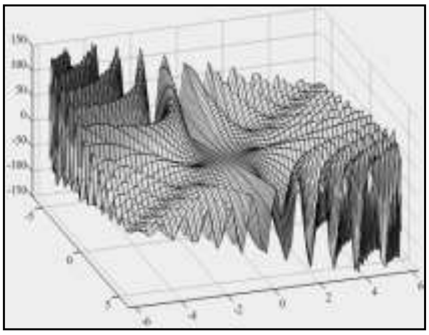

Fig. 3. Using a numerical approximation of the function describing the population transitions manifested interesting dynamics as they formed a saddle.

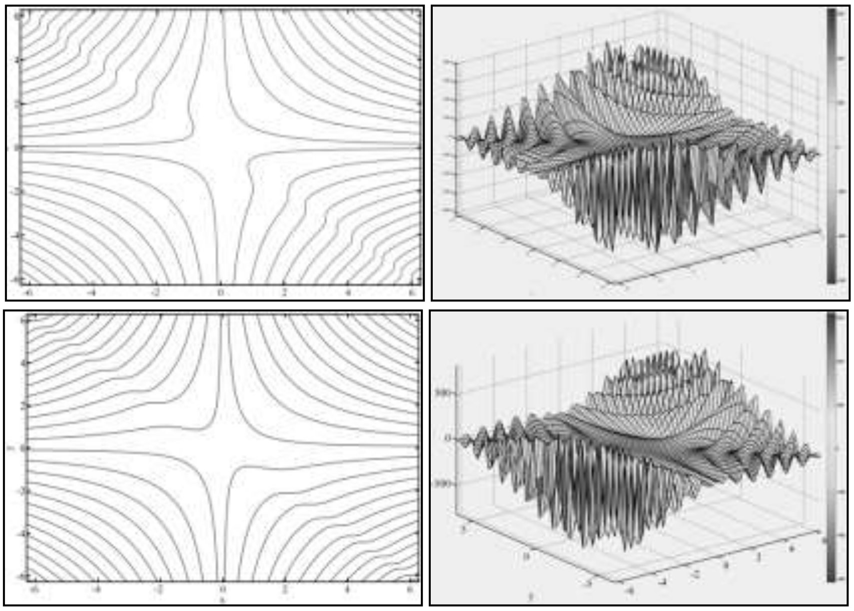

Fig. 4. Numerical representation of the first partial derivative with respect to $N_{p,y}$ (upper left and right) and with respect to $N_{p,z}$ (lower left and right).

Accordingly, as far as metabolic data are concerned, the determination of the factor *k* was implemented with numerical approximations. We have assumed again that *k* is a nonlinear factor. The first aim was to determine the dynamics of the factor *k* i.e. how it changes as a function of concentration. In order to do this, we used the simplified model presented in Figure 5. Glucose measurements were taken from cell culture supernatants (C_G). We assumed that glucose entering the cell was transformed as a total into ATPs and pyruvate. Since cells presumably follow a lactic acid fermentation cycle, pyruvate should be transformed into lactate through LDH.

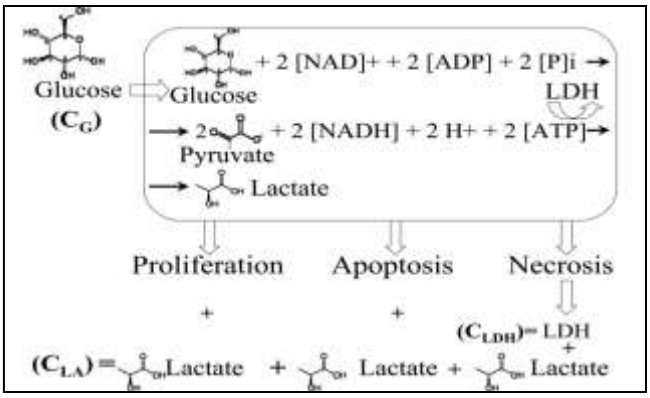

Fig. 5. A simple model of cell fate and measurements of metabolic factors.

In addition, the enzyme LDH (Lactate Dehydrogenase) was measured as a function of the total population of necrotic cells (C_{LDH}). It is important to note that LDH is released from the cells only if cell lysis takes place, thus allowing the contents of the cytosol to be released in the extracellular medium.

At the same time the measured lactate (C_{LA}) was considered to be diffused from both living and apoptotic cells and also released from necrotic cells due to cell membrane lysis. Finally, we accounted for three possible cell fates: progression of proliferation (N_v), necrosis (N_n) and apoptosis (N_{ta}). One of the first correlations calculated was that of the measured LDH and the respective number of necrotic cells. We would be expected to observe a positive correlation between the two factors. We have previously reported that LDH concentration and necrotic cell population indeed showed a positive correlation in two particular cases: untreated cells and cells treated with a large dose of prednisolone (700uM) [23]. This effect can be interpreted as follows: all other glucocorticoid concentrations beside necrotic cell death, also lead to the rupture of the cell membrane and cell lysis. Interestingly, the largest concentration that would be expected to have a lytic effect due to the overdose *per se*, showed a negative correlation, exactly matching that of cells with no glucocorticoid treatment. As mentioned earlier, we have attempted to impute numerically the factor *k* by plotting conditions at time *t+1* vs. conditions at time *t*. In other words we have attempted to model the total cell population over time as a function of the drugs concentrations. As it is shown in Figure 6 it appeared that cells followed complicated dynamics under the influence of the glucocorticoids even when the cell populations are separated into viable, necrotic and apoptotic. The manifested oscillatory behaviour indicates that cells proliferate with nonlinear dynamics, and despite the very few data points, their behaviour could still be revealed. In addition, the plotting of the phase-space of metabolic factors shows that the transition from one state to the other also follows oscillations (Figure 7).

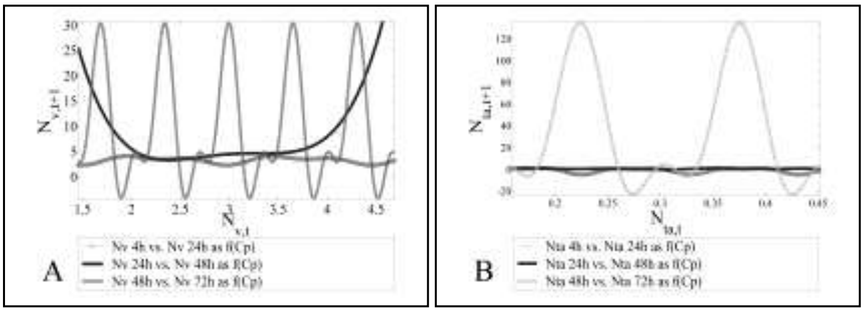

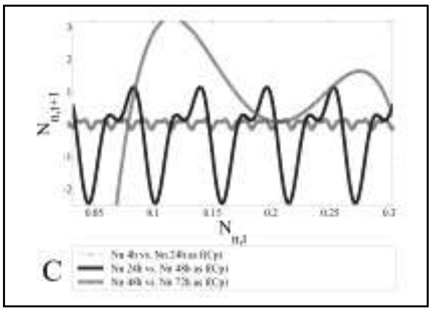

Fig. 6. Phase-space analysis of the different populations manifested complex dynamics with respect to time. In particular, viable cells (**A**), apoptotic cells (**B**) and necrotic cells (**C**) manifested oscillatory behavior as far as the *k* factor is concerned as modelled with Fourier series.

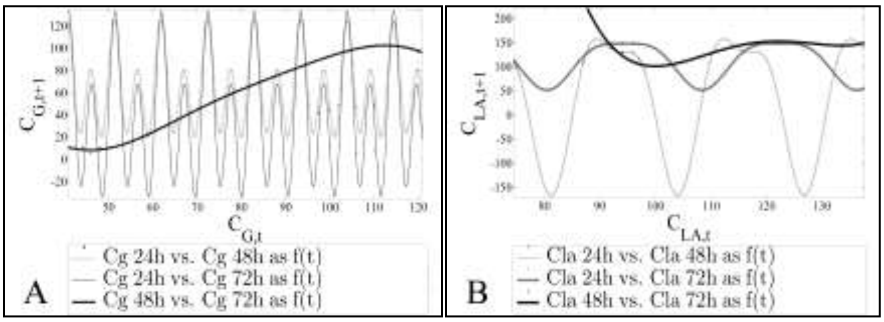

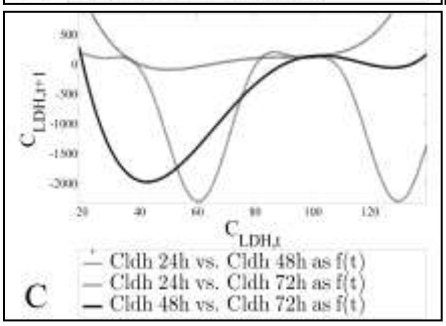

Fig. 7. Fitting of glucose concentration $C_{G,t}$ vs. $C_{G,t+1}$ (**A**), lactate $C_{LA,t}$ vs. $C_{LA,t+1}$ (**B**) and $C_{LDH,t}$ vs. $C_{LDH,\ t+1}$ (**C**). The factor *k* manifested again complicated dynamics resembling oscillatory behavior.

In the present work we attempted to identify non-linear factors of cell proliferation under the influence of chemotherapeutics, and more specifically under the influence of the glucocorticoid prednisolone. We attempted to establish an initial theoretical framework for the analysis of such phenomena and for future considerations. Cell growth appeared to be of a non-linear character. This knowledge could be proved useful in the treatment of tumors, since understanding the biology of proliferation would lead us to a better understanding of cellular resistance to chemotherapeutics. Biological systems are extremely complicated and they manifest, without doubt, non-linear/chaotic phenomena. Therefore, as we have mentioned in previous works, we believe that the maturity of biological sciences would come through integration with other disciplines, such as mathematics and physics, and the ability to give generalized models for these phenomena. Such an example is the understanding of cell proliferation in which we attempted to contribute with hints.

We also attempted to create a modelling framework, along with its mathematical formulation, for describing the dynamics of leukemic cells under the influence of glucocorticoids. We used two factors in our analysis: cell populations, including changes in viability and cell death, and metabolic factors. Approximations of experimental data of course require large datasets, in order to have a more precise view of the fitted phenomena. However, we must mention that obtaining large amounts of data from biological systems can sometimes be proved to be a tedious task. This is owed to the fact that cells in culture preserve a proliferation potential and if they remain in culture for a long period of time, the observed results should be accounted for additional effects besides the one under investigation. In the present analysis, the *Jacobian* matrix J determines the transition dynamics of the system from one state to the next. In a previous work the use of Jacobian matrices was used for the determination of the possible dynamics of a system at a metabolic state [22]. There is a great amount of mathematical formulations concerning biological systems dating back in the early 19th century but the whole idea of integrating biological systems with analytical or stochastic formulations is still in its infancy [13, 19-21]. Therefore, such approaches could prove very useful in gaining more insight into the proliferation dynamics of cell populations and the dynamics emerging under the influence of external stimuli such as chemotherapeutics.

APPENDIX

The functions that have been used for the fitting of the data and the mathematical formulations were the following: Quadratic:

a) $y = ax^2 + bx + c$

b) Cubic: $y = ax^3 + bx^2 + cx + d$

c) polynomial of n^{th} *,* m^{th} *degree:*

$f(x,y) = a_n x^n b_m y^m + a_{n-1} x^{n-1} b_{m-1} y^{m-1} + ... + a_1 x b_1 y + a_0 b_0$ *d) d)* 1^{st} *order Fourier Series:* $a_1 \cos(xw) + b_1 \sin(xw) + a_0$

e) 2^{nd} *order Fourier Series:*

$a_2 \cos(2xw) + a_1 \cos(xw) + b_2 \sin(2xw) + b_1 \sin(xw) + a_0$ *ff) Lotka-Voltera equations:*

$$\frac{dx}{dt} = x(\alpha - \beta y)$$

$$\frac{dy}{dt} = -y(\gamma - \delta x)$$

g) Kolmogorov variation of Lotka-Voltera functions

$$\frac{dx}{dt} = f(x,y)x$$

$$\frac{dy}{dt} = g(x,y)y$$

$$f(x,y) = A_0 - A_1 x - A_2 y$$

$$g(x,y) = B_0 - B_1 x - B_2 y$$

References

[1] C. Wolfrom, N. P. Chau, J. Maigne, J. C. Lambert, B. Ducot, S. Guerroui, and J. Deschatrette, *J Cell Sci,* vol. 113 (Pt 6), pp. 1069-74, Mar (2000).

[2] M. Laurent, J. Deschatrette, and C. M. Wolfrom, *PLoS One,* vol. 5, p. e9346.

[3] S. Guerroui, J. Deschatrette, and C. Wolfrom, *Pathol Biol (Paris),* vol. 53, pp. 290-4, Jun (2005).

[4] M. L. Den Boer, D. O. Harms, R. Pieters, K. M. Kazemier, U. Gobel, D. Korholz, U. Graubner, R. J. Haas, N. Jorch, H. J. Spaar, G. J. Kaspers, W. A. Kamps, A. Van der Does-Van den Berg, E. R. Van Wering, A. J. Veerman, and G. E. Janka-Schaub, *J Clin Oncol,* vol. 21, pp. 3262-8, Sep 1 (2003).

[5] M. Lauten, M. Stanulla, M. Zimmermann, K. Welte, H. Riehm, and M. Schrappe, *Klin Padiatr,* vol. 213, pp. 169-74, Jul-Aug (2001).

[6] G. Cario, A. Fetz, C. Bretscher, A. Moricke, A. Schrauder, M. Stanulla, and M. Schrappe, *Ann Hematol,* vol. 87, pp. 709-16, Sep (2008).

[7] G. I. Lambrou, S. Vlahopoulos, C. Papathanasiou, M. Papanikolaou, M. Karpusas, E. Zoumakis, and F. Tzortzatou-Stathopoulou, *Leuk Res,* May 16 (2009).

[8] J. C. Mar and J. Quackenbush, *PLoS Comput Biol,* vol. 5, p. e1000626, Dec (2009).

[9] J. C. Mar, R. Rubio, and J. Quackenbush, *Genome Biol,* vol. 7, p. R119, (2006).

[10] J. R. Chabot, J. M. Pedraza, P. Luitel, and A. van Oudenaarden, *Nature,* vol. 450, pp. 1249-52, Dec 20 (2007).

[11] T. Degenhardt, K. N. Rybakova, A. Tomaszewska, M. J. Mone, H. V. Westerhoff, F. J. Bruggeman, and C. Carlberg, *Cell,* vol. 138, pp. 489-501, Aug 7 (2009).

[12] O. Warburg, K. Posener, and E. Negelein, *Biochemische Zeitschrift,* vol. 152, pp. 319-344, (1924).

[13] R. Ramakrishnan, D. C. DuBois, R. R. Almon, N. A. Pyszczynski, and W. J. Jusko, *J Pharmacokinet Pharmacodyn,* vol. 29, pp. 1-24, Feb (2002).

[14] Y. N. Sun, D. C. DuBois, R. R. Almon, and W. J. Jusko, *J Pharmacokinet Biopharm,* vol. 26, pp. 289-317, Jun (1998).

[15] M. G. Ormerod and A. W. Payne, *Cytometry,* vol. 8, pp. 240-3, Mar (1987).

[16] M. G. Ormerod, A. W. Payne, and J. V. Watson, *Cytometry,* vol. 8, pp. 637-41, Nov (1987).

[17] J. V. Watson, S. H. Chambers, and P. J. Smith, *Cytometry,* vol. 8, pp. 1-8, Jan (1987).

[18] A. Chatziioannou, G. Palaiologos, and F. N. Kolisis, *Metab Eng,* vol. 5, pp. 201-10, Jul (2003).

[19] A. J. Lotka, *Proc Natl Acad Sci U S A,* vol. 6, pp. 410-5, Jul (1920).

[20] A. J. Lotka, *The Journal of Physical Chemistry,* vol. 14, pp. 271-274, (1910).

[21] P. H. Verhulst, *Corresp. mathématique et physique* vol. 10, pp. 113-121, (1838).

[22] S. Grimbs, J. Selbig, S. Bulik, H. G. Holzhutter, and R. Steuer, *Mol Syst Biol,* vol. 3, p. 146, (2007).

[23] G. I. Lambrou, A. Chatziioannou, M. Adamaki, M. Moschovi, E. Koultouki, T. Karakonstantakis, G. P. Chrousos, and S. Vlahopoulos, "Studying the Nonlinearities of T-cell Leukemia Growth and the Underlying Metabolism Upon Glucocorticoid Treatment through the Application of Dynamic Mathematical Methodologies " in *ITAB 2010,* Corfu, Greece, 2010.

Chaotic Modeling and Simulation (CMSIM) 2: 387-394, 2012

pH Oscillations in the Bromate-Sulfite-Perchloric Acid Reaction

Farah Zaknoun, Mazen Al-Ghoul and Rabih Sultan[1]

[1] Department of Chemistry, American University of Beirut, Beirut, Lebanon
E-mail: rsultan@aub.edu.lb

Abstract: The dynamics of oscillations in chemical reactions has stimulated a wide research interest and produced thousands of studies on about 70 known chemical oscillators, notably over the past 50 years. Oscillating chemical reactions find many applications in Physics, Biology, Geology, Physiology and Medicine.
The dynamics of the bromate-sulfite-perchloric acid (BSH) reaction is investigated in a continuous-flow stirred tank reactor (CSTR), with Mn^{2+} as a proton-consuming (or negative feedback) species. This reaction is known to exhibit periodic oscillations in $[H^+]$, and it thus belongs to a sub-category of chemical oscillators, called pH oscillators.
The reaction is carried out at 45°C, and a flow rate of 1.59 mL/min. The oscillations are monitored in the $[Mn^{2+}]$-$[BrO_3^-]$ phase space, wherein a bifurcation diagram is constructed to delineate the regions of the various behavior regimes. Under our prevailing conditions, a shorter period and higher amplitude of oscillation than those reported in the Literature were obtained. A decrease in the period of oscillations from 40 minutes to 10 minutes in our system under newly imposed $[BrO_3^-]_0$ conditions renders the system more feasible and practical for study. A variation in the flow rate and residence time was also conducted. Decreasing the flow rate from 1.59 mL/min to 1.35 mL/min caused a doubling of the period of oscillations. Yet, over the entire spanned range, no chaotic behavior was observed.
Keywords: Chemical oscillations, BSH reaction, Period doubling, Chaos monitoring, pH oscillations
.

1 Introduction

Oscillating reactions [1] have garnished the chemical literature with rich dynamical behavior encompassing temporal concentration oscillations, and notably fascinating visual spatio-temporal structures. A large number of oscillating reactions is known nowadays, such as the Bray-Liebhafsky (H_2O_2-IO_3^- system) [2], Briggs-Rauscher [3], CIMA (chlorite-iodide-malonic acid) [4] and the Belousov-Zhabotinskii (BZ) [5-7] reactions. Of particular interest to us here, is a subclass of oscillating reactions where the oscillating species is the hydrogen ion (H^+), thus known as pH oscillators [8-10]. The first pH-regulated oscillator was reported by M. Orban, and I. Epstein [11], in the reaction of sulfide ion with hydrogen peroxide. The latter was shown to yield both periodic

Received: 26 June 2011 / Accepted 30 March 2012

ISSN 2241-0503

oscillations and bi-stability in the H^+ potential/pH, in addition to the bi-stability and periodic oscillations in the potentials of Pt redox and sulfide ion-selective electrodes. Afterwards, the field of pH oscillations started growing rapidly spanning reactions with sulfur- or nitrogen- containing species or the ferrocyanide ion as reductants, and basically IO_3^-, IO_4^-, BrO_3^-, and H_2O_2 as oxidants. In constructing a pH-oscillator, the reductant is normally a species that is able to be oxidized to another species that produces H^+, often autocatalytically, or to another species that consumes H^+ by some oxidant. Furthermore, the proper combination of two reductants in a pH-oscillator is often a necessity to control high– or low– pH states. Several pH-oscillators have been characterized mechanistically [12-14]. The most systematically studied pH-oscillators include the reaction of iodate with sulfite and ferrocyanide [10,12], and its bromate [14] analogue. Essentially, designing a pH oscillator is based on having two main composite pathways, the positive feedback pathway that produces H^+, and a negative feedback pathway that removes H^+ from the system.

In this paper we study the bromate-sulfite-perchloric acid (BSH) reaction in a CSTR, and monitor oscillations while varying two main concentration parameters: $[BrO_3^-]_0$ and $[Mn^{2+}]_0$ (one at a time), maintaining all other parameters constant, and then construct the corresponding bifurcation diagrams. The overall reaction in acidic medium is as follows:

$$BrO_3^- + 3\,HSO_3^- \longrightarrow 3\,SO_4^{2-} + Br^- + 3\,H^+ \quad (1)$$

The waveform of the temporal pH oscillations for various values of $[BrO_3^-]_0$ at fixed $[Mn^{2+}]_0$, $[SO_3^{2-}]_0$ and $[H^+]_0$ shows large-amplitude pH oscillations of typically 4.5 pH units (range 2.8-7.3), as obtained in earlier studies [8]. Whereas the period of oscillations remains constant (39 min) while $[BrO_3^-]_0$ is being varied, it was found to decrease with gradual increase in the concentration of negative feedback species $[Mn^{2+}]_0$. The reaction was also studied at different flow rates, and the possibility of detecting a chaotic behavior was explored.

2 Experimental Procedure

Reagent-grade chemicals Na_2SO_3, $HClO_4$, $MnSO_4.H_2O$ and $NaBrO_3$ were used for the daily preparation of the needed solutions. A CSTR configuration was set as described by Okazaki and Hanazaki [15]. A water-jacketed quartz-glass beaker (double-walled) was employed as the reactor. Four stock solutions placed in three different beakers (one containing both SO_3^{2-} and H^+, another Mn^{2+} and the third one BrO_3^-) were brought into the reactor through glass capillary tubes connected by bendable Teflon tubes using regulated peristaltic pumps. $SO_3^{2-}$and H^+ were placed in one reservoir because their concentrations were held constant throughout the different runs, while Mn^{2+} and BrO_3^- were being varied. The flow rate of all the pumps was controlled by the voltage generated using a National Instruments toolkit interface with the *Labview software*. The pumps were connected to separate channels. The flow rate of each pump was then calibrated separately, as a function of the voltage. A schematic representation of the setup is shown in Fig. 1.

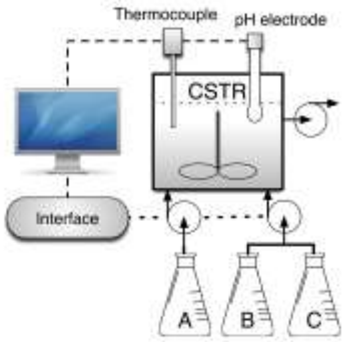

Figure 1: Experimental setup showing the CSTR, the reagent sources (flasks) and the corresponding pumps. Flask A: Mn^{2+}; Flask B: BrO_3^-; Flask C; H^+ and SO_3^{2-}.

The reaction mixture was vigorously stirred by a Teflon coated magnetic stirrer bar. As soon as the volume of the mixture reaches 9.0 mL, aspiration from the top of the reactor is operated in a way to maintain this volume constant throughout the remainder of the experiment. A thermostat bath providing water circulation to the reactor was used to maintain the reaction temperature at 45.0 ± 0.1 ºC. The pH of the mixture was monitored by continuous measurement using a calibrated glass/combination electrode, vertically inserted in the reaction mixture and connected to the NI interface. A thermocouple was also connected to monitor the temperature of the reactor. The sampling rate was 2 Hz, which yields a rate of 2 pH readings/sec.

3 Results and Discussion

Within the settings and configuration of our CSTR, we use a range of bromate concentrations notably higher than the one used by Okazaki *et al.* [8], but we keep the concentrations of the other species essentially similar, i.e. $[Mn^{2+}]_0$ = 9.0 mM, $[SO_3^{2-}]_0$ = 118 mM and $[H^+]_0$ = 16.5 mM. The inlet flow rate is regulated at k_{in} = 1.59 mL/ min. This corresponds to a residence time of 5.66 min for a fixed CSTR volume of 9.00 mL ($t_{res.} = V_{CSTR} / k_{in}$). Note that in our experiments, the outlet flow rate k_{out} is threefold larger, that is, k_{out} = 4.77 mL/min, since the solutions in the *three* reservoirs are pumped in separately, while they are drained out of the reactor at once.

We explored the range $[BrO_3^-]_0$ = 250 to 1500 mM, with $[Mn^{2+}]_0$, $[SO_3^{2-}]_0$ and $[H^+]_0$ held constant as specified above, and according to Ref. [8]. Some of these concentrations exhibited oscillations and others did not. Over the $[BrO_3^-]_0$ range 90 – 300 mM, no oscillations were observed within the frame of our experimental CSTR settings. We jumped to higher $[BrO_3^-]_0$, starting particularly with $[BrO_3^-]_0$ = 590 mM. The first important result is the large-amplitude oscillations ranging from pH_{lo} = 2.00 to pH_{hi} = 7.46, with a pH amplitude 5.46.

This value exceeds the amplitude reported by Okazaki *et al.* [8] (4.5 pH units) by about 1 pH unit (0.96). In addition, the period is 10.9 min, compared to 39.1

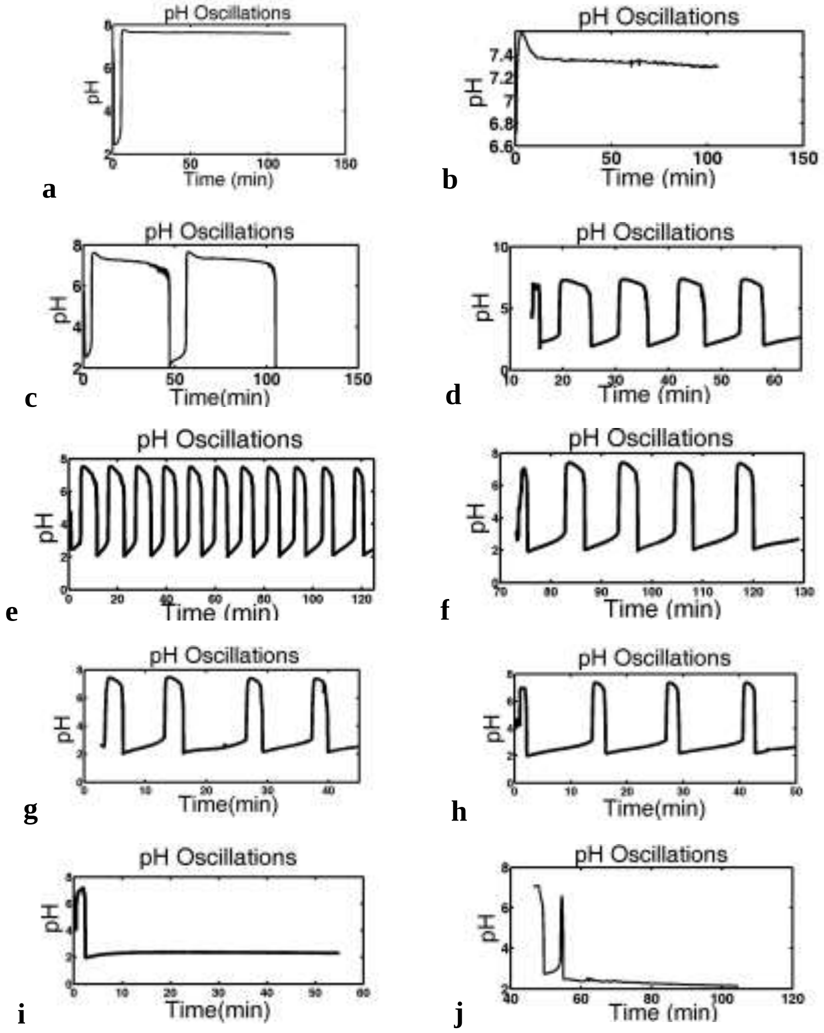

Figure 2: Oscillations obtained in the BSH reaction with $[Mn^{2+}]_0$ = 9.0 mM used a negative feedback; $[H^+]_0$ = 16.5 mM, $[SO_3^{2-}]_0$ = 118 mM, with $[BrO_3^-]_0$ = (a) 350, (b) 385, (c) 450, (d) 560, (e) 590, (f) 620, (g) 730, (h) 800, (i) 1000, and (j)1500 mM.

min. reported by Okazaki *et al.* [8]. So we continue to vary $[BrO_3^-]_0$ throughout the rest of the study, i.e. explore the region 300-590 mM and then above 590 mM (the first $[BrO_3^-]_0$ with satisfactory oscillations). The obtained behavior for some relevant chosen BrO_3^- concentrations is displayed in Fig. 2. This wide range of BrO_3^- concentrations enables us to construct a bifurcation diagram in the pH – $[BrO_3^-]_0$ space, delineating the various regions with different characteristic behaviors. Such a bifurcation diagram is depicted in Fig. 3. It highlights the high steady state region (SSH), low steady state region (SSL) and the oscillatory regime (OR). At low $[BrO_3^-]_0$ values, only SSH is stable.

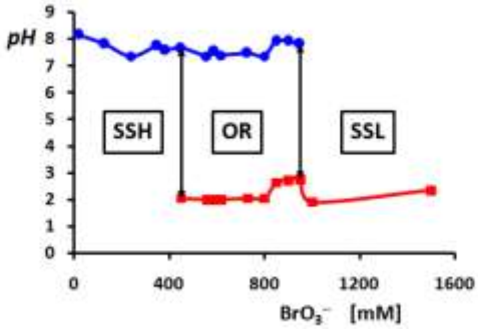

Figure 3: Bifurcation diagram in the Mn^{2+}- BrO_3^-- SO_3^{2-}-H^+ system with $[Mn^{2+}]_0$ = 9.0 mM. One (steady-state) or two (oscillatory region) pH values are plotted for each $[BrO_3^-]_0$ run. The framed labels read as follows: SSH (Steady-State High); OR (Oscillatory Region); SSL (Steady-State Low).

Upon increasing $[BrO_3^-]_0$ through the concentration 385 mM (among our tested values), the system experiences a transition (bifurcation) to an onset of oscillations (OR region). At $[BrO_3^-]_0 \geq 1000$ mM, as shown in Fig. 2 (frames **i** and **j**), the system is stable in the low pH regime. This is illustrated in the bifurcation diagram, and appears in the region labeled SSL (low pH steady state).

The variation of the amplitude and period of oscillation with the initial bromate concentration $[BrO_3^-]_0$ is shown in Fig. 4. We can see that the amplitude, and period of oscillations (beyond 450 mM) remain essentially constant (the range in Figure 4.a spans only about 0.5 pH unit).

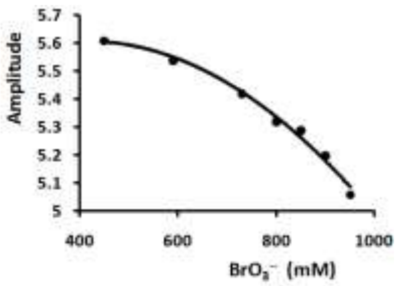

a

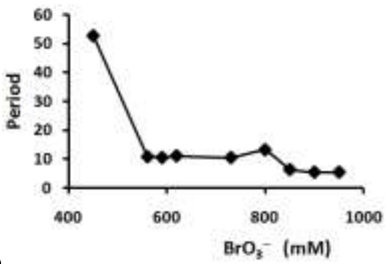

b

Figure 4: a. Variation of the amplitude of pH oscillations with bromate concentration $[BrO_3^-]_0$. b. Variation of the period of oscillations with bromate concentration $[BrO_3^-]_0$.

Among all the experiments done, $[BrO_3^-]_0$ = 590 mM is selected for the variation of flow rate, achieved by changing the voltages on the pumps.

Upon decreasing the flow rate to 1.35 mL/min, the period increased to 26.4 min, almost twice the value measured for k_{in} = 1.59 mL/min, as clearly shown in Fig. 5.

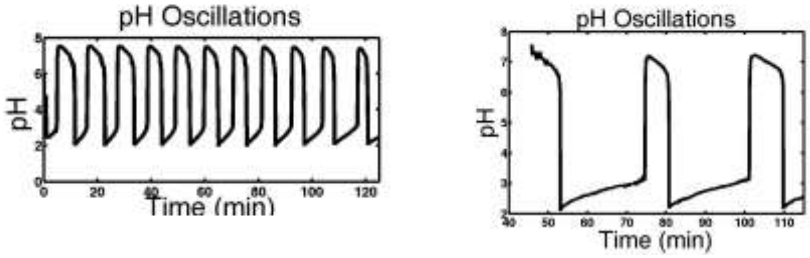

Figure 5: Effect of decreasing the flow rate from 1.59 to 1.35 mL/min for constant $[BrO_3^-]_0$ = 590 mM. The figure shows the pH oscillation at two different flow rates. a. $[BrO_3^-]_0$ = 590 mM, with k = 1.59 mL/min. b. $[BrO_3^-]_0$ = 590 mM, with k = 1.35 mL/min.

This can be considered as a period-doubling effect. Since the route to chaos starts with period-doubling and then followed by further increase (period-quadrupling etc.), we tried decreasing the flow rate further. We carried out runs at flow rates 1.260, 0.686 and 0.502 mL/min. No further ascent in the period of oscillation was obtained. As a second alternative, instead of decreasing the flow rate, we increased k_{in} to 1.89, 2.64 and 3.26 mL/min respectively. However none of the runs exhibited any noticeable change of interest, in particular the anticipated chaos.

We now vary $[Mn^{2+}]_0$, keeping the other concentrations constant. The results are displayed in Fig. 6.

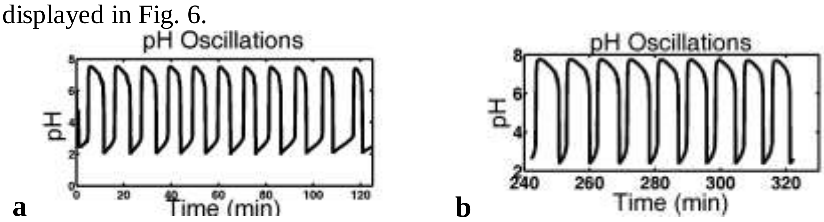

Figure 6: BSH runs at fixed $[BrO_3^-]_0$ = 590 mM, $[H^+]$ = 16.5 mM, $[SO_3^{2-}]$ = 118 mM, but with $[Mn^{2+}]$ = 9.0 (a), and 13.0 mM (b). The period of oscillations decreases here from 10.9 to 8.7 min.

Upon increasing $[Mn^{2+}]_0$ from 7.2 to 9.0 to 13.0 mM, the period decreased from 11.76 min to 10.86 min to 8.66 minutes respectively. In the absence of $[Mn^{2+}]_0$, no oscillations were found indicating that Mn^{2+} plays an important role in the reaction mechanism, under the prevailing experimental conditions. It is worth noting that here again, the variation of $[Mn^{2+}]_0$ did not show any transition to chaotic behavior. Another interesting observation is that the duration of the low-pH stage decreases from 5.2 to 2.7 min. as $[Mn^{2+}]_0$ increases from 9.0 mM to 13.0 mM respectively, while that of the high pH stage remains constant (5.7 min.) as seen in Fig. 6. The latter trend agrees with the results of Okazaki et al. [8]. At very low $[Mn^{2+}]_0$, Mn^{2+} becomes insufficient for consuming protons, and thus the low pH regime lasts gradually longer, until the transition to high pH is suppressed (oscillations cease). According to Okazaki et al. [8], among the stable Mn^{2+} species in the pH range 3-4 ($Mn(OH)^{2+}$, $Mn(OH)_2^{2+}$, and $MnO(OH)^+$), $MnO(OH)^+$ plays the most important role, and undergoes the reaction:

$$MnO(OH)^+ + 2\,HSO_3^- + 2\,H^+ \longrightarrow Mn^{2+} + HS_2O_6^- + 2\,H_2O \quad (2)$$

$MnO(OH)^+$ is readily produced from Mn^{2+} according to:

$$3\,Mn^{2+} + BrO_3^- + 3\,H_2O \longrightarrow 3\,MnO(OH)^+ + Br^- + 3\,H^+ \quad (3)$$

The predominance of $MnO(OH)^+$, coupled to the dependence on $[BrO_3^-]_0$, suggest that reaction (2) is the relevant process for the negative feedback scheme, contributed by the presence of Mn^{2+}. Finally, it is quite interesting to realize that the $[BrO_3^-]_0$ = 590 mM/$[Mn^{2+}]_0$ = 9.0 mM conditions produce oscillations with essentially equal durations of low and high pH stages (5.2 and 5.7 min. respectively).
It was further suggested [8] that the employment of two negative feedback species could produce chaotic pH-oscillations. To test this possibility, Mn^{2+} was combined with MnO_4^-, another known negative feedback species.

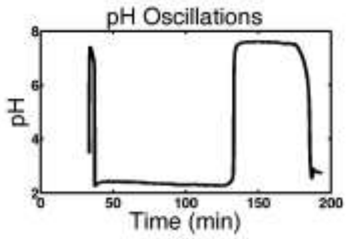

Figure 7: BSH run with two negative feedback species. $[Mn^{2+}]$ = 9.0 mM and $[MnO_4^-]$ = 1.5 mM, with $[BrO_3^-]$ = 590 mM.

The result is shown in Fig. 7, without any noticeable sign of chaos. So with all those explored possibilities (variation in flow rate, $[Mn^{2+}]_0$ or use of two negative feedback species), no chaotic oscillations were observed.

4 Conclusions

The $[BrO_3^-]_0$ regime used here resulted in a *larger amplitude* and a *shorter period* than the values obtained in Ref. [8]. Furthermore, the system exhibited a period-doubling upon only one variation of flow rate. However, as discussed earlier, this system did not display any chaotic behavior in the whole range of BrO_3^- and Mn^{2+} concentrations explored, flow rate domains, or through the use of two negative feedback species. A *bifurcation diagram* was constructed, delineating the steady-state and oscillatory regimes.

Other suggested attempts to reach chaos in future studies on this system are, to name but a few, changing parameters such as the stirring rate and the temperature of the CSTR, in addition to variations in $[SO_3^{2-}]$ and $[H^+]$.

Acknowledgements: This work was supported by a University Research Board (URB) grant (American University of Beirut).

References

1. R. Field and M. Burger *Oscillations and Traveling Waves in Chemical Systems*, Wiley, New York, 1985.
2. W. C. Bray and H. A. Liebhafsky. *J. Am. Chem. Soc*. 53:38, 1931.
3. T. S. Briggs and W. C. Rauscher. *J. Chem. Educ.* 50:496, 1973.
4. V. Castets, E. Dulos, J. Boissonade, and P. De Kepper. *Phys. Rev. Lett.* 64:2953–2956, 1990.
5. B. P. Belousov. *Sbornik Refratov po Radiatsionni Meditsine*, Medgiz, Moscow, 1958, p. 145.
6. A. M. Zhabotinskii, Biofizika, 9:306, 1964.
7. R. J. Field, E. Körös and R. M. Noyes. *J. Am. Chem. Soc.* 94:8649, 1972.
8. N. Okazaki, G. Rabai and I. Hanazaki. *J. Phys. Chem. A* 103:10915-10920, 1999.
9. K. M. Kovacs and G. Rabai. *J. Phys. Chem. A* 105:9183-9187, 2001.
10. T. G. Szanto and R. Gyula. *J. Phys. Chem. A* 109:5398-5402, 2005.
11. M. Orbán and I. R. Epstein. *J. Am. Chem. Soc.* 107:2302, 1985.
12. E. C. Edblom, M. Orbán, and I. R. Epstein. *J. Am. Chem. Soc.* 108:2826, 1986.
13. E. C. Edblom, L. Gyorgyi, M. Orbán, and I. R. Epstein. *J. Am. Chem. Soc.* 109:4876, 1987.
14. E. C. Edblom, Y. Luo, M. Orbán, K. Kustin, and I. R. Epstein. *J. Phys. Chem.* 93:2722, 1989.
15. N. Okazaki and I. Hanazaki. *J. Chem. Phys.* 109:637, 1998.

Chaotic Modeling and Simulation (CMSIM) 2: 395-447, 2012

Universality of Tsallis Non-Extensive Statistics and Fractal Dynamics for Complex Systems

G.P. Pavlos[1], M.N. Xenakis[2], L.P. Karakatsanis[1], A.C. Iliopoulos [1], A.E.G. Pavlos [3], D.V. Sarafopoulos [1]

[1]Department of Electrical and Computer Engineering, Democritus University of Thrace, 67100 Xanthi, Greece (Email: gpavlos@ee.duth.gr)
[2]German Research School for Simulation Sciences, Aachen, Germany
[3]Department of Physics, Aristotle University of Thessaloniki, 54624 Thessaloniki, Greece

Abstract: Tsallis q-extension of statistics and fractal generalization of dynamics are two faces of the same physical reality, as well as the Kernel modern complexity theory. The fractal generalization dynamics is based at the multiscale – multifractal characters of complex dynamics in the physical space-time and the complex system's dynamical phase space. Tsallis q-triplet of non-extensive statistics can be used for the experiment test of q-statistic as well as of the fractal dynamics. In this study we present indicative experimental verifications of Tsallis theory in various complex systems such as solar plasmas, (planetic magnetospheres, cosmic stars and cosmic rays), atmospheric dynamics, seismogenesis and brain dynamics.
Keywords: Tsallis non-extensive statistics, Non-equilibrium phase transition, intermittent turbulence, Self Organized Criticality, Low Dimensional Chaos, Magnetosphere, Superstorm.

1. Introduction

Physical theory today has been led into admirable experience and knowledge. Namely, at all levels of physical reality a global ordering principle is operating. Prigogine [1], Nicolis [2], Davies [3], El Naschie [4], Iovane [5], Nottale [6], Castro [7]. All classical physical theory dominates the Demokritean and Euclidean reductionistic point of view. That is, cosmos is created from elementary particles which obey to the fundamental laws, space consists of points and time from moments points or moments have zero measure. In Einstein's relativistic physical theory Democritean (elementary material particles) and Euclidian (points, space, point view) are joined into a unified physical entity that of the space time manifold. Here, geometry explains physics since the forces-fields are identified with the curvature of the space-time manifold. Although Einstein showed, with a rare genius way, the unity of universe through a mathematization and geometrization modification of the

ISSN 2241-0503

cosmos subject-matter, however he didn't escape from the reductionistic and deterministic point of view [8]. According to this concept, the observed and macroscopic reality is illusion as the only existed reality is the fundamental geometrical and objective reality of the space-time manifold in general. This is the Democritian, Parmenidian, Euclidian, Spinozian point of view.

The overthrow of the dogmatic determinism and reductionism in science started to be realized after the novel concept of Heisenberg according to which the physical magnitude properties are not objective and divided realities but operators as the dynamical states are infinite dimensional vectors. This new concept of Heisenberg led to a new theoretical status corresponding to a microscopical complexity point view of cosmos. Neuman inspired from Heisenberg's novel theory introduced non-commutatively in geometry, according to which Space does not consist of points but from "states". In addition, superstring theory forced physicists to introduce non-commutatively at the Planck scale of space-time, confirming Neuman's as well as Heisenberg's intuition. This, of course, was the initiation of an avalanche of serious of changes in the fundamentals of physical theory, corresponding to new theoretical concepts as: poly-dimensional and p-adic physics, scale relativity fractal dynamics and fractal space-time etc El Naschie [4], Khrenminov [9], Nottale [6], Castro [7], Kroger [10], Pezzaglia [11], Tarasov [12], El-Naboulsis [13], Gresson [14], Goldfain [15].

Prigogine [1] and Nicolis [2] were the principal leaders of an outstanding transition to the new epistemological ideas in the macroscopical level. Far from equilibrium they discover an admirable operation of the physical-chemical systems. That is, the discovered the possibility of long range spatiotemporal correlations development when the system lives far from equilibrium. Thus, Prigogine and Nicolis opened a new road towards to the understanding of random fields and statistics, which lead to a non-Gaussian reality. This behavior of nature is called Self-Organization. Prigogine's and Nicoli's self-organized concepts inspired one of the writers of this paper to introduce the self organization theory as basic tool to interpret the dynamics of the space plasmas dynamics [16] as well as seismogenesis [17] as a result of the self organization of Earth's manage-crust system. However Lorenz[18] had discovered the Lorenz's attractor as the weather's self organization process while other scientists had observed the self organization of fluids (e.g. dripping faucet model) or else, verifying the Feinebaum [19] mathematical scenarios to complexity includes in nonlinear maps or Ordinary Differential Equations – Partial Differential Equations [20]. However, scientists still now prefers to follow the classical theory, namely that macro-cosmos is just the result of fundamental laws which can be traced only at the microscopical level. Therefore, while the supporter of classical reductionistic theory considers the chaos and the self organization macroscopic characteristics that they ought to be the result of the fundamental Lagrangian or the fundamental Hamiltonian of nature, there is an ongoing a different perception. Namely, that macroscopic chaos and complexity not only cannot be explained by the hypothetical microscopic simplicity but they are present also in the microscopic reality.

Therefore, scientists like Nelson [21], Hooft [22], Parisi [23], Beck [24] and others used the complexity concept for the explanation of the microscopic "simplicity", introducing theories like stochastic quantum field theory or chaotic field theory. This new perception started to appear already through the Wilsonian theories of renormalization which showed the multiscale cooperation of the physical reality [25]. At the same time, the multiscale cooperativity goes with the self similarity characters of nature that allows the renormalization process. This leads to the utilization of fractal geometry into the unification of physical theories, as the fractal geometries are characterized by the scaling property which includes the multiscale and self similar character. Scientists like Ord [26], El Naschie [4], Nottale [6] and others, will introduce the idea of fractal geometry into the geometry of space-time, negating the notion of differentiability of physical variables. The fractal geometry is connected to non-commutative geometry since at fractal objects the principle of self similarity negates the notion of the simple geometrical point just like the idea of differentiability. Therefore, the fractal geometry of space-time is leading to the fractal extension of dynamics exploiting the fractal calculus (fractal integrals-fractal derivatives) [27]. Also, the fractal structure of space-time has intrinsically a stochastic character since a presupposition for determinism is differentiability [6, 14]. Thus, in this way, statistics are unified with dynamics automatically, while the notion of probability obtains a physical substance, characterized as dynamical probabilism. The ontological character of probabilism can be the base for the scientific interpretation of self-organization and ordering principles just as Prigogine [1] had imagined, following Heisenberg's concept. From this point of view, we could say that contemporary physical theory returns to the Aristotetiles point of view as Aristotelianism includes the Newtonian and Democritian mechanistical determinism as one component of the organism like behavior of Nature [28].

Modern evolution of physical theory as it was described previously is highlighted in Tsallis q-statistics generalization of the Boltzmann-Gibbs statistics which includes the classical (Gaussian) statistics, as the $q=1$ limit of thermodynamical equilibrium. Far from equilibrium, the statistics of the dynamics follows the q-Gaussian generalization of the B-G statistics or other more generalized statistics. At the same time, Tsallis q-extension of statistics can be produced by the fractal generalization of dynamics. The traditional scientific point of view is the priority of dynamics over statistics. That is dynamics creates statistics. However for complex system their holistic behaviour does not permit easily such a simplification and division of dynamics and statistics. Tsallis $q-$statistics and fractal or strange kinetics are two faces of the same complex and holistic (non-reductionist) reality.

Moreover, the Tsallis statistical theory including the Tsallis extension of entropy to what is known as q-entropy [29], the fractal generalization of dynamics [6, 7] and the scale extension of relativity theory C [6, 7] are the cornerstones of modern physical theory related with nonlinearity and non-integrability as well as with the non-equilibrium ordering and self organization. In the following, in section (2) we present the theoretical concepts of q-statistics and fractal dynamics, while in section (3) we present indicative experimental verification of the Tsallis statistical theory. Finally in section (4) we present estimations of q-statistics index for various kinds of complex systems and in section (5) we summarize and discuss the results of this study.

2. Theoretical Concepts

2.1 Complexity Theory and the Cosmic Ordering Principle

The conceptual novelty of complexity theory embraces all of the physical reality from equilibrium to non-equilibrium states. This is noticed by Castro [7] as follows: *"…it is reasonable to suggest that there must be a deeper organizing principle, from small to large scales, operating in nature which might be based in the theories of complexity, non-linear dynamics and information theory which dimensions, energy and information are intricately connected." [7].* Tsallis non-extensive statistical theory [29] can be used for a comprehensive description of space plasma dynamics, as recently we became aware of the drastic change of fundamental physical theory concerning physical systems far from equilibrium.

The dynamics of complex systems is one of the most interesting and persisting modern physical problems including the hierarchy of complex and self-organized phenomena such as: intermittent turbulence, fractal structures, long range correlations, far from equilibrium phase transitions, anomalous diffusion – dissipation and strange kinetics, reduction of dimensionality etc [30-37].

More than other scientists, Prigogine, as he was deeply inspired by the arrow of time and the chemical complexity, supported the marginal point of view that the dynamical determinism of physical reality is produced by an underlying ordering process of entirely holistic and probabilistic character at every physical level. If we accept this extreme scientific concept, then we must accept also for complex systems the new point of view, that the classical kinetic is inefficient to describe sufficiently the emerging complex character as the system lives far from equilibrium. However resent evolution of the physical theory centered on non-linearity and fractality shows that the Prigogine point of view was so that much extreme as it was considered at the beginning.

After all, Tsallis $q-$extension of statistics [29] and the fractal extension for dynamics of complex systems as it has been developed by Notalle [6], El Naschie [4], Castro [7], Tarasov [12], Zaslavsky [38], Milovanov [32], El Nabulsi [13], Cresson [14], Coldfain [15], Chen [39], and others scientists, they are the double face of a unified novel theoretical framework, and they constitute the appropriate base for the modern study of non-equilibrium dynamics as the q-statistics is related at its foundation to the underlying fractal dynamics of the non-equilibrium states.

For complex systems near equilibrium the underlying dynamics and the statistics are Gaussian as it is caused by a normal Langevin type stochastic process with a white noise Gaussian component. The normal Langevin stochastic equation corresponds to the probabilistic description of dynamics by the well-known normal Fokker – Planck equation. For Gaussian processes only the moments-cumulants of first and second order are non-zero, while the central limit theorem inhibits the development of long range correlations and macroscopic self-organization, as any kind of fluctuation quenches out exponentially to the normal distribution. Also at equilibrium, the dynamical attractive phase space is practically infinite dimensional as the system state evolves in all dimensions according to the famous ergodic theorem of Boltzmann – Gibbs statistics. However, in Tsallis $q-$statistics even for the case of $q=1$ (corresponding to Gaussian process) the non-extensive character permits the development of long range correlations produced by equilibrium phase transition multi-scale processes according to the Wilson RGT [40]. From this point of view, the classical mechanics (particles and fields), including also general relativity theory, as well as the quantum mechanics – quantum field theories, all of them are nothing else than a near thermodynamical equilibrium approximation of a wider theory of physical reality, characterized as complexity theory. This theory can be related with a globally acting ordering process which produces the $q-$statistics and the fractal extension of dynamics classical or quantum.

Generally, the experimental observation of a complex system presupposes non-equilibrium process of the physical system which is subjected to observation, even if the system lives thermodynamically near to equilibrium states. Also experimental observation includes discovery and ascertainment of correlations in space and time, as the spatio-temporal correlations are related or they are caused by from the statistical mean values fluctuations. The theoretical interpretation prediction of observations as spatial and temporal correlations – fluctuations is based on statistical theory which relates the microscopic underling dynamics with the macroscopic observations indentified to statistical moments and cumulants. Moreover, it is known that statistical moments and cumulants are related to the underlying dynamics by the derivatives of the partition function (Z) to the external source variables (J) [41].

From this point of view, the main problem of complexity theory is how to extend the knowledge from thermodynamical equilibrium states to the far from equilibrium physical states. The non-extensive $q-$statistics introduced by Tsallis [29] as the extension of Boltzmann – Gibbs equilibrium statistical theory is the appropriate base for the non-equilibrium extension of complexity theory. The far from equilibrium $q-$statistics can produce the q-partition function

(Z_q) and the corresponding $q-$moments and cumulants, in correspondence with Boltzmann – Gibbs statistical interpretation of thermodynamics.

The miraculous consistency of physical processes at all levels of physical reality, from the macroscopic to the microscopic level, as well as the inefficiency of existing theories to produce or to predict the harmony and hierarchy of structures inside structures from the macroscopic or the microscopic level of cosmos. This completely supports or justifies such new concepts as that indicated by Castro [7]: *"of a global ordering principle or that indicated by Prigogine, about the becoming before being at every level of physical reality."* The problem however with such beautiful concepts is how to transform them into an experimentally testified scientific theory.

The Feynman path integral formulation of quantum theory after the introduction of imaginary time transformation by the Wick rotation indicates the inner relation of quantum dynamics and statistical mechanics [42, 43]. In this direction it was developed the stochastic and chaotic quantization theory [22-24, 44], which opened the road for the introduction of the macroscopic complexity and self-organization in the region of fundamental quantum field physical theory. The unified character of macroscopic and microscopic complexity is moreover verified by the fact that the $n-$point Green functions produced by the generating functional $W(J)$ of QFT after the Wick rotation can be transformed to $n-$point correlation functions produced by the partition function $Z(J)$ of the statistical theory. This indicates in reality the self-organization process underlying the creation and interaction of elementary particles, similarly to the development of correlations in complex systems and classical random fields Parisi [23]. For this reason lattice theory describes simultaneously microscopic and macroscopic complexity [40, 42].

In this way, instead of explaining the macroscopic complexity by a fundamental physical theory such as QFT, Superstring theory, M-theory or any other kind of fundamental theory we become witnesses of the opposite fact, according to what Prigogine was imagining. That is, macroscopic self-organization process and macroscopic complexity install their kingdom in the heart of reductionism and fundamentalism of physical theory. The Renormalizable field theories with the strong vehicle of Feynman diagrams that were used for the description of high energy interactions or the statistical theory of critical phenomena and the nonlinear dynamics of plasmas [45] lose their efficiency when the complexity of the process scales up [40].

Many scientist as Chang [31], Zelenyi [30], Milovanov [32], Ruzmaikin [33], Abramenko [36], Lui[46], Pavlos[37], in their studies indicate the statistical non-extensivity as well as the multi-scale, multi-fractal and anomalous – intermittent character of fields and particles in the space plasmas and other complex systems far from equilibrium. These results verify the concept that space plasmas and other complex systems dynamics are part of the more general theory of fractal dynamics which has been developed rapidly the last years. Fractal dynamics are the modern fractal extension of physical theory in every level. On the other side the fractional generalization of modern physical theory is based on fractional calculus: fractional derivatives or integrals or fractional calculus of scalar or vector fields and fractional functional calculus [12, 39]. It is very impressive the efficiency of fractional calculus to describe complex and far from equilibrium systems which display scale-invariant properties, turbulent dissipation and long range correlations with memory preservation, while these characteristics cannot be illustrated by using traditional analytic and differentiable functions, as well as, ordinary differential operators. Fractional calculus permits the fractal generalization of Lagrange – Hamilton theory of Maxwell equations and Magnetohydrodynamics, the Fokker – Planck equation Liouville theory and BBGKI hierarchy, or the fractal generalization of QFT and path integration theory [12-15, 39].

According to the fractal generalization of dynamics and statistics we conserve the continuity of functions but abolish their differentiable character based on the fractal calculus which is the non-differentiable generalization of differentiable calculus. At the same time the deeper physical meaning of fractal calculus is the unification of microscopic and macroscopic dynamical theory at the base of the space – time fractality [4, 6, 39, 47-49]. Also the space-time is related to the fractality – multi-fractality of the dynamical phase – space, whish can be manifested as non-equilibrium complexity and self-organization.

Moreover fractal dynamics leads to a global generalization of physical theory as it can be related with the infinite dimension Cantor space, as the microscopic essence of physical space – time, the non-commutative geometry and non-commutative Clifford manifolds and Clifford algebra, or the p-adic physics [4, 7, 13, 50, 51]. According to these new concepts introduced the last two decades at every level of physical reality we can describe in physics complex structure which cannot be reduced to underlying simple fundamental entities or underlying simple fundamental laws. Also, the non-commutative character of physical theory and geometry indicates [51, 52] that the scientific observation is nothing more than the observation of undivided complex structures in every level. Cantor was the founder of the fractal physics creating fractal sets by contraction of the homogenous real number set, while on the other side the set of real numbers can be understood as the result of the observational coarse graining [27, 50, 53]. From a philosophical point of view the mathematical forms are nothing else than self-organized complex structures of the mind-brain, in self-consistency with all the physical reality. On the other side, the generalization of Relativity theory to scale relativity by Nottale [6] or Castro [7] indicates the unification of microscopic and macroscopic dynamics through the fractal generalization of dynamics.

After all, we conjecture that the macroscopic self-organization related with the novel theory of complex dynamics, as they can be observed at far from equilibrium dynamical physical states, are the macroscopic emergence result of the microscopic complexity which can be enlarged as the system arrives at bifurcation or far from equilibrium critical points. That is, far from equilibrium the observed physical self-organization manifests the globally active ordering principle to be in priority from local interactions processes. We could conjecture that is not far from truth the concept that local interactions themselves are nothing else than local manifestation of the holistically active ordering principle. That is what until now is known as fundamental lows is the equilibrium manifestation or approximation of the new and globally active ordering principle. This concept can be related with the fractal generalization of dynamics which is indentified with the dynamics of correlations supported by Prigogine [1], Nicolis [2] and Balescu [54], as the generalization of Newtonian theory. This conjecture concerning the fractal unification of macroscopic and microscopic dynamics at can be strongly supported by the Tsallis nonextensive q-statistics theory which is verified almost everywhere from the microscopic to the macroscopic level [7, 29]. From this point of view it is reasonable to support that the q-statistics and the fractal generalization of space plasma dynamics is the appropriate framework for the description of their non-equilibrium complexity.

2.2 Chaotic Dynamics and Statistics

The macroscopic description of complex systems can be approximated by non-linear partial differential equations of the general type:

$$\frac{\partial \vec{U}(\vec{x},t)}{\partial t} = \vec{F}(\vec{u},\vec{\lambda}) \tag{1}$$

where u belongs to a infinite dimensional state (phase) space which is a Hilbert functional space. Among the various control parameters, the plasma Reynold number is the one which controls the quiet static or the turbulent plasma states. Generally the control parameters measure the distance from the thermodynamical equilibrium as well as the critical or bifurcation points of the system for given and fixed values, depending upon the global mathematical structure of the dynamics. As the system passes its bifurcation points a rich variety of spatio-temporal patterns with distinct topological and dynamical profiles can be emerged such as: limit cycles or torus, chaotic or strange attractors, turbulence, Vortices, percolation states and other kinds of complex spatiotemporal structures [31, 49, 55-63].

Generally chaotic solutions of the mathematical system (1) transform the deterministic form of equation (1) to a stochastic non-linear stochastic system:

$$\frac{\partial \vec{u}}{\partial t} = \vec{\Phi}(\vec{u},\vec{\lambda}) + \vec{\delta}(\vec{x},t) \tag{2}$$

where $\vec{\delta}(\vec{x},t)$ corresponds to the random force fields produced by strong chaoticity [64, 65].

The non-linear mathematical systems (1-2) include mathematical solutions which can represent plethora of non-equilibrium physical states included in mechanical, electromagnetic or chemical and other physical systems which are study here.

The random components ($\delta(\vec{x},t)$) are related to the BBGKY hierarchy:

$$\frac{\partial f_q}{\partial t} = [H_q, f_a] + S_q, q = 1,2,...,N \tag{3}$$

where f_q is the $q-$particle distribution function, H_q is the $q-$th approximation of the Hamiltonian $q-$th correlations and S_q is the statistical term including correlations of higher than q-orders [45, 65].

The non-linear mathematical systems (1, 2) correspond to the new science known today as complexity science. This new science has a universal character, including an unsolved scientific and conceptual controversy which is continuously spreading in all directions of the physical reality and concerns the integrability or computability of the dynamics [66]. This universality is something supported by many scientists after the Poincare discovery of chaos and its non-integrability as is it shown in physical sciences by the work of Prigogine, Nicolis, Yankov and others [1, 2, 66] in reality. Non-linearity and chaos is the top of a hidden mountain including new physical and mathematical concepts such as fractal calculus, p-adic physical theory, non-commutative geometry, fuzzy anomalous topologies fractal space-time etc [4, 7, 12-15, 38, 39, 50-52]. These new mathematical concepts obtain their physical power when the physical system lives far from equilibrium.

After this and, by following the traditional point of view of physical science we arrive at the central conceptual problem of complexity science. That is, how is it possible that the local interactions in a spatially distributed physical system can cause long range correlations or how they can create complex spatiotemporal coherent patterns as the previous non-linear mathematical systems reveal, when they are solved arithmetically, or in situ observations reveal in space plasma systems. For non-equilibrium physical systems the above questions make us to ask how the development of complex structures and long range spatio-temporal correlations can be explained and described by local interactions of particles and fields. At a first glance the problem looks simple supposing that it can be explained by the self-consistent particle-fields classical interactions. However the existed rich phenomenology of complex non-equilibrium phenomena reveals the non-classical and strange character of the universal non-equilibrium critical dynamics [31, 35].
In the following and for the better understanding of the new concepts we follow the road of non-equilibrium statistical theory [31, 36]
The stochastic Langevin equations (11, 13, 17) can take the general form:

$$\frac{\partial u_i}{\partial t} = -\Gamma(\vec{x}) \frac{\delta H}{\delta u_i(\vec{x},t)} + \Gamma(\vec{x}) n_i(\vec{x},t) \tag{4}$$

where H is the Hamiltonian of the system, $\delta H / \delta u_i$ its functional derivative, Γ is a transport coefficient and n_i are the components of a Gaussian white noise:

$$\left.\begin{aligned} &< n_i(\vec{x},t) >= 0 \\ &< n_i(\vec{x},t) n_j(\vec{x}',t') >= 2\Gamma(\vec{x})\delta_{ij}\delta(\vec{x}-\vec{x}')\delta(t-t') \end{aligned}\right\} \tag{5}$$

[31, 65, 67, 68]. The above stochastic Langevin Hamiltonian equation (18) can be related to a probabilistic Fokker – Planck equation [31]:

$$\frac{1}{\Gamma(\vec{x})}\frac{\partial P}{\partial t} = \frac{\delta}{\delta \vec{u}} \cdot \left(\frac{\delta \mathrm{H}}{\delta \vec{u}} P + \frac{\delta}{\delta \vec{u}} \left[\Gamma(\vec{x}) P \right] \right) \tag{6}$$

where $P = P\left(\left\{u_i(\vec{x},t)\right\},t\right)$ is the probability distribution function of the dynamical configuration $\left\{u_i(\vec{x},t)\right\}$ of the system at time t. The solution of the Fokker – Planck equation can be obtained as a functional path integral in the state space $\left\{u_i(\vec{x})\right\}$:

$$P\left(\left\{u_i(\vec{x})\right\},t\right) \sim \int \Delta\vec{Q} \exp(-S) P_0\left(\left\{u_i(\vec{x})\right\},t_0\right) \tag{7}$$

where $P_0\left(\left\{u_i(\vec{x})\right\},t_0\right)$ is the initial probability distribution function in the extended configuration state space and $S = i\int L dt$ is the stochastic action of the system obtained by the time integration of it's stochastic Lagrangian (L) [31, 69]. The stationary solution of the Fokker – Planck equation corresponds to the statistical minimum of the action and corresponds to a Gaussian state:

$$P\left(\left\{u_i\right\}\right) \sim \exp\left[-\left(1/\Gamma\right)\mathrm{H}\left(\left\{u_i\right\}\right)\right] \tag{8}$$

The path integration in the configuration field state space corresponds to the integration of the path probability for all the possible paths which start at the configuration state $\vec{u}(\vec{x},t_0)$ of the system and arrive at the final configuration state $\vec{u}(\vec{x},t)$. Langevin and F-P equations of classical statistics include a hidden relation with Feynman path integral formulation of QM [23, 31, 42, 43]. The F-P equation can be transformed to a Schrödinger equation:

$$i\frac{d}{dt}\hat{U}\left(t,t_0\right) = \hat{H} \cdot \hat{U}(t,t_0) \tag{9}$$

by an appropriate operator Hamiltonian extension $H\left(u(\vec{x},t)\right) \Rightarrow \hat{H}\left(\hat{u}(\vec{x},t)\right)$ of the classical function (H) where now the field (u) is an operator distribution [31, 68]. From this point of view, the classical stochasticity of the macroscopic Langevin process can be considered as caused by a macroscopic quandicity revealed by the complex system as the F-K probability distribution P satisfies the quantum relation:

$$P\left(u,t\,|\,u,t_0\right)=\left\langle u\,|\,\hat{U}(t,t_0)\,|\,u_0\right\rangle \tag{10}$$

This generalization of classical stochastic process as a quantum process could explain the spontaneous development of long-range correlations at the macroscopic level as an enlargement of the quantum entanglement character at critical states of complex systems. This interpretation is in faithful agreement with the introduction of complexity in sub-quantum processes and the chaotic – stochastic quantization of field theory [22-24, 44], as well as with scale relativity principles [6, 7, 49] and fractal extension of dynamics [4, 12, 13-15, 39] or the older Prigogine self-organization theory [1]. Here, we can argue in addition to previous description that quantum mechanics is subject gradually to a fractal generalization [7, 12, 13-15]. The fractal generalization of QM-QFT drifts along also the tools of quantum theory into the correspondent generalization of RG theory or path integration and Feynman diagrams. This generalization implies also the generalization of statistical theory as the new road for the unification of macroscopic and microscopic complexity.

If $P\left[\vec{u}(\vec{x},t)\right]$ is the probability of the entire field path in the field state space of the distributed system, then we can extend the theory of generating function of moments and cumulants for the probabilistic description of the paths [60, 69]. The n-point field correlation functions (n-points moments) can be estimated by using the field path probability distribution and field path (functional) integration:

$$\left\langle u(\vec{x}_1,t_1)u(\vec{x}_2,t_2)...u(x_n,t_n)\right\rangle=\int\Delta\vec{u}P\left[\vec{u}\left(\vec{x},t\right)\right]u(\vec{x}_1,t_1)...u(\vec{x}_n,t_n) \tag{11}$$

For Gaussian random processes which happen to be near equilibrium the $n-$ th point moments with $n>2$ are zero, correspond to Markov processes while far from equilibrium it is possible non-Gaussian (with infinite nonzero moments) processes to be developed. According to Haken [69] the characteristic function (or generating function) of the probabilistic description of paths:

$$\left[u(x,t)\right]\equiv\left(u(\vec{x}_1,t_1),u(\vec{x}_2,t_2),...,u(\vec{x}_n,t_n)\right) \tag{12}$$

is given by the relation:

$$\Phi_{path}\left(j_1(t_1),j_2(t_2),...,j_n(t_n)\right)=\left\langle \exp i\sum_{i=1}^{N} j_i u(\vec{x}_i,t_i)\right\rangle_{path} \tag{13}$$

while the path cumulants $K_s(t_{a_1}...t_{a_s})$ are given by the relations:

$$\Phi_{path}\left(j_1(t_1),j_2(t_2),...,j_n(t_n)\right)=\exp\left\{\sum_{s=1}^{\infty}\frac{i^s}{s!}\sum_{a_1,...a_s=1}^{n}K_s(t_{a_1}..t_{a_s})\cdot j_{a_1}...j_{a_s}\right\} \tag{14}$$

and the $n-$ point path moments are given by the functional derivatives:

$$\left\langle u(\vec{x}_1,t_1),u(\vec{x}_2,t_2),...,u(\vec{x}_n,t_n)\right\rangle = \left(\delta^n\Phi\left(\{j_i\}\right)/\delta j_1...\delta j_n\right)t\{j_i\}=0 \quad (15)$$

For Gaussian stochastic field processes the cumulants except the first two vanish $\left(k_3 = k_4 = ...0\right)$. For non-Gaussian processes it is possible to be developed long range correlations as the cummulants of higher than two order are non-zero [69]. This is the deeper meaning of non-equilibrium self-organization and ordering of complex systems. The characteristic function of the dynamical stochastic field system is related to the partition functions of its statistical description, while the cumulant development and multipoint moments generation can be related with the BBGKY statistical hierarchy of the statistics as well as with the Feynman diagrams approximation of the stochastic field system [41, 70]. For dynamical systems near equilibrium only the second order cumulants is non-vanishing, while far from equilibrium field fluctuations with higher – order non-vanishing cumulants can be developed.

Finally, we can understand how the non-linear dynamics correspond to self-organized states as the high-order (infinite) non-vanishing cumulants can produce the non-integrability of the dynamics. From this point of view the linear or non-linear instabilities of classical kinetic theory are inefficient to produce the non-Gaussian, holistic (non-local) and self-organized complex character of non-equilibrium dynamics. That is, far from equilibrium complex states can be developed including long range correlations of field and particles with non-Gaussian distributions of their dynamic variables. As we show in the next section such states such states reveal the necessity of new theoretical tools for their understanding which are much different from the classical linear or non-linear approximation of kinetic theory.

2.3 Strange attractors and Self-Organization

When the dynamics is strongly nonlinear then for the far from equilibrium processes it is possible to be created strong self-organization and intensive reduction of dimensionality of the state space, by an attracting low dimensional set with parallel development of long range correlations in space and time. The attractor can be periodic (limit cycle, limit m-torus), simply chaotic (mono-fractal) or strongly chaotic with multiscale and multifractal profile as well as attractors with weak chaotic profile known as SOC states. This spectrum of distinct dynamical profiles can be obtained as distinct critical points (critical states) of the nonlinear dynamics, after successive bifurcations as the control parameters change. The fixed points can be estimated by using a far from equilibrium renormalization process as it was indicated by Chang [31].

From this point of view phase transition processes can be developed by between different critical states, when the order parameters of the system are changing. The far from equilibrium development of chaotic (weak or strong) critical states include long range correlations and multiscale internal self organization. Now, these far from equilibrium self organized states, the equilibrium BG statistics and BG entropy, are transformed and replaced by the Tsallis extension of $q-$statistics and Tsallis entropy. The extension of renormalization group theory and critical dynamics, under the $q-$extension of partition function, free energy and path integral approach has been also indicated [37, 70-72]. The multifractal structure of the chaotic attractors can be described by the generalized Rényi fractal dimensions:

$$D_{\bar{q}} = \frac{1}{\bar{q}-1} \lim_{\lambda \to 0} \frac{\log \sum_{i=1}^{N\lambda} p_i^{\bar{q}}}{\log \lambda}, \tag{16}$$

where $p_i \sim \lambda^{\alpha(i)}$ is the local probability at the location (i) of the phase space, λ is the local size of phase space and $a(i)$ is the local fractal dimension of the dynamics. The Rényi $\bar{q}$ numbers (different from the $q-$index of Tsallis statistics) take values in the entire region ($-\infty, +\infty$) of real numbers. The spectrum of distinct local fractal dimensions $\alpha(i)$ is given by the estimation of the function $f(\alpha)$ [73, 74] for which the following relations hold:

$$\sum p_i^{\bar{q}} = \int d\alpha' p(\alpha')\lambda^{-f(\alpha')} d\alpha' \tag{17}$$

$$\tau(\bar{q}) \equiv (\bar{q}-1)D\bar{q} \overset{\min_a}{=} \bar{q}\alpha - f(\alpha) \tag{18}$$

$$a(\bar{q}) = \frac{d[\tau(\bar{q})]}{d\bar{q}} \tag{19}$$

$$f(\alpha) = \bar{q}\alpha - \tau(\bar{q}), \tag{20}$$

The physical meaning of these magnitudes included in relations (2.15-2.18) can be obtained if we identify the multifractal attractor as a thermodynamical object, where its temperature (T), free energy (F), entropy (S) and internal energy (U) are related to the properties of the multifractal attractor as follows:

$$\left.\begin{array}{ll} \bar{q} \Rightarrow \frac{1}{T}, & \tau(\bar{q}) = (\bar{q}-1)D_q \Rightarrow F \\ \alpha \Rightarrow U, & f(\alpha) \Rightarrow S \end{array}\right\} \tag{21}$$

This correspondence presents the relations (2.17 -2.19) as a thermodynamical Legendre transform [75]. When $\bar{q}$ increases to infinite ($+\infty$), which means, that we freeze the system ($T_{(q=+\infty)} \to 0$), then the trajectories (fluid lines) are closing on the attractor set, causing large probability values at regions of low fractal dimension, where $\alpha = \alpha_{\min}$ and $D_{\bar{q}} = D_{-\infty}$. Oppositely, when

$\overline{q}$ decreases to infinite ($-\infty$), that is we warm up the system ($T_{(q=-\infty)} \to 0$) then the trajectories are spread out at regions of high fractal dimension ($\alpha \Rightarrow \alpha_{\max}$). Also for $\overline{q}\,' > \overline{q}$ we have $D_{\overline{q}'} < D_{\overline{q}}$ and $D_{\overline{q}} \Rightarrow D_{+\infty}(D_{-\infty})$ for $\alpha \Rightarrow \alpha_{\min}(\alpha_{\max})$ correspondingly. However, the above description presents only a weak or limited analogy between multifractal and thermodynamical objects. The real thermodynamical character of the multifractal objects and multiscale dynamics was discovered after the definition by Tsallis [29] of the $q-$entropy related with the $q-$statistics as it was summarized previously in relations (2.1-2.13).

2.4 Intermittent Turbulence

According to previous description dissipative nonlinear dynamics can produce self-organization and long range correlations in space and time. In this case we can imagine the mirroring relationship between the phase space multifractal attractor and the corresponding multifractal turbulence dissipation process of the dynamical system in the physical space. Multifractality and multiscaling interaction, chaoticity and mixing or diffusion (normal or anomalous), all of them can be manifested in both the state (phase) space and the physical (natural) space as the mirroring of the same complex dynamics. We could say that turbulence is for complexity theory, what the blackbody radiation was for quantum theory, as all previous characteristics can be observed in turbulent states. The theoretical description of turbulence in the physical space is based upon the concept of the invariance of the HD or MHD equations upon scaling transformations to the space-time variables ($\vec{X}, t$) and velocity ($\vec{U}$):

$$\overrightarrow{X}\,' = \lambda \overrightarrow{X},\ \ \overrightarrow{U}\,' = \lambda^{\alpha/3}\overrightarrow{U}\,, t' = \lambda^{1-\alpha/3} t \tag{22}$$

and corresponding similar scaling relations for other physical variables [45, 76]. Under these scale transformations the dissipation rate of turbulent kinetic or dynamical field energy E_n (averaged over a scale $\mathrm{l_n} = l_o \delta_n = R_o \delta_n$) rescales as ε_n:

$$\varepsilon_n \sim \varepsilon_0 (\mathrm{l_n} \backslash l_0)^{\alpha-1} \tag{23}$$

Kolmogorov [77] assumes no intermittency as the locally averaged dissipation rate, in reality a random variable, is independent of the averaging domain. This means in the new terminology of Tsallis theory that Tsallis q-indices satisfy the relation $q=1$ for the turbulent dynamics in the three dimensional space. That is the multifractal (intermittency) character of the HD or the MHD dynamics consists in supposing that the scaling exponent α included in relations (2.20, 2.21) takes on different values at different interwoven fractal subsets of the $d-$dimensional physical space in which the dissipation field is embedded. The exponent α and for values $a < d$ is related with the degree of singularity in the field's gradient ($\frac{\partial A(x)}{\partial x}$) in the $d-$dimensional natural space [78]. The gradient singularities cause the anomalous diffusion in physical or in phase space of the dynamics. The total dissipation occurring in a $d-$dimensional space of size l_n scales also with a global dimension $D_{\overline{q}}$ for powers of different order $\overline{q}$ as follows:

$$\sum_n \varepsilon_n^{\overline{q}} l_n^{\ d} \sim l_n^{\ (\overline{q}-1)D_{\overline{q}}} = l_n^{\ \tau(\overline{q})} \tag{24}$$

Supposing that the local fractal dimension of the set $dn(a)$ which corresponds to the density of the scaling exponents in the region ($\alpha, \alpha + d\alpha$) is a function $f_d(a)$ according to the relation:

$$dn(\alpha) \sim \ln^{-f_d(\alpha)} da \tag{25}$$

where d indicates the dimension of the embedding space, then we can conclude the Legendre transformation between the mass exponent $\tau(\overline{q})$ and the multifractal spectrum $f_d(a)$:

$$\left.\begin{aligned} f_d(a) &= a\overline{q} - (\overline{q}-1)(D_{\overline{q}} - d + 1) + d - 1 \\ a &= \frac{d}{d\overline{q}}[(\overline{q}-1)(D_{\overline{q}} - d + 1)] \end{aligned}\right\} \tag{26}$$

For linear intersections of the dissipation field, that is $d = 1$ the Legendre transformation is given as follows:

$$f(a) = a\overline{q} - \tau(\overline{q}),\ \ a = \frac{d}{d\overline{q}}[(q-1)D_q] = \frac{d}{d\overline{q}}\tau(\overline{q}),\ \ \overline{q} = \frac{df(a)}{da} \tag{27}$$

The relations (24-27) describe the multifractal and multiscale turbulent process in the physical state. The relations (16-19) describe the multifractal and multiscale process on the attracting set of the phase space. From this physical point of view, we suppose the physical identification of the magnitudes $D_{\overline{q}}, a, f(a)$ and $\tau(\overline{q})$ estimates in the physical and the corresponding phase space of the dynamics. By using experimental timeseries we can construct the function $D_{\overline{q}}$ of the generalized Rényi $d-$dimensional space dimensions, while the relations (26) allow the calculation of the fractal exponent (a) and the corresponding multifractal spectrum $f_d(a)$. For homogeneous fractals of the turbulent dynamics the generalized dimension spectrum $D_{\overline{q}}$ is constant and equal to the fractal dimension, of the support [76]. Kolmogorov [79] supposed that $D_{\overline{q}}$ does not depend on $\overline{q}$ as the dimension of the fractal support is

$D_q = 3$. In this case the multifractal spectrum consists of the single point ($a = 1$ and $f(1) = 3$). The singularities of degree (a) of the dissipated fields, fill the physical space of dimension d with a fractal dimension $F(a)$, while the probability $P(a)da$, to find a point of singularity (a) is specified by the probability density $P(a)da \sim \ln^{d-F(a)}$. The filling space fractal dimension $F(a)$ is related with the multifractal spectrum function $f_d(a) = F(a) - (d-1)$, while according to the distribution function $\Pi_{dis}(\varepsilon_n)$ of the energy transfer rate associated with the singularity a it corresponds to the singularity probability as $\Pi_{dis}(\varepsilon_n)d\varepsilon_n = P(a)da$ [78]. Moreover the partition function $\sum_i P_i^{\bar{q}}$ of the Rényi fractal dimensions estimated by the experimental timeseries includes information for the local and global dissipation process of the turbulent dynamics as well as for the local and global dynamics of the attractor set, as it is transformed to the partition function $\sum_i P_i^q = Z_q$ of the Tsallis q-statistic theory.

2.5 Fractal generalization of dynamics

Fractal integrals and fractal derivatives are related with the fractal contraction transformation of phase space as well as contraction transformation of space time in analogy with the fractal contraction transformation of the Cantor set [27, 53]. Also, the fractal extension of dynamics includes an extension of non-Gaussian scale invariance, related to the multiscale coupling and non-equilibrium extension of the renormalization group theory [38]. Moreover Tarasov [12], Coldfain [15], Cresson [14], El-Nabulsi [13] and other scientists generalized the classical or quantum dynamics in a continuation of the original break through of El-Naschie [4], Nottale [6], Castro [7] and others concerning the fractal generalization of physical theory.

According to Tarasov [12] the fundamental theorem of Riemann – Liouville fractional calculus is the generalization of the known integer integral – derivative theorem as follows:

if $$F(x) = {}_{\alpha}I_x^{\mathrm{a}} f(x) \tag{28}$$

then $${}_{a}D_x^{\mathrm{a}} F(x) = f(x) \tag{29}$$

where ${}_{a}I_x^{\mathrm{a}}$ is the fractional Riemann – Liouville according to:

$${}_{a}I_x^{\mathrm{a}}\ f(x) \equiv \frac{1}{\Gamma(\mathrm{a})}\int_a^x \frac{f(x')dx'}{(x-x')^{1-\mathrm{a}}} \tag{30}$$

and ${}_aD_x^{\mathrm{a}}$ is the Caputo fractional derivative according to:

$$
\begin{aligned}
&{}_aD_x^{\mathrm{a}}F(x) = {}_aI_x^{n-a}D_x^nF(x) = \\
&= \frac{1}{\Gamma(n-\mathrm{a})}\int_a^x \frac{dx'}{(x-x')^{1+\mathrm{a}-\mathrm{n}}}\frac{dnF(x)}{dx^n}
\end{aligned}
\tag{31}
$$

for $f(x)$ a real valued function defined on a closed interval $[a,b]$.

In the next we summarize the basic concepts of the fractal generalization of dynamics as well as the fractal generalization of Liouville and MHD theory following Tarasov [12]. According to previous descriptions, the far from equilibrium dynamics includes fractal or multi-fractal distribution of fields and particles, as well as spatial fractal temporal distributions. This state can be described by the fractal generalization of classical theory: Lagrange and Hamilton equations of dynamics, Liouville theory, Fokker Planck equations and Bogoliubov hierarchy equations. In general, the fractal distribution of a physical quantity (M) obeys a power law relation:

$$M_D \sim M_0\left(\frac{R}{R_0}\right)^D \tag{32}$$

where (M_D) is the fractal mass of the physical quantity (M) in a ball of radius (R) and (D) is the distribution fractal dimension. For a fractal distribution with local density $\rho(\vec{x})$ the fractal generalization of Euclidean space integration reads as follows:

$$M_D(W) = \int_W \rho(x)dV_D \tag{33}$$

where

$$dV_D = C_3\left(D,\vec{x}\right)dV_3 \tag{34}$$

and

$$C_3\left(D,\vec{x}\right) = \frac{2^{3-D}\Gamma(3/2)}{\Gamma(D/2)}\left|\vec{x}\right|^{D-3} \tag{35}$$

Similarly the fractal generalization of surface and line Euclidean integration is obtained by using the relations:

$$dS_d = C_2\left(d,\vec{x}\right)dS_2 \tag{36}$$

$$C_2\left(d,\vec{x}\right) = \frac{2^{2-d}}{\Gamma(d/2)}\left|\vec{x}\right|^{d-2} \tag{37}$$

for the surface fractal integration and

$$dl_\gamma = C_1(\gamma,\vec{x})dl_1 \tag{38}$$

$$C_1(\gamma,\vec{x}) = \frac{2^{1-\gamma}\Gamma\left(1/2\right)}{\Gamma\left(\gamma/2\right)}\left|\vec{x}\right|^{\gamma-1} \tag{39}$$

for the line fractal integration. By using the fractal generalization of integration and the corresponding generalized Gauss's and Stoke's theorems we can transform fractal integral laws to fractal and non-local differential laws [12] The fractional generalization of classical dynamics (Hamilton Lagrange and Liouville theory) can be obtained by the fractional generalization of phase space quantative description [12]. For this we use the fractional power of coordinates:

$$X^a = \mathrm{sgn}(x)\left|x\right|^a \tag{40}$$

where $\mathrm{sgn}(x)$ is equal to +1 for $x \geq 0$ and equal to -1 for $x < 0$.

The fractional measure $M_{\mathrm{a}}(B)$ of a $n-$ dimension phase space region (B) is given by the equation:

$$M_{\mathrm{a}}(B) = \int_B g(\mathrm{a}) d\mu_{\mathrm{a}}(q,p) \tag{41}$$

where $d\mu_{\mathrm{a}}(q,p)$ is a phase space volume element:

$$d\mu_{\mathrm{a}} = \Pi \frac{dq_K^{\mathrm{a}} \Lambda dp_K^{\mathrm{a}}}{\left[\mathrm{a}\Gamma(\mathrm{a})\right]^2} \tag{42}$$

where $g(\mathrm{a})$ is a numerical multiplier and $dq_K^{\mathrm{a}} \Lambda dp_K^{\mathrm{a}}$ means the wedge product.

The fractional Hamilton's approach can be obtained by the fractal generalization of the Hamilton action principle:

$$S = \int \left[pq - H(t,p,q)\right] dt \tag{43}$$

The fractal Hamilton equations:

$$\left(\frac{dq}{at}\right)^q = \Gamma\left(2-a\right) p^{a-1} D_p^{\mathrm{a}} H \tag{44}$$

$$D_t^{\mathrm{a}} p = -D_q^{\mathrm{a}} H \tag{45}$$

while the fractal generalization of the Lagrange's action principle:

$$S = \int L\left(t,q,u\right) dt \tag{46}$$

Corresponds to the fractal Lagrange equations:

$$D_q^a L - \Gamma\left(2-a\right) D_t^{\mathrm{a}} \left[D_U^{\mathrm{a}} L\right]_{U=\dot{q}} = 0 \tag{47}$$

Similar fractal generalization can be obtained for dissipative or non-Hamiltonian systems [12]. The fractal generalization of Liouville equation is given also as:

$$\frac{\partial \tilde{p}_N}{\partial t} = L_N \tilde{p}_N \tag{48}$$

where $\tilde{p}_N$ and L_N are the fractal generalization of probability distribution function and the Liouville operator correspondingly. The fractal generalization of Bogoliubov hierarchy can be obtained by using the fractal Liouville equation as well as the fractal Fokker Planck hydrodynamical - magnetohydrodynamical approximations [12].

The fractal generalization of classical dynamical theory for dissipative systems includes the non-Gaussian statistics as the fractal generalization of Boltzmann – Gibbs statistics.

Finally the far from equilibrium statistical mechanics can be obtained by using the fractal extension of the path integral method. The fractional Green function of the dynamics is given by the fractal generalization of the path integral:

$$\begin{aligned} K_a\left(x_f, t_f; x_i, t_i\right) &\approx \int_{x_i}^{x_f} D\left[x_a(\tau)\right] \exp\left[\frac{i}{h} S_a(\gamma)\right] \\ &\approx \sum_{\{\gamma\}} \exp\left[\frac{i}{h} S_a(\gamma)\right] \end{aligned} \tag{49}$$

where K_a is the probability amplitude (fractal quantum mechanics) or the two point correlation function (statistical mechanics), $D\left[x_a(\tau)\right]$ means path integration on the sum $\{\gamma\}$ of fractal paths and $S_a(\gamma)$ is the fractal generalization of the action integral [13]:

$$S_a\left[\gamma\right] = \frac{1}{\Gamma(a)} \int_{x_i}^{x_f} L\left(D_\gamma^a q(\tau), \tau\right)(t-\tau)^{a-1} d\tau \tag{50}$$

2.6 The Highlights of Tsallis Theory

As we show in the next sections of this study, everywhere in space plasmas we can ascertain the presence of Tsallis statistics. This discovery is the continuation of a more general ascertainment of Tsallis q-extensive statistics from the macroscopic to the microscopic level [29].

In our understanding the Tsallis theory, more than a generalization of thermodynamics for chaotic and complex systems, or a non-equilibrium generalization of B-G statistics, can be considered as a strong theoretical vehicle for the unification of macroscopic and microscopic physical complexity. From this point of view Tsallis statistical theory is the other side of the modern fractal generalization of dynamics while its essence is nothing else than the efficiency of self-organization and development of long range correlations of coherent structures in complex systems.

From a general philosophical aspect, the Tsallis q-extension of statistics can be identified with the activity of an ordering principle in physical reality, which cannot be exhausted with the local interactions in the physical systems, as we noticed in previous sections.

2.6.1 The non-extensive entropy (S_q)

It was for first time that Tsallis [1], inspired by multifractal analysis, conceived that the Boltzmann – Gibbs entropy:

$$S_{BG} = -K\sum p_i \ln p_i \ , \ i = 1,2,...,N \tag{51}$$

is inefficient to describe all the complexity of non-linear dynamical systems. The Boltzmann – Gibbs statistical theory presupposes ergodicity of the underlying dynamics in the system phase space. The complexity of dynamics which is far beyond the simple ergodic complexity, it can be described by Tsallis non-extensive statistics, based on the extended concept of $q-$entropy:

$$S_q = k\left(1-\sum_{i=1}^{N} p_i^q\right) / \left(q-1\right) \tag{52}$$

for discrete state space or

$$S_q = k\left[1-\int\left[p(x)\right]^q dx\right] / \left(q-1\right) \tag{53}$$

for continuous state space.
For a system of particles and fields with short range correlations inside their immediate neighborhood, the Tsallis $q-$entropy S_q asymptotically leads to Boltzmann – Gibbs entropy (S_{BG}) corresponding to the value of $q=1$. For probabilistically dependent or correlated systems A,B it can be proven that:

$$\begin{aligned} S_q(A+B) &= S_q(A)+S_q(B/A)+(1-q)S_q(A)S_q(B/A) \\ &= S_q(B)+S_q(A/B)+(1-q)S_q(B)S_q(A/B) \end{aligned} \tag{54}$$

Where $S_q(A) \equiv S_q\left(\left\{p_i^A\right\}\right)$, $S_q(B) \equiv Sq\left(\left\{p_i^B\right\}\right)$, $S_q(B/A)$ and $S_q(A/B)$ are the conditional entropies of systems A,B [29]. When the systems are probabilistically independent, then relation (3.1.4) is transformed to:

$$S_q(A+B) = S_q(A)+S_q(B)+(1-q)S_q(A)S_q(B) \tag{55}$$

The dependent (independent) property corresponds to the relation:

$$p_{ij}^{A+B} \neq p_i^A p_j^B \left(p_{ij}^{A+B} = p_i^A p_j^B\right) \tag{56}$$

Comparing the Boltzmann – Gibbs (S_{BG}) and Tsallis (S_q) entropies, we conclude that for non-existence of correlations S_{BG} is extensive whereas S_q

for $q \neq 1$ is non-extensive. In contrast, for global correlations, large regions of phase – space remain unoccupied. In this case S_q is non-extensive either $q = 1$ or $q \neq 1$.

2.6.2 The $q-$ extension of statistics and Thermodynamics

Non-linearity can manifest its rich complex dynamics as the system is removed far from equilibrium. The Tsallis $q-$ extension of statistics is indicated by the non-linear differential equation $dy/dx = y^q$. The solution of this equation includes the $q-$ extension of exponential and logarithmic functions:

$$e_q^x = \left[1+(1-q)x\right]^{1/(1-q)} \tag{57}$$

$$\ln_q x = \left(x^{1-q}-1\right)/\left(1-q\right) \tag{58}$$

and

$$p_{opt}(x) = e_q^{-\beta_q[f(x)-F_q]} / \int dx' e_q^{-\beta_q[f(x')-F_q]} \tag{59}$$

for more general $q-$ constraints of the forms $\left\langle f(x) \right\rangle_q = F_q$. In this way, Tsallis $q-$ extension of statistical physics opened the road for the $q-$ extension of thermodynamics and general critical dynamical theory as a non-linear system lives far from thermodynamical equilibrium. For the generalization of Boltzmann-Gibbs nonequilibrium statistics to Tsallis nonequilibrium q-statistics we follow Binney [41]. In the next we present q-extended relations, which can describe the non-equilibrium fluctuations and $n-$ point correlation function (G) can be obtained by using the Tsallis partition function Z_q of the system as follows:

$$G_q^n(i_1, i_2, ..., i_n) \equiv \left\langle s_{i_1}, s_{i_2}, ..., s_{i_n} \right\rangle_q = \frac{1}{z} \frac{\partial^n Z_q}{\partial j_{i_1} \cdot \partial j_{i_2} ... \partial j_{i_n}} \tag{60}$$

Where $\{s_i\}$ are the dynamical variables and $\{j_i\}$ their sources included in the effective – Lagrangian of the system. Correlation (Green) equations (62) describe discrete variables, the $n-$ point correlations for continuous distribution of variables (random fields) are given by the functional derivatives of the functional partition as follows:

$$G_q^n(\vec{x}_1, \vec{x}_2, ..., \vec{x}_n) \equiv \left\langle \varphi(\vec{x}_1)\varphi(\vec{x}_2)...\varphi(\vec{x}_n) \right\rangle_q = \frac{1}{Z} \frac{\delta}{\delta J(\vec{x}_1)} \cdots \frac{\delta}{\delta J(\vec{x}_n)} Z_q(J) \tag{61}$$

where $\varphi(\vec{x})$ are random fields of the system variables and $j(\vec{x})$ their field sources. The connected $n-$ point correlation functions G_i^n are given by:

$$G_q^n(\vec{x}_1,\vec{x}_2,...,\vec{x}_n) \equiv \frac{\delta}{\delta J(\vec{x}_1)}...\frac{\delta}{\delta J(\vec{x}_n)}\log Z_q(J) \tag{62}$$

The connected $n-$point correlations correspond to correlations that are due to internal interactions defined as [41]:

$$G_q^n(\vec{x}_1,\vec{x}_2,...,\vec{x}_n) \equiv \left\langle \varphi(\vec{x}_1)...\varphi(\vec{x}_n)\right\rangle_q - \left\langle \varphi(x_1)...\varphi(x_n)\right\rangle_q \tag{63}$$

The probability of the microscopic dynamical configurations is given by the general relation:

$$P(conf) = e^{-\beta S_{conf}} \tag{64}$$

where $\beta = 1/kt$ and S_{conf} is the action of the system, while the partition function Z of the system is given by the relation:

$$Z = \sum_{conf} e^{-\beta S_{conf}} \tag{65}$$

The $q-$extension of the above statistical theory can be obtained by the $q-$partition function Z_q. The $q-$partition function is related with the meta-equilibrium distribution of the canonical ensemble which is given by the relation:

$$p_i = e_q^{-\beta q(E_i - V_q)/Z_q} \tag{66}$$

with

$$Z_q = \sum_{conf} e_q^{-\beta q(E_i - V_q)} \tag{67}$$

and

$$\beta_q = \beta / \sum_{conf} p_i^q \tag{68}$$

where $\beta = 1/KT$ is the Lagrange parameter associated with the energy constraint:

$$\left\langle E\right\rangle_q \equiv \sum_{conf} p_i^q E_i / \sum_{conf} p_i^q = U_q \tag{69}$$

The $q-$extension of thermodynamics is related with the estimation of $q-$Free energy (F_q) the $q-$expectation value of internal energy $\left(U_q\right)$ the $q-$specific heat $\left(C_q\right)$ by using the $q-$partition function:

$$F_q \equiv U_q - TS_q = -\frac{1}{\beta}\ln qZ_q \tag{70}$$

$$U_q = \frac{\partial}{\partial \beta} \ln q Z_q, \frac{1}{T} = \frac{\partial S_q}{\partial U_q} \tag{71}$$

$$C_q \equiv T \frac{\partial \delta_q}{\partial T} = \frac{\partial U_q}{\partial T} = -T \frac{\partial^2 F_q}{\partial T^2} \tag{72}$$

2.6.3 The Tsallis $q-$extension of statistics via the fractal extension of dynamics

At the equilibrium thermodynamical state the underlying statistical dynamics is Gaussian ($q=1$). As the system goes far from equilibrium the underlying statistical dynamics becomes non-Gaussian ($q \neq 1$). At the first case the phase space includes ergodic motion corresponding to normal diffusion process with mean-squared jump distances proportional to the time $\left\langle x^2 \right\rangle \sim t$ whereas far from equilibrium the phase space motion of the dynamics becomes chaotically self-organized corresponding to anomalous diffusion process with mean-squared jump distances $\left\langle x^2 \right\rangle \sim t^a$, with $a<1$ for sub-diffusion and $a>1$ for super-diffusion. The equilibrium normal-diffusion process is described by a chain equation of the Markov-type:

$$W\left(x_3,t_3;x_1,t_1\right) = \int dx_2 W\left(x_3,t_3;x_2,t_2\right) W\left(x_2,t_2;x_1,t_1\right) \tag{73}$$

where $W\left(x,t;x',t'\right)$ is the probability density for the motion from the dynamical state (x',t') to the state (x,t) of the phase space. The Markov process can be related to a random differential Langevin equation with additive white noise and a corresponding Fokker – Planck probabilistic equation [38] by using the initial condition:

$$\underset{\Delta t \to 0}{W}(x,y;\Delta t) = \delta(x-y) \tag{74}$$

This relation means no memory in the Markov process and help to obtain the expansion:

$$W\left(x,y;\Delta t\right) = \delta\left(x-y\right) + a\left(y;\Delta t\right)\delta'\left(x-y\right) + \frac{1}{2} b\left(y;\Delta t\right)\delta''\left(x-y\right) \tag{75}$$

where $A\left(y;\Delta t\right)$ and $B\left(y;\Delta t\right)$ are the first and second moment of the transfer probability function $W\left(x,y;\Delta t\right)$:

$$a\left(y;\Delta t\right) = \int dx(x-y)W(x,y;\Delta t) \equiv \left\langle \left\langle \Delta y \right\rangle \right\rangle \tag{76}$$

$$b(y;\Delta t)=\int dx(x-y)^2 W(x,y;\Delta t)\equiv\left\langle\left\langle(\Delta y)^2\right\rangle\right\rangle \tag{77}$$

By using the normalization condition:

$$\int dyW(x,y;\Delta t)=1 \tag{78}$$

we can obtain the relation:

$$a(y;\Delta t)=-\frac{1}{2}\frac{\partial b(y;\Delta t)}{\partial y} \tag{79}$$

The Fokker – Planck equation which corresponds to the Markov process can be obtained by using the relation:

$$\frac{\partial p(x,t)}{\partial t}=\lim_{\Delta t\to 0}\frac{1}{\Delta t}\left[\int_{-\infty}^{+\infty} dyW(x,y;\Delta t)p(y,t)-p(x,t)\right] \tag{80}$$

where $p(x,t)\equiv W(x,x_0;t)$ is the probability distribution function of the state (x,t) corresponding to large time asymptotic, as follows:

$$\frac{\partial P(x,t)}{\partial t}=-\nabla_x\left(AP(x,t)\right)+\frac{1}{2}\nabla_x^2\left(BP(x,t)\right) \tag{81}$$

where $A(x)$ is the flow coefficient:

$$A(x,t)\equiv\lim_{\Delta t\to 0}\frac{1}{\Delta t}\left\langle\left\langle\Delta x\right\rangle\right\rangle \tag{82}$$

and $B(x,t)$ is the diffusion coefficient:

$$B(\vec{x},t)\equiv\lim_{\Delta t\to 0}\frac{1}{\Delta t}\left\langle\left\langle\Delta x^2\right\rangle\right\rangle \tag{83}$$

The Markov process is a Gaussian process as the moments $\lim_{\Delta t\to 0}\left\langle\left\langle\Delta x^m\right\rangle\right\rangle$ for $m>2$ are zero [63]. The stationary solutions of F-P equation satisfy the extremal condition of Boltzmann – Gibbs entropy:

$$S_{BG}=-K_B\int p(x)\ln p(x)dx \tag{84}$$

corresponding to the known Gaussian distribution:

$$p(x)\sim\exp\left(-x^2/2\sigma^2\right) \tag{85}$$

According to Zaslavsky [38] the fractal extension of Fokker – Planck (F-P) equation can be produced by the scale invariance principle applied for the phase space of the non-equilibrium dynamics. As it was shown by Zaslavsky for strong chaos the phase space includes self similar structures of islands inside islands dived in the stochastic sea [38]. The fractal extension of the FPK equation (FFPK) can be derived after the application of a Renormalization group of anomalous kinetics (RGK):

$$\hat{R}_K : s' = \lambda_s S \ , \ t' = \lambda_t t$$

where s is a spatial variable and t is the time.
Correspondingly to the Markov process equations:

$$\frac{\partial^\beta p(\xi,t)}{\partial t^\beta} \equiv \lim_{\Delta t \to 0} \frac{1}{(\Delta t)^\beta} \left[W\left(\xi, \xi_0; t+\Delta t\right) - W\left(\xi, \xi_0; t\right) \right] \quad (86)$$

$$W(\xi,n;\Delta t) = \delta(\xi - n) + A(n;\Delta t)\delta^{(\alpha)}(\xi - n) + \frac{1}{2} B(n;\Delta t)\delta^{(2a)}(\xi - n) + ... \quad (87)$$

as the space-time variations of probability W are considered on fractal space-time variables (t,ξ) with dimensions (β, a).
For fractal dynamics $a(n;\Delta t)$, $b(n;\Delta t)$ satisfy the equations:

$$a(n;\Delta t) = \int \left| n - \xi \right|^\alpha W(\xi,n;\Delta t) d\xi \equiv \left\langle \left\langle \left| \Delta\xi \right|^a \right\rangle \right\rangle \quad (88)$$

$$b(n;\Delta t) = \int \left| n - \xi \right|^{2\alpha} W(\xi,n;\Delta t) d\xi \equiv \left\langle \left\langle \left| \Delta\xi \right|^{2a} \right\rangle \right\rangle \quad (89)$$

and the limit equations:

$$A(\xi) = \lim_{\Delta t \to 0} \frac{a(\xi;\Delta t)}{(\Delta t)^\beta} \quad (90)$$

$$B(\xi) = \lim_{\Delta t \to 0} \frac{b(\xi;\Delta t)}{(\Delta t)^\beta} \quad (91)$$

By them we can obtain the FFPK equation.
Far from equilibrium the non-linear dynamics can produce phase space topologies corresponding to various complex attractors of the dynamics. In this case the extended complexity of the dynamics corresponds to the generalized strange kinetic Langevin equation with correlated and multiplicative noise components and extended fractal Fokker – Planck - Kolmogorov equation (FFPK) [38, 80]. The $q-$extension of statistics by Tsallis can be related with the strange kinetics and the fractal extension of dynamics through the Levy process:

$$P\left(x_n, t_n; x_0 t_0\right) = \int dx_1 ... dx_{N-1} P\left(x_N, t_N; x_{N-1}, t_{N-1}\right) ... P\left(x_1, t_1; x_0, t_0\right) \quad (92)$$

The Levy process can be described by the fractal F-P equation:

$$\frac{\partial^\beta P(x,t)}{\partial t^\beta} = \frac{\partial^a}{\partial(-x)^a} \left[A(x) P(x,t) \right] + \frac{\partial^{a+1}}{\partial(-x)^{a+1}} \left[B(x) P(x,t) \right] \quad (93)$$

where $\partial^{\beta} / \partial t^{\beta}$, $\partial^{a} / \partial(-x)^{a}$ and $\partial^{a+1} / \partial(-x)^{a+1}$ are the fractal time and space derivatives correspondingly [38]. The stationary solution of the F F-P equation for large x is the Levy distribution $P(x) \sim x^{-(1+\gamma)}$. The Levy distribution coincides with the Tsallis $q-$extended optimum distribution (3.2.4) for $q = (3+\gamma)/(1+\gamma)$. The fractal extension of dynamics takes into account non-local effects caused by the topological heterogeneity and fractality of the self-organized phase – space. Also the fractal geometry and the complex topology of the phase – space introduce memory in the complex dynamics which can be manifested as creation of long range correlations, while, oppositely, in Markov process we have complete absence of memory.

In general, the fractal extension of dynamics as it was done until now from Zaslavsky, Tarasov and other scientists indicate the internal consistency of Tsallis $q-$statistics as the non-equilibrium extension of B-G statistics with the fractal extension of classical and quantum dynamics. Concerning the space plasmas the fractal character of their dynamics has been indicated also by many scientists. Indicatively, we refer the fractal properties of sunspots and their formation by fractal aggregates as it was shown by Zelenyi and Milovanov [30, 32], the anomalous diffusion and intermittent turbulence of the solar convection and photospheric motion shown by Ruzmakin et al. [33], the multi-fractal and multi-scale character of space plasmas indicated by Lui [46] and Pavlos et al. [37].

Finally we must notice the fact that the fractal extension of dynamics identifies the fractal distribution of a physical magnitude in space and time according to the scaling relation $M(R) \sim R^{a}$ with the fractional integration as an integration in a fractal space [12]. From this point of view it could be possible to conclude the novel concept that the non-equilibrium $q-$extension of statistics and the fractal extension of dynamics are related with the fractal space and time themselves [6, 39, 80].

2.6.4 Fractal acceleration and fractal energy dissipation

The problem of kinetic or magnetic energy dissipation in fluid and plasmas as well as the bursty acceleration processes of particles at flares, magnetospheric plasma sheet and other regions of space plasmas is an old and yet resisting problem of fluids or space plasma science.

Normal Gaussian diffusion process described by the Fokker – Planck equation is unable to explain either the intermittent turbulence in fluids or the bursty character of energetic particle acceleration following the bursty development of inductive electric fields after turbulent magnetic flux change in plasmas [81]. However the fractal extension of dynamics and Tsallis extension of statistics

indicate the possibility for a mechanism of fractal dissipation and fractal acceleration process in fluids and plasmas.
According to Tsallis statistics and fractal dynamics the super-diffusion process:

$$\langle R^2 \rangle \sim t^\gamma \tag{94}$$

with $\gamma > 1$ ($\gamma = 1$ for normal diffusion) can be developed at systems far from equilibrium. Such process is known as intermittent turbulence or as anomalous diffusion which can be caused by Levy flight process included in fractal dynamics and fractal Fokker – Planck Kolmogorov equation (FFPK). The solution of FFPK equation [38] corresponds to double (temporal, spatial) fractal characteristic function:

$$P(k,t) = \exp\left(-constxt^\beta \left|k\right| a\right) \tag{95}$$

Where $P\left(k,t\right)$ is the Fourier transform of asymptotic distribution function:

$$P(\xi,t) \sim constxt^\beta / \xi^{1+\alpha}, \; (\xi \to \infty) \tag{96}$$

This distribution is scale invariant with mean displacement:

$$\left\langle \left|\xi\right|^\alpha \right\rangle \sim constxt^\beta, \; (t \to \infty) \tag{97}$$

According to this description, the flights of multi-scale and multi-fractal profile can explain the intermittent turbulence of fluids, the bursty character of magnetic energy dissipation and the bursty character of induced electric fields and charged particle acceleration in space plasmas as well as the non-Gaussian dynamics of brain-heart dynamics. The fractal motion of charged particles across the fractal and intermittent topologies of magnetic – electric fields is the essence of strange kinetic [38, 80]. Strange kinetics permits the development of local sources with spatial fractal – intermittent condensation of induced electric-magnetic fields in brain, heart and plasmas parallely with fractal – intermittent dissipation of magnetic field energy in plasmas and fractal acceleration of charged particles. Such kinds of strange accelerators in plasmas can be understood by using the Zaslavsky studies for Hamiltonian chaos in anomalous multi-fractal and multi-scale topologies of phase space [38]. Generally the anomalous topology of phase space and fractional Hamiltonian dynamics correspond to dissipative non-Hamiltonian dynamics in the usual phase space [12]. The most important character of fractal kinetics is the wandering of the dynamical state through the gaps of cantori which creates effective barriers for diffusion and long range Levy flights in trapping regions of the phase space. Similar Levy flights processes can be developed by the fractal dynamics and intermittent turbulence of the complex systems.

In this theoretical framework it is expected the existence of Tsallis non extensive entropy and q-statistics in non-equilibrium distributed complex systems as, fluids, plasmas or brain and heart systems which are studied in the next section of this work. The fractal dynamics corresponding to the non-extensive Tsallis $q-$statistical character of the probability distributions in the distributed complex systems indicate the development of a self-organized and globally correlated parts of active regions in the distributed dynamics. This character can be related also with deterministic low dimensional chaotic profile of the active regions according to Pavlos et al. [37,].

3. Theoretical expectations through Tsallis statistical theory and fractal dynamics

Tsallis $q-$statistics as well as the non-equilibrium fractal dynamics indicate the multi-scale, multi-fractal chaotic and holistic dynamics of space plasmas. Before we present experimental verification of the theoretical concepts described in previous studies as concerns space plasmas in this section we summarize the most significant theoretical expectations.

3.1 The $q-$triplet of Tsallis

The non-extensive statistical theory is based mathematically on the nonlinear equation:

$$\frac{dy}{dx} = y^q \text{ , } (y(0) = 1, q \in \Re) \tag{98}$$

with solution the $q-$exponential function defined previously in equation (2.2). The solution of this equation can be realized in three distinct ways included in the $q-$triplet of Tsallis: ($q_{sen}, q_{stat}, q_{rel}$). These quantities characterize three physical processes which are summarized here, while the $q-$triplet values characterize the attractor set of the dynamics in the phase space of the dynamics and they can change when the dynamics of the system is attracted to another attractor set of the phase space. The equation (2.36) for $q=1$ corresponds to the case of equilibrium Gaussian Boltzmann-Gibbs (BG) world [35, 36]. In this case of equilibrium BG world the $q-$triplet of Tsallis is simplified to ($q_{sen}=1, q_{stat}=1, q_{rel}=1$).

a. The q_{stat} index and the non-extensive physical states

According to [35, 36] the long range correlated metaequilibrium non-extensive physical process can be described by the nonlinear differential equation:

$$\frac{d(p_i Z_{stat})}{dE_i} = -\beta q_{stat} (p_i Z_{stat})^{q_{stat}} \tag{99}$$

The solution of this equation corresponds to the probability distribution:

$$p_i = e_{q_{stat}}^{-\beta_{stat} E_i} / Z_{q_{stat}} \tag{100}$$

where $\beta_{q_{stat}} = \dfrac{1}{KT_{stat}}$, $Z_{stat} = \sum_j e_{q_{stat}}^{-\beta q_{stat} E_j}$.

Then the probability distribution function is given by the relations:

$$p_i \propto \left[1-(1-q)\beta_{q_{stat}} E_i\right]^{1/1-q_{stat}} \tag{101}$$

for discrete energy states $\{E_i\}$ by the relation:

$$p(x) \propto \left[1-(1-q)\beta_{q_{stat}} x^2\right]^{1/1-q_{stat}} \tag{102}$$

for continuous X states $\{X\}$, where the values of the magnitude X correspond to the state points of the phase space.

The above distributions functions (2.46, 2.47) correspond to the attracting stationary solution of the extended (anomalous) diffusion equation related with the nonlinear dynamics of system [36]. The stationary solutions $P(x)$ describe the probabilistic character of the dynamics on the attractor set of the phase space. The non-equilibrium dynamics can be evolved on distinct attractor sets depending upon the control parameters values, while the q_{stat} exponent can change as the attractor set of the dynamics changes.

b. The q_{sen} index and the entropy production process

The entropy production process is related to the general profile of the attractor set of the dynamics. The profile of the attractor can be described by its multifractality as well as by its sensitivity to initial conditions. The sensitivity to initial conditions can be described as follows:

$$\frac{d\xi}{d\tau} = \lambda_1 \xi + (\lambda_q - \lambda_1)\xi^q \tag{103}$$

where ξ describes the deviation of trajectories in the phase space by the relation: $\xi \equiv \lim_{\Delta(x)\to 0}\{\Delta x(t) \setminus \Delta x(0)\}$ and $\Delta x(t)$ is the distance of neighboring trajectories [82]. The solution of equation (2.41) is given by:

$$\xi = \left[1 - \frac{\lambda q_{sen}}{\lambda_1} + \frac{\lambda q_{sen}}{\lambda_1} e^{(1-q_{sen})\lambda_1 t}\right]^{\frac{1}{1-q}} \tag{104}$$

The q_{sen} exponent can be also related with the multifractal profile of the attractor set by the relation:

$$\frac{1}{q_{sen}} = \frac{1}{a_{\min}} - \frac{1}{a_{\max}} \tag{105}$$

where $a_{\min}(a_{\max})$ corresponds to the zero points of the multifractal exponent spectrum $f(a)$ [36, 79, 82]. That is $f(a_{\min}) = f(a_{\max}) = 0$.
The deviations of neighboring trajectories as well as the multifractal character of the dynamical attractor set in the system phase space are related to the chaotic phenomenon of entropy production according to Kolmogorov – Sinai entropy production theory and the Pesin theorem [36]. The $q-$entropy production is summarized in the equation:

$$K_q \equiv \lim_{t\to\infty} \lim_{W\to\infty} \lim_{N\to\infty} \frac{< S_q > (t)}{t}. \tag{106}$$

The entropy production (dS_q / t) is identified with K_q, as W are the number of non-overlapping little windows in phase space and N the state points in the windows according to the relation $\sum_{i=1}^{W} N_i = N$. The S_q entropy is estimated by the probabilities $P_i(t) \equiv N_i(t) / N$. According to Tsallis the entropy production K_q is finite only for $q = q_{sen}$ [36, 82].

c. The q_{rel} index and the relaxation process

The thermodynamical fluctuation – dissipation theory [63] is based on the Einstein original diffusion theory (Brownian motion theory). Diffusion process is the physical mechanism for extremization of entropy. If ΔS denote the deviation of entropy from its equilibrium value S_0, then the probability of the proposed fluctuation that may occur is given by:

$$P \sim \exp(\Delta s / k). \tag{107}$$

The Einstein – Smoluchowski theory of Brownian motion was extended to the general Fokker – Planck diffusion theory of non-equilibrium processes. The potential of Fokker – Planck equation may include many metaequilibrium stationary states near or far away from the basic thermodynamical equilibrium state. Macroscopically, the relaxation to the equilibrium stationary state can be described by the form of general equation as follows:

$$\frac{d\Omega}{d\tau} \sim -\frac{1}{\tau}\Omega, \tag{108}$$

where $\Omega(t) \equiv [O(t) - O(\infty)] / [O(0) - O(\infty)]$ describes the relaxation of the macroscopic observable $O(t)$ relaxing towards its stationary state value. The non-extensive generalization of fluctuation – dissipation theory is related to the general correlated anomalous diffusion processes [36]. Now, the equilibrium relaxation process (2.46) is transformed to the metaequilibrium non-extensive relaxation process:

$$\frac{d\Omega}{dt} = -\frac{1}{T_{q_{rel}}}\Omega^{q_{rel}} \tag{109}$$

the solution of this equation is given by:

$$\Omega(t) \sim e_{q_{rel}}^{-t/\tau_{rel}} \tag{110}$$

The autocorrelation function $C(t)$ or the mutual information $I(t)$ can be used as candidate observables $\Omega(t)$ for the estimation of q_{rel}. However, in contrast to the linear profile of the correlation function, the mutual information includes the non linearity of the underlying dynamics and it is proposed as a more faithful index of the relaxation process and the estimation of the Tsallis exponent q_{rel}.

3.2 Measures of Multifractal Intermittence Turbulence

In the following, we follow Arimitsu and Arimitsu [78] for the theoretical estimation of significant quantitative relations which can also be estimated experimentally. The probability singularity distribution $P(a)$ can be estimated as extremizing the Tsallis entropy functional S_q. According to Arimitsu and Arimitsu [78] the extremizing probability density function $P(a)$ is given as a $q-$exponential function:

$$P(a) = Z_q^{-1}[1-(1-q)\frac{(a-a_0)^2}{2X/\ln 2}]^{\frac{1}{1-q}} \tag{111}$$

where the partition function Z_q is given by the relation:

$$Z_q = \sqrt{2X/[(1-q)\ln 2]}\ B(1/2, 2/1-q), \tag{112}$$

and $B(a,b)$ is the Beta function. The partition function Z_q as well as the quantities X and q can be estimated by using the following equations:

$$\left.\begin{aligned} \sqrt{2X} &= \left[\sqrt{a_0^2+(1-q)^2}-(1-q)\right]/\sqrt{b} \\ b &= (1-2^{-(1-q)})/[(1-q)\ln_2] \end{aligned}\right\} \tag{113}$$

We can conclude for the exponent's spectrum $f(a)$ by using the relation $P(a) \approx \ln^{d-F(a)}$ as follows:

$$f(a)=D_0+\log_2[1-(1-q)\frac{(a-a_o)^2}{2X/\ln 2}]/(1-q)^{-1} \quad (114)$$

where a_0 corresponds to the $q-$expectation (mean) value of a through the relation:

$$<(a-a_0)^2>_q=(\int daP(a)^q(a-a_0)^q)/\int daP(a)^q \,. \quad (115)$$

while the $q-$expectation value a_0 corresponds to the maximum of the function $f(a)$ as $df(a)/da\,|\,a_0=0$. For the Gaussian dynamics ($q\to 1$) we have mono-fractal spectrum $f(a_0)=D_0$. The mass exponent $\tau(\overline{q})$ can be also estimated by using the inverse Legendre transformation: $\tau(\overline{q})=a\overline{q}-f(a)$ (relations 2.24 – 2.25) and the relation (2.29) as follows:

$$\tau(\overline{q})=\overline{q}a_0-1-\frac{2X\overline{q}^2}{1+\sqrt{C_{\overline{q}}}}-\frac{1}{1-q}[1-\log_2(1+\sqrt{C_{\overline{q}}})], \quad (116)$$

Where $C_{\overline{q}}=1+2\overline{q}^2(1-q)X\ln 2$.

The relation between a and q can be found by solving the Legendre transformation equation $\overline{q}=df(a)/da$. Also if we use the equation (2.29) we can obtain the relation:

$$a_{\overline{q}}-a_0=(1-\sqrt{C_{\overline{q}}})/[\overline{q}(1-q)\ln 2] \quad (117)$$

The $q-$index is related to the scaling transformations (2.20) of the multifractal nature of turbulence according to the relation $q=1-a$. Arimitsu and Arimitsu [78] estimated the $q-$index by analyzing the fully developed turbulence state in terms of Tsallis statistics as follows:

$$\frac{1}{1-q}=\frac{1}{a_-}-\frac{1}{a_+} \quad (118)$$

where $a_\pm$ satisfy the equation $f(a_\pm)=0$ of the multifractal exponents spectrum $f(a)$. This relation can be used for the estimation of $q_{sen}-$index included in the Tsallis $q-$triplet (see next section).

The above analysis based at the extremization of Tsallis entropy can be also used for the theoretical estimation of the structure functions scaling exponent spectrum $J(p)$ of the $S_p(\tau)$, where $p=1,2,3,4,\ldots$ The structure functions were first introduced by Kolmogorov [79] defined as statistical moments of the field increments:

$$S_p(\overrightarrow{r})=<|u(\vec{x}+\vec{d})-u(\vec{x})|^p>=<|\delta u_n|^p> \quad (119)$$

$$S_p(\vec{r}) =<| u(\vec{x}+\Delta\vec{x}) - u(\vec{x}) |^p > \qquad (120)$$

After discretization of $\Delta\vec{x}$ displacement the above relation can be identified to:

$$Sp(l^{\mathrm{n}}) =<| \delta u_n |^p > \qquad (121)$$

The field values $u(\vec{x})$ can be related with the energy dissipation values ε_n by the general relation $\varepsilon_n = (\delta u_n)^3 / l^{\mathrm{n}}$ in order to obtain the structure functions as follows:

$$S_p(l^{\mathrm{n}}) =< (\varepsilon_n/\varepsilon_0)^p >=< \delta_n^{p(a-1)} >= \delta_n^{j(p)} \qquad (122)$$

where the averaging processes $<\ldots>$ is defined by using the probability function $P(a)da$ as $<\ldots>= \int da(\ldots)P(a)$. By this, the scaling exponent $J(p)$ of the structure functions is given by the relation:

$$J(p) = 1 + \tau(\overline{q} = \frac{p}{3}) \qquad (123)$$

By following Arimitsu [78] the relation (2.30) leads to the theoretical prediction of $J(p)$ after extremization of Tsallis entropy as follows:

$$J(p) = \frac{a_0 p}{3} - \frac{2Xp^2}{q(1+\sqrt{C_{p/3}}} - \frac{1}{1-q}[1-\log_2(1+\sqrt{C_{p/3}})] \qquad (124)$$

The first term $a_0 p/3$ corresponds to the original of known Kolmogorov theory (K41) according to which the dissipation of field energy ε_n is identified with the mean value ε_0 according to the Gaussian self-similar homogeneous turbulence dissipation concept, while $a_0 = 1$ according to the previous analysis for homogeneous turbulence. According to this concept the multifractal spectrum consists of a single point. The next terms after the first in the relation (2.39) correspond to the multifractal structure of intermittence turbulence indicating that the turbulent state is not homogeneous across spatial scales. That is, there is a greater spatial concentration of turbulent activity at smaller than at larger scales. According to Abramenko [36] the intermittent multifractal (inhomogeneous) turbulence is indicated by the general scaling exponent $J(p)$ of the structure functions according to the relation:

$$J(p) = \frac{p}{3} + T^{(u)}(p) + T^{(F)}(p), \qquad (125)$$

where the $T^{(u)}(p)$ term is related with the dissipation of kinetic energy and the $T^{(F)}(p)$ term is related to other forms of field's energy dissipation as the magnetic energy at MHD turbulence [36, 83] .

The scaling exponent spectrum $J(p)$ can be also used for the estimation of the intermittency exponent μ according to the relation:

$$S(2) \equiv < \varepsilon^2 / \varepsilon > \sim \delta_n^{\mu} = \delta_n^{J(2)} \tag{127}$$

from which we conclude that $\mu = J(2)$. The intermittency turbulence correction to the law $P(f) \sim f^{-5/3}$ of the energy spectrum of Kolmogorov's theory is given by using the intermittency exponent:

$$P(f) \sim f^{-(5/3+\mu)} \tag{128}$$

The previous theoretical description can be used for the theoretical interpretation of the experimentally estimated structure function, as well as for relating physically the results of data analysis with Tsallis statistical theory, as it is described in the next sections.

4. Comparison of theory with the observations

4.1 The Tsallis q-statistics

The traditional scientific point of view is the priority of dynamics over statistics. That is dynamics creates statistics. However for complex system their holistic behaviour does not permit easily such a simplification and division of dynamics and statistics. Tsallis $q-$statistics and fractal or strange kinetics are two faces of the same complex and holistic (non-reductionist) reality. As Tsallis statistics is an extension of B-G statistics, we can support that the thermic and the dynamical character of a complex system is the manifestation of the same physical process which creates extremized thermic states (extremization of Tsallis entropy), as well as dynamically ordered states. From this point of view the Feynman path integral formulation of physical theory [84] indicates the indivisible thermic and dynamical character of physical reality. After this general investment in the following, we present evidence of Tsallis non-extensive $q-$statistics for space plasmas. The Tsallis statistics in relation with fractal and chaotic dynamics of space plasmas will be presented in a short coming series of publications.

In next sections we present estimations of Tsallis statistics for various kinds of space plasma's systems. The q_{stat} Tsallis index was estimated by using the observed Probability Distribution Functions (PDF) according to the Tsallis q-exponential distribution:

$$PDF\left[\Delta Z\right] \equiv A_q \left[1 + (q-1)\beta_q (\Delta Z)^2\right]^{\frac{1}{1-q}}, \tag{129}$$

where the coefficients A_q, β_q denote the normalization constants and $q \equiv q_{stat}$ is the entropic or non-extensivity factor ($q_{stat} \leq 3$) related to the size of the tail in the distributions. Our statistical analysis is based on the algorithm described in [56]. We construct the $PDF\left[\Delta Z\right]$ which is associated to the first difference $\Delta Z = Z_{n+1} - Z_n$ of the experimental sunspot time series, while the ΔZ range is subdivided into little ``cells'' (data binning process) of width δz, centered at z_i so that one can assess the frequency of Δz -values that fall within each cell/bin. The selection of the cell-size δz is a crucial step of the algorithmic process and its equivalent to solving the binning problem: a proper initialization of the bins/cells can speed up the statistical analysis of the data set and lead to a convergence of the algorithmic process towards the exact solution. The resultant histogram is being properly normalized and the estimated q-value corresponds to the best linear fitting to the graph $\ln_q(p(z_i))\ vs\ z_i^2$. Our algorithm estimates for each $\delta_q = 0{,}01$ step the linear adjustment on the graph under scrutiny (in this case the $\ln_q(p(z_i))\ vs\ z_i^2$ graph) by evaluating the associated correlation coefficient *(CC)*, while the best linear fit is considered to be the one maximizing the correlation coefficient. The obtained q_{stat}, corresponding to the best linear adjustment is then being used to compute the following equation:

$$G_q(\beta, z) = \frac{\sqrt{\beta}}{C_q} e_q^{-\beta z^2} \tag{130}$$

where $C_q = \sqrt{\pi} \cdot \Gamma(\frac{3-q}{2(q-1)}) / \sqrt{q-1} \cdot \Gamma(\frac{1}{q-1})$, $1 < q < 3$ for different *β*-values. Moreover, we select the *β*-value minimizing the $\sum_i [G_{q_{sstat}}(\beta, z_i) - p(z_i)]^2$, as proposed again in [56].

In the following we present the estimation of Tsallis statistics q_{stat} for various cases of space plasma system. Especially, we study the $q-$statistics for the following space plasma complex systems: I Magnetospheric system, II Solar Wind (magnetic cloud), III Solar activity, IV Cosmic stars, IIV Cosmic Rays.

4.2 Cardiac Dynamics

For the study of the q-statistics we used measurements from the cardiac and especially the heart rate variability timeseries which includes a multivariate data set recorded from a patient in the sleep laboratory of the Beth Israel Hospital in Boston, Massachusetts. The heart rate was determined by measuring the time between the QRS complexes in the electrocardiogram, taking the inverse, and then converting this to an evenly sampled record by interpolation. They were converted from 250 Hz to 2 Hz data by averaging over a 0.08 second window at the times of the heart rate samples.

Figure 1a presents the experimental time series, while Fig.1b presents the q-Gaussian functions G_q, corresponding to the time series under scrunity. The q-Gaussian function presents the best fitting of the experimental distribution function $P(z)$ estimated for the value $q_{stat} = 1.26 \pm 0.1$ for the stationary heart variability time series. The q-value was estimated by the linear correlation fitting between $\ln_q P(z_i)$ and $(z_i)^2$, shown in fig. 1c, were $P(z)$ corresponds to the experimental distribution functions, according to the description in section 4.1. The fact that the heart's variability observations obey to non-extensive Tsallis with a $q-$values higher than the Gaussian case ($q = 1$) permit to conclude for the heart's variability dynamics case the existence of q-statistics .

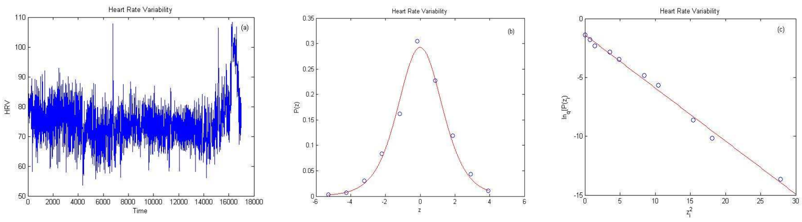

Figure 1: (a) Time series of heart rate variability **(b)** PDF $P(z_i)$ vs. z_i q Guassian function that fits $P(z_i)$ for the heart rate variability **(c)** Linear Correlation between $\ln_q P(z_i)$ and $(z_i)^2$ where q = 1.26 ± 0.10 for the heart rate variability.

4.3 Brain Epilepsy Dynamics

In this section we present the q-statistics obtained from real EEG timeseries from epileptic patients during seizure attack. Each EEG timeseries consisting of 3.750 points. The width of the timeseries is ranging from -1,000 Volt to 1,000 Volt.

In Figure 2a the experimental time series during the epilepsy is presented. The q-value was found to be $q_{stat} = 1.64 \pm 0.14$. The results of the q-statistics analysis are shown in Figure 2b and Figure 2c.

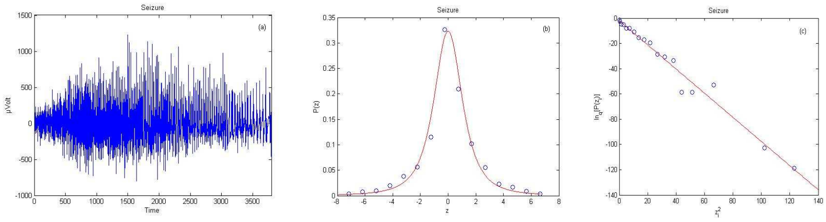

Figure 2: **(a)** Time series of seizure state **(b)** PDF $P(z_i)$ vs. z_i q Guassian function that fits $P(z_i)$ for the seizure state **(c)** Linear Correlation between $\ln_q P(z_i)$ and $(z_i)^2$ where q = 1.63 ± 0.14 for the seizure state.

4.4 Eartquakes Dynamics

In this sub-section we present the q-statistics of the experimental data from earthquakes in the region of whole Greece with magnitude greater from 4 and time period 1964-2004. The data set was found from the National Observatory of Athens (NOA).

In Figure 3a the time series of Interevent Times is presented, while the corresponding q-value is shown in Figure 3b and was found to be $q_{stat} = 2.28 \pm 0.12$. In Figure 3d we present the experimental time series of Magnitude data. The q-statistics for this case are presented in Figure 3e. The corresponding q-value was found to be $q_{stat} = 1.77 \pm 0.09$. The results reveal clearly non-Gaussian statistics for the earthquake Interevent Times and Magnitude data. The results showed the existence of q-statistics and the non-Gaussianity of the data sets.

4.5 Atmospheric Dynamics

In this sub-section we study the q-statistics for the air temperature and rain fall experimental data sets from the weather station 20046 Polar GMO in E.T. Krenkelja for the period 1/1/1960 – 31/12/1960. In Figure 4(a,d) the experimental time series from temperature and rainfall correspondingly are presented and in the Figure 4(b,c,e,f) the results of the q-statistics analysis are shown. The estimated q-values were found to be for the temperature data set and for the rainfall data set. In both cases we observed clearly non Gaussian statistics.

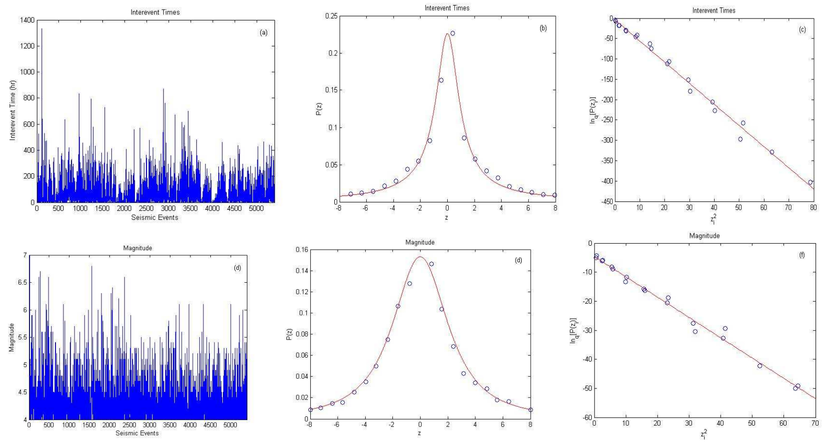

Figure 3: (a) Time series of Interevent Times **(b)** PDF $P(z_i)$ vs. z_i q Guassian function that fits $P(z_i)$ for the Interevent Times **(c)** Linear Correlation between $\ln_q P(z_i)$ and $(z_i)^2$ where q = 2.28 ± 0.12 for the Interevent Times **(d)** Time series of Magnitude **(e)** PDF $P(z_i)$ vs. z_i q Gaussian function that fits $P(z_i)$ for the Magnitude **(f)** Linear Correlation between $\ln_q P(z_i)$ and $(z_i)^2$ where q = 1.77 ± 0.09 for the Magnitude.

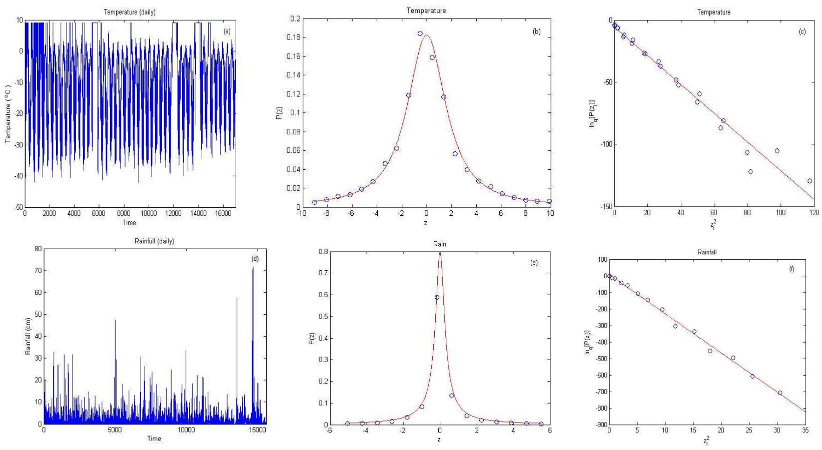

Figure 4: (a) Time series of Temperature **(b)** PDF $P(z_i)$ vs. z_i q Guassian function that fits $P(z_i)$ for the Temperature **(c)** Linear Correlation between $\ln_q P(z_i)$ and $(z_i)^2$ where q = 1.89 ± 0.08 for the Temperature **(d)** Time series of Rainfall **(e)** PDF $P(z_i)$ vs. z_i q Gaussian function that fits $P(z_i)$ for the Rainfall **(f)** Linear Correlation between $\ln_q P(z_i)$ and $(z_i)^2$ where q = 2.21 ± 0.06 for the Rainfall.

4.6 Magnetospheric Magneto Hydro Dynamics (MHD) Dynamics

The estimation of V_x, B_z Tsallis statistics during the substorm period is presented in fig.5(a-f). Fig. 2(a,d) shows the experimental time series corresponding to spacecraft observations of bulk plasma flows V_x and magnetic field B_z component. Fig. 2(b,e) presents the estimated q-values for the V_x plasma velocity time series and for the magnetic field B_z component time series. The q-values of the signals under scrutiny were found to be $q_{stat} = 1.98 \pm 0.06$ for the V_x plasma velocity time series and $q_{stat} = 2.05 \pm 0.04$ for the magnetic field B_z component. The fact that the magnetic field and plasma flow observations obey to non-extensive Tsallis with $q-$values much higher than the Gaussian case ($q = 1$) permit to conclude for magnetospheric plasma the existence of non-equilibrium MHD anomalous diffusion process.

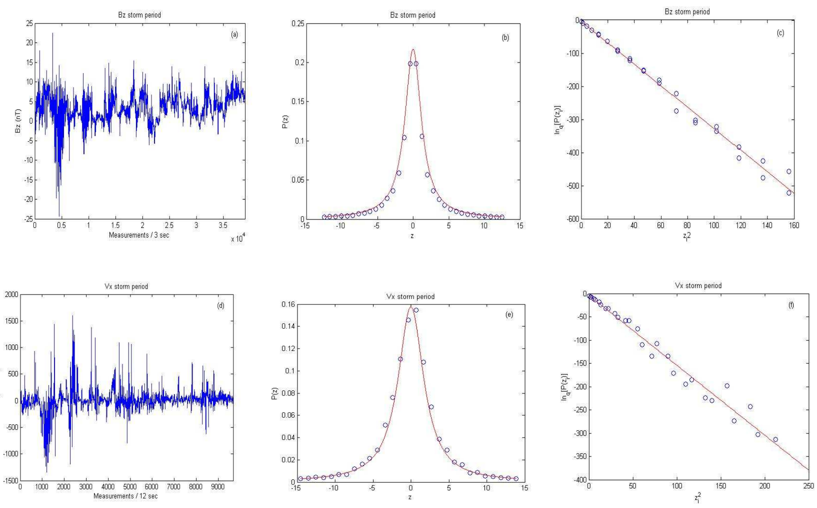

Figure 5: (a) Time series of Bz storm period **(b)** PDF $P(z_i)$ vs. z_i q Gaussian function that fits $P(z_i)$ for the Bz storm period **(c)** Linear Correlation between $\ln_q P(z_i)$ and $(z_i)^2$ where q = 2.05 ± 0.04 for the Bz storm period **(d)** Time series of Vx storm period **(e)** PDF $P(z_i)$ vs. z_i q Guassian function that fits $P(z_i)$ for the Vx storm period **(f)** Linear Correlation between $\ln_q P(z_i)$ and $(z_i)^2$ where q = 1.98 ± 0.06 for the Vx storm period.

4.7 Magnetospheric Fractal Accelerator of Charged Particles

Already Tsallis theory has been used for the study of magnetospheric energetic particles non-Gaussian by Voros [61] and Leubner [62]. In the following we study the q-statistics of magnetospheric energetic particle during a strong sub-storm period. We used the data set from the GEOTAIL/EPIC experiment during the period from 12:00 UT to 21:00 UT of 8/2/1997 and from 12:00 UT of 9/2/1997 to 12:00 UT of 10/2/1997. The Tsallis statistics estimated for the magnetospheric electric field and the magnetospheric particles $\left(e^-, p^+\right)$ during the storm period is shown in Fig. 6(a-i). Fig. 6(a,d,g) present the spacecraft observations of the magnetospheric electric field E_y component and the magnetospheric electrons $\left(e^-\right)$ and protons $\left(p^+\right)$. The corresponding Tsallis q-statistics was found to correspond to the q-values: $q_{stat} = 2.49 \pm 0.07$ for the E_y electric field component, $q_{stat} = 2.15 \pm 0.07$ for the energetic electrons and $q_{stat} = 2.49 \pm 0.05$ for the energetic protons. These values reveal clearly non-Gaussian dynamics for the mechanism of electric field development and electrons-protons acceleration during the magnetospheric storm period.

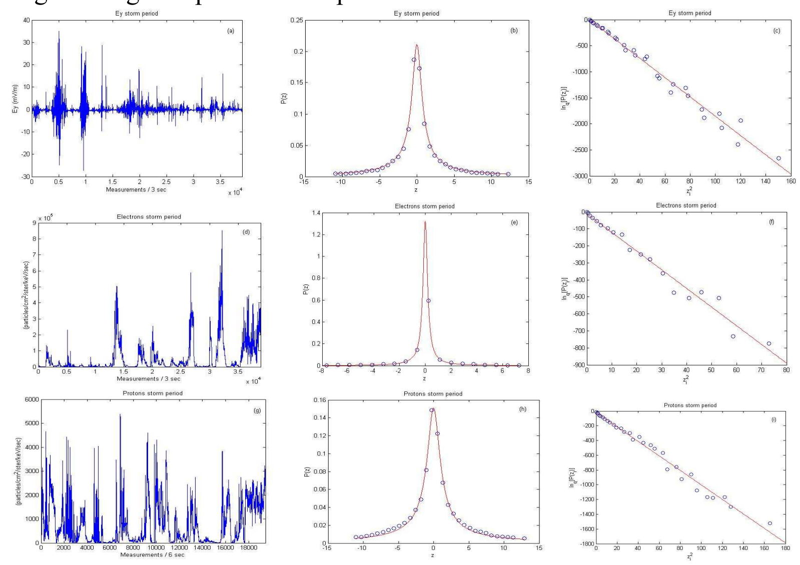

Figure 6: (a) Time series of Ey storm period **(b)** PDF $P(z_i)$ vs. z_i q Guassian function that fits $P(z_i)$ for the Ey storm period **(c)** Linear Correlation between $\ln_q P(z_i)$ and $(z_i)^2$ where q = 2.49 ± 0.07 for the Ey storm period **(d)** Time series of electrons storm period **(e)** PDF $P(z_i)$ vs. z_i q Gaussian function that fits $P(z_i)$ for the electrons storm period **(f)** Linear Correlation between $\ln_q P(z_i)$ and $(z_i)^2$ where q = 2.15 ± 0.07 for the electrons storm period time series **(g)** Time series of protons storm period **(h)** PDF $P(z_i)$ vs. z_i q Gaussian function that fits $P(z_i)$

for the protons storm period **(i)** Linear Correlation between $\ln_q P(z_i)$ and $(z_i)^2$ where q = 2.49 ± 0.05 for the protons storm period.

4.8 Solar Wind Magnetic Cloud

From the spacecraft ACE, magnetic field experiment (MAG) we take raw data and focus on the Bz magnetic field component with a sampling rate 3 sec. Tha data correspond to sub-storm period with time zone from 07:27 UT, 20/11/2001 until 03:00 UT, 21/11/2003.

Magnetic clouds are a possible manifestation of a Coronal Mass Ejection (CME) and they represent on third of ejectra observed by satellites. Magnetic cloud behave like a magnetosphere moving through the solar wind. Carbone et al. [58], de Wit [63] estimated non-Gaussian turbulence profile of solar wind. Bourlaga and Vinas [55] estimated the q-statistics of solar wind at the q-value $q_{stat} = 1.75 \pm 0.06$. Fig. 7 presents the q-statistics estimated in the magnetic cloud solar plasma for the z-component B_Z of the magnetic field. The B_Z time series is shown in Fig. 7a. The q-statistics for B_Z component is shown at Fig. 7(b,c), while the q-value was found to be $q_{stat} = 2.02 \pm 0.04$. This value is higher than the value $q_{stat} = 1.75$ estimated from Bourlaga and Vinas [55] at 40 AU.

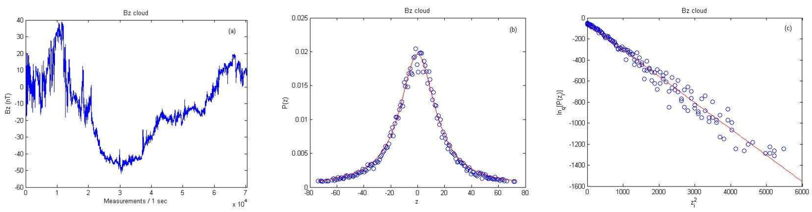

Figure 7: (a) Time series of Bz cloud **(b)** PDF $P(z_i)$ vs. z_i q Gaussian function that fits $P(z_i)$ for the Bz cloud **(c)** Linear Correlation between $\ln_q P(z_i)$ and $(z_i)^2$ where q = 2.02 ± 0.04 for the Bz cloud.

4.9 Solar Activity: Sun Spot-Flares Dynamics

In this sub-section we present the q-statistics of the sunspot and solar flares complex systems by using data of Wolf number and daily Flare Index. Especially, we use the Wolf number, known as the international sunspot number measures the number of sunspots and group of sunspots on the surface of the sun computed by the formula: (10)*R=k*(10g+s)* where: *s* is the number of individual spots, *g* is the number of sunspot groups and *k* is a factor that varies with location known as the observatory factor. We analyse a period of 184 years. Moreover we analyse the daily Flare Index of the solar activity that was determined using the final grouped solar flares obtained by NGDC (National Geophysical Data Center). It is calculated for each flare using the formula: $Q = (i * t)$, where "i" is the importance coefficient of the flare and "t" is the duration of the flare in minutes. To obtain final daily values, the daily sums of the index for the total surface are divided by the total time of observation of that day. The data covers time period from 1/1/1996 to 31/12/2007.

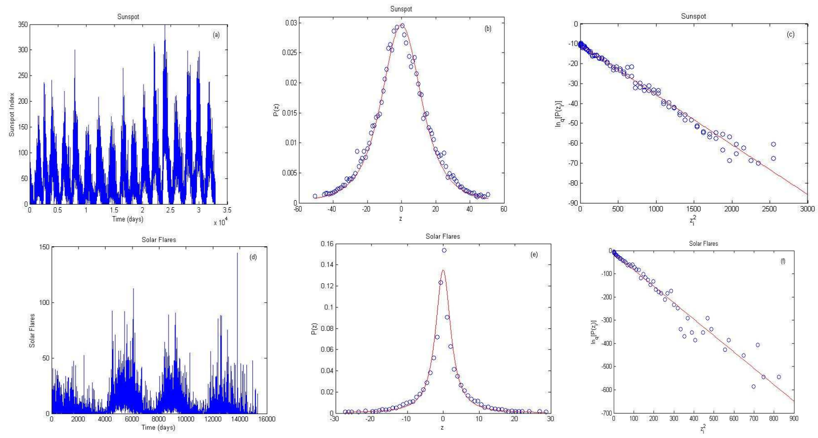

Figure 8: **(a)** Time series of Sunspot Index concerning the period of 184 years **(b)** PDF $P(z_i)$ vs. z_i q Guassian function that fits $P(z_i)$ for the Sunspot Index **(c)** Linear Correlation between $\ln_q P(z_i)$ and $(z_i)^2$ where q = 1.53 ± 0.04 for the Sunspot Index **(d)** Time series of Solar Flares concerning the period of 184 years **(e)** PDF $P(z_i)$ vs. z_i q Guassian function that fits $P(z_i)$ for the Solar Flares **(f)** Linear Correlation between $\ln_q P(z_i)$ and $(z_i)^2$ where q = 1.90 ± 0.05 for the Solar Flares.

Although solar flares dynamics is coupled to the sunspot dynamics. Karakatsanis and Pavlos [64] and Karakatsanis et al. [64] have shown that the dynamics of solar flares can be discriminated from the sunspot dynamics. Fig. 8 presents the estimation of q-statistics of sunspot index shown in fig. 8(b,c) and the q-statistics of solar flares signal shown in fig. 8(e,g). The q-values for the sunspot index and the solar flares time series were found to be $q_{stat} = 1.53 \pm 0.04$ and $q_{stat} = 1.90 \pm 0.05$ correspondingly. We clearly observe non-Gaussian statistics for both cases but the non-Gaussianity of solar flares was found much stronger than the sunspot index.

4.10 Solar Flares Fractal Accelerator

At solar flare regions the dissipated magnetic energy creates strong electric fields according to the theoretical concepts. The bursty character of the electric field creates burst of solar energetic particles through a mechanism of solar flare fractal acceleration. According to theoretical concept presented in previous section the fractal acceleration of energetic particles can be concluded by the Tsallis q-extenstion of statistics for non-equilibrium complex states. In the following we present significants verification of this theoretical prediction of Tsallis theory by study the q-statistics of energetic particle acceleration. Finally we analyze energetic particles from spacecraft ACE – experiment EPAM and time zone 1997 day 226 to 2006 day 178 and protons (0.5 – 4) MeV with period 20/6/1986 – 31/5/2006, spacecraft GOES, hourly averaged data. Figure 9 presents the estimation of the solar protons - electrons q-statistics. The q-values for solar energetic protons and electrons time series were found to be $q_{stat} = 2.31 \pm 0.13$ and $q_{stat} = 2.13 \pm 0.06$ correspondingly. Also in this case we clearly observe non-Gaussian statistics for both cases.

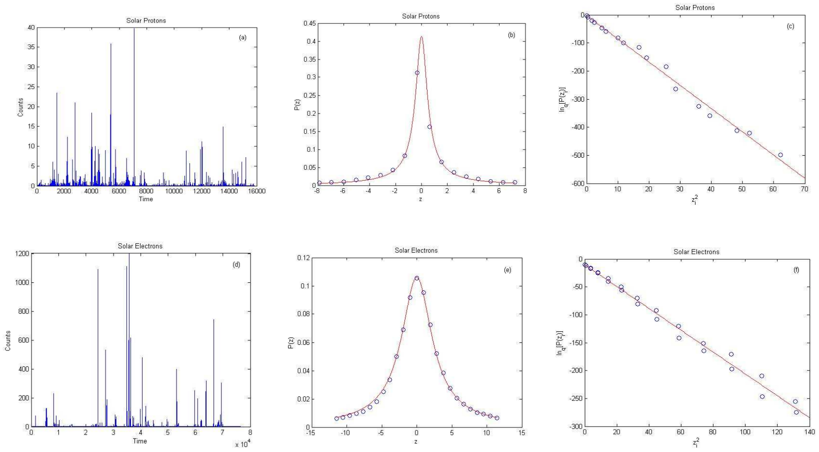

Figure 9: (a) Time series of Solar proton **(b)** PDF $P(z_i)$ vs. z_i q Guassian function that fits $P(z_i)$ for the Solar proton data **(c)** Linear Correlation between $\ln_q P(z_i)$ and $(z_i)^2$ where q = 2.31 ± 0.13 for the Solar proton **(d)** Time series of Solar electrons **(e)** PDF $P(z_i)$ vs. z_i q Guassian function that fits $P(z_i)$ for the Solar electrons **(f)** Linear Correlation between $\ln_q P(z_i)$ and $(z_i)^2$ where q = 2.13 ± 0.06 for the Solar electrons.

4.11 Cosmic Stars

In the following we study the q-statistics for cosmic star brightness. For this we used a set of measurements of the light curve (time variation of the intensity) of the variable white dwarf star PG1159-035 during March 1989. It was recorded by the Whole Earth Telescope (a coordinated group of telescopes distributed around the earth that permits the continuous observation of an astronomical object) and submitted by James Dixson and Don Winget of the Department of Astronomy and the McDonald Observatory of the University of Texas at Austin. The telescope is described in an article in The Astrophysical Journal (361), p. 309-317 (1990), and the measurements on PG1159-035 will be described in an article scheduled for the September 1 issue of the Astrophysical

Journal. The observations were made of PG1159-035 and a non-variable comparison star. A polynomial was fit to the light curve of the comparison star, and then this polynomial was used to normalize the PG1159-035 signal to remove changes due to varying extinction (light absorption) and differing telescope properties.

Figure 10 shows the estimation of q-statistics for the cosmic stars PG-1159-035. The q-values for the star PG-1159-035 time series was found to be $q_{stat} = 1.64 \pm 0.03$. We clearly observe non-Gaussian statistics.

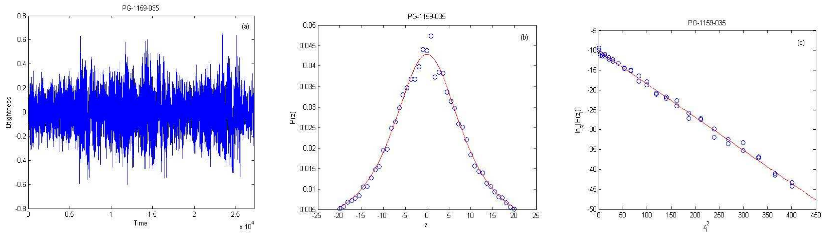

Figure 10: (a) Time series of cosmic star PG-1159-035 **(b)** PDF $P(z_i)$ vs. z_i q Guassian function that fits $P(z_i)$ for the cosmic star PG-1159-035 **(c)** Linear Correlation between $\ln_q P(z_i)$ and $(z_i)^2$ where q = 1.64 ± 0.03 for the cosmic star PG-1159-035.

4.12 Cosmic Rays

In this sub-section we study the q-statistics for the cosmic ray (carbon) data set. For this we used the data from the Cosmic Ray Isotope Spectrometer (CRIS) on the Advanced Composition Explorer (ACE) spacecraft and especially the carbon element (56-74 Mev) in hourly time period and time zone duration from 2000 – 2011.The cosmic rays data set is presented in Fig.11a, while the q-statistics is presented in Fig.11[b,c]. The estimated q_{stat} value was found to he $q_{stat} = 1.44 \pm 0.05$. This resulted reveals clearly non-Gaussian statistics for the cosmic rays data.

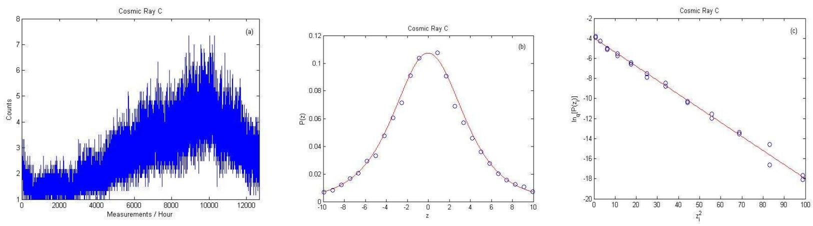

Figure 11: (a) Time series of cosmic ray Carbon **(b)** PDF $P(z_i)$ vs. z_i q Guassian function that fits $P(z_i)$ for the cosmic ray Carbon **(c)** Linear Correlation between $\ln_q P(z_i)$ and $(z_i)^2$ where q = 1.44 ± 0.05 for the cosmic ray Carbon.

System	q_stat
Cardiac (hrv)	1.26 ± 0.10
Brain (seizure)	1.63 ± 0.14
Seismic (Interevent)	2.28 ± 0.12
Seismic (Magnitude)	1.77 ± 0.09
Atmosphere (Temperature)	1.89 ± 0.08
Atmosphere (Rainfall)	2.21 ± 0.06
Magnetosphere (Bz storm)	2.05 ± 0.04
Magnetosphere (Vx storm)	1.98 ± 0.06
Magnetosphere (Ey storm)	2.49 ± 0.07
Magnetosphere (Electrons storm)	2.15 ± 0.07
Magnetosphere (Protons storm)	2.49 ± 0.05
Solar Wind (Bz cloud)	2.02 ± 0.04
Solar (Sunspot Index)	1.53 ± 0.04
Solar (Flares Index)	1.8700
Solar (Protons)	2.31 ± 0.13
Solar (Electrons)	2.13 ± 0.06
Cosmic Stars (Brigthness)	1.64 ± 0.03
Cosmic Ray (C)	1.44 ± 0.05

TABLE 1: This table includes the estimated qstat indeces for the brain and heart activity, the Magnetospheric dynamics (Bz, Vx, Ey, electron, protons time series), solar wind magnetic cloud, sunspot-solar flare time series, cosmic stars and cosmic rays

5. Summary and Discussion

In this study we presented novel theoretical concepts (sections 2-3) and novel experimental results (section 4) concerning the non-equilibrium distributed dynamics of various kinds of complex systems as : brain and heart activity, seismic and atmospheric dynamics as well as space plasmas dynamics corresponding to planetic magnetospheres, solar wind, solar corona, solar convection zone, cosmic stars and cosmic rays. In all of these cases the statistics was found to be non-Gaussian as the q-statistics index was estimated to be larger than the value q=1 which corresponds to Gaussian dynamics. The values of qstat index for the systems which were studied are presented in table 1. This experimental result constitutes strong evidence for the universality of non-equilibrium complex or strange dynamics as it was presented in section 2

of this study. As for the theory in the theoretical description of this study we have shown the theoretical coupling of Tsallis non-extensive statistical theory and the non-equilibrium fractal dynamics. That is has been shown also the internal correlation of the Tsallis q-extension of Boltzmann-Gibbs statistics with modern fractal generalization of dynamics. Our theoretical descriptions showed the possibility of the experimental testing of Tsallis statistics and fractal dynamics through the Tsallis q-triplet as well as the structure functions exponent spectrum. Moreover at this study we have tested the theoretical concepts only through the q-statistics index of Tsallis non extensive theory, the tests of the entire q-triplet and the structure functions exponent spectrum are going to be presented in a short coming paper [37].
Finally the theoretical concepts and the experimental results of this study clearly indicate the faithful character of the universality of Tsallis q-statistics and fractal dynamics in a plenty of different physical systems. In this way we can indicate faithfully that the Tsallis q-entropy theory as well as the fractal dynamics constitutes the new basis for a novel unification of the complexity physical theory.

References

1. Prigozine I., (1977), Time, structure and fluctuations, Nobel Lecture.; Prigozine I., (1996), El fin de las certitumbres, Editions Odile Jakob
2. Nicolis, G. & Prigogine, I. [1971], Fluctuations in nonequilibrium systems" Proc. Nat. Acad. Sci. 68x, p. 2102.; Nicolis, G. & Prigogine, I. [1977], Self-organization in nonequilibrium systems: From dissipative structures to order through uctuations", Willey, New York.; Nicolis, G. [1979] "Irreversible thermodynamics", Rep. Prog. Phys., 42, p. 225.; Nicolis, G. [1986] "Dissipative Systems", Rep. Prog. Phys., 49, p. 873.; Nicolis, G. [1989] "Physics of Far-From-Equilibrium Systems and Selforganisation", in Davies, Cambridge University Press.; Nicolis, G. & Prigogine, I. [1989] "Exploring Complexity: An Introduction", eds. Freeman, W.H., San Francisco.
3. Davies, P., The cosmic blueprint, Unwin Paperbacks, 1987.
4. El Naschie, M.S. [1998] "Superstrings, Knots, and Noncommutative Geometry in E(in_nity) Space", Int. Journal of Theoretical Physics, 37, p. 2935.; El Naschie, M.S. [2004] "A review of E in_nity theory and the mass spectrum of high energy particle physics", Chaos, Solitons & Fractals, 19, p. 209-236.; El Naschie, M.S. [2005] "Einstein's dream and fractal geometry", Chaos, Solitons & Fractals, 24, p. 1.; El Naschie, M.S. [2006] "Elementary prerequisites for E-in_nity (Recommended background readings in nonlinear dynamics, geometry and topology)", Chaos, Solitons & Fractals, 30, p. 579.
5. Iovane, G., Cantorian spacetime and Hilbert space: Part I – Foundations, Chaos, Solitons and Fractals, 28, 857-878, 2006.; Iovane, G., Cantorian spacetime and Hilbert space: Part II – Relevant consequences, Chaos, Solitons and Fractals, 29, 1-22, 2006.
6. Nottale, L. [1993] "Fractal Space-Time and Micro-physics", Towards a Theory of Scale Relativity, eds. World Scientific.; Nottale, L. [1994] "Scale Relativity, Fractal Space-time and Quantum Mechanics", Chaos, Solitons & Fractals, 4, p. 361.;

Nottale, L. [1996] "Scale Relativity and Fractal Space-Time: Applications to Quantum Physics, Cosmology and Chaotic Systems", Chaos, Solitons & Fractals, 7, p. 877.; Nottale L., The Theory of Scale Relativity: Non-Differentiable Geometry and Fractal Space-Time, Aip Conference Proceedings 2004, 718(20), p.68-95.; Nottale L., (2006), Fractal space – time, non – differentiable and scale relativity, Invited contribution for the Jubilee of Benoit mandelbrot.

7. Castro, C. [2005] ", On non-extensive statistics, chaos and fractal strings", Physica A 347, p. 184.
8. Bohr, N., Dialectica 1, 312, 1948.
9. Khrenninov, A., Classical and Quantum Mechanics of Information Spaces with Applications to Cognitive, Physhological, Social, and Anomalous Phenomena, Foundations of Physics, 29 (7), 1999.
10. Kroger, H., Why are probabilistic laws governing quantum mechanics and neurobiology?, Chaos, Solitons and Fractals, 25, 815-834, 2005.
11. Pezzaglia, W.W., Dimensionally Democratic Calculus and Principles of Polydimensional Physics, arxiv: gr-qc/9912025v1, 1999.
12. Tarasov, V.E., Fractional Liouville and BBGKI Equations, Journal of Physics: Conferences Series 7, 17-33, 2005.; Tarasov, V.E., Electromagnetic Fields on fractals, Modern Physics Letters, A 21, 1587-1600, 2006.; Tarasov, V.E., Fractional Variations for dynamical systems: Hamilton and Lagrange approaches, J. of Phys. A: Math. Gen., 39, 8409-8425, 2006.; Tarasov, V.E., Fractional vector calculus and fractional Maxwell's equations, Annals of Physics, 323, 2756-2778, 2008.
13. El-Nabulsi, A.R., A Fractional Approach to Nonconservative Lagrangian Dynamical Systems, FIZIKA A, 14, 289-298, 2005.; El-Nabulsi, A.R., Necessary optimality conditions for fractional action-like integrals of variational calculus with Riemann-Liouville derivatives of order (α, β), Math. Meth. Appl. Sci., 30, 1931-1939, 2007.; El-Nabulsi, A.R., Fractional dynamics, fractional weak bosons masses and physics beyond the standard model, Chaos, Solitons and Fractals, 41, 2262-2270, 2009.; El-Nabulsi, A.R., Fractional action-like variational problems in holonomic, non-holonomic and semi-holonomic constrained and dissipative dynamical systems, Chaos, Solitons and Fractals, 42, 52-61, 2009.
14. Cresson, J., Non-differentiable variational principles, J. Math. Anal. Appl., 307, 48-64, 2005.; Cresson, J. and Greff, I., Non-differentiable embedding of Lagrangian systems and partial differential equations, J. Math. Anal. Appl., 384, 626-646, 2011.
15. Goldfain, E., Fractional dynamics, Cantorian space-time and the gauge hierarchy problem, Chaos, Solitons and Fractals, 22, 513-520, 2004.; Goldfain, E., Complex Dynamics and the High-energy Regime of Quantum Field Theory, Int. J. of Nonlinear Sciences and Numerical Simulation, 6(3), 223-234, 2005.; Goldfain, E., Chaotic Dynamics of the Renormalization Group Flow and Standard Model Parameters, Int. J. of Nonlinear Science, 3, 170-180, 2007.; Goldfain, E., Fractional dynamics and the TeV regime of field theory, Communications in Nonlinear Science and Numerical Simulation, 13, 666-676, 2008.
16. Pavlos, G.P., Sarris, E.T., Paschalidis, N., The growth rate and location of the acceleration of energetic particles inside the plasma sheet, *Planetary and Space Science*, Vol. 37, issue 5, pp. 503-516, May 1989.; Pavlos, G.P., Sarris, E.T., Encounter with a source of energetic particles inside the plasma sheet, *Annales Geophysicae*, Vol. 7, pp. 531-539, October 1989.; Pavlos, G.P., Kyriakou, G.A., Rigas, A.G., Liatsis, P., Trochoutsos, P.C., Tsonis, A.A., Evidence for strange

attractor structures in space plasmas, *Annales Geophysicae*, Vol. 10, No. 5, pp. 309-322, May 1992.; Pavlos, G.P., Dialettis, D., Kyriakou, G.A., Sarris, E.T., A preliminary low-dimensional Chaotic Analysis of the solar Cycle, *Annales Geophysicae*, Vol. 10, No. 10, pp. 759-762, October 1992.; Pavlos, G.P., Rigas, A.G., Dialettis, D., Sarris, E.T., Karakatsanis, L.P., Tsonis T.T., Evidence for chaotic dynamics in the outer solar plasma and the earth magnetosphere, *Chaotic Dynamics: Theory and Practice*, NATO ASI Series B: Physics, Vol. 298, pp. 327-339, November 1992.; Pavlos, G.P., Karakatsanis, L.P., Latousakis, I., Dialettis, D., Papaioannou, G., Chaotic analysis of a time series composed by seismic events recorded in Japan, *International Journal of Bifurcation and Chaos*, Vol. 4, issue 1, pp. 87-98, February 1994.; Pavlos, G.P., Diamantidis, D., Adamopoulos, A., Rigas, A.G., Daglis, I.A., Sarris, E.T., Chaos and magnetospheric dynamics, *Nonlinear Processes in Geophysics*, Vol. 1, No. 2/3, pp. 124-135, 1994.; Pavlos, G.P., Athanasiou, M., Kugiumtzis, D., Hatzigeorgiu, N., Rigas, A.G., Sarris, E.T., Nonlinear analysis of Magnetospheric data, Part I. Geometric characteristics of the AE index time series and comparison with nonlinear surrogate data, *Nonlinear Processes in Geophysics*, Vol. 6, No. 1, pp. 51-65, 1999a.; Pavlos, G.P., Kugiumtzis, D., Athanasiou, M., Hatzigeorgiu, N., Diamantidis, D., Sarris, E.T., Nonlinear analysis of Magnetospheric data, Part II. Dynamical characteristics of the AE index time series and comparison with nonlinear surrogate data, *Nonlinear Processes in Geophysics*, Vol. 6, No. 2, pp. 79-98, 1999b.; Pavlos, G.P., Athanasiou, M., Diamantidis, D., Rigas, A.G., Sarris, E.T., Comments and new results about the magnetospheric chaos hypothesis, *Nonlinear Processes in Geophysics*, Vol. 6, No. 2, pp. 99-127, 1999c.

17. Iliopoulos, A., Pavlos, G. & Athanasiu, M. [2008], Spatiotemporal Chaos into the Hellenic Seismogenesis: Evidence for a Global Strange Attractor, Nonlin. Phenom. Complex Sys. 11(2), p. 274.; Iliopoulos, A. & Pavlos, G. [2010], Global Low Dimensional Seismic Chaos in the Hellenic Region," Intern. J. Bifurc. Chaos 20(7), p. 2071.
18. Sparrow, C., The Lorenz Equations, Bifurcations, Chaos and Strange Attractors, Springer, 1982.
19. Quantitative Universality for a Class of Nonlinear Transformations, Journal of Statistical Physics, 19, 25-52, 1978.
20. Libchaber, A., Experimental Study of Hydrodynamic Instabilites. Rayleigh-Bernard Experiment: Helium in a Small Box, Nonlinear Phenomena at Phase Transitions and Instabilities, eds. Riste, T., 259, Plenum, 1982.
21. Nelson, E. [1966], Derivation of the Schrodinger equation from Newtonian mechanics, Phys. Rev., 150, p. 1079.; Nelson, E. [1985], Quantum Fluctuations, Princeton University Press, New York.
22. Hooft, G.T. [1999] "Quantum gravity as a dissipative deterministic system", Class. Quantum Grav., 16, p. 3263-3279.; Hooft, G.T. [2001a] "Determinism and Dissipation in Quantum Gravity", Basics and highlights in fundamental physics: proceedings of the International School of Subnuclear Physics, 37, p. 397.; Hooft, G.T. [2001b] "How Does God Play Dice?(Pre) Determinism at the Planck Scale", An Essay in Honor of John S. Bell, arXiv:hep-th/0104219.
23. Parisi G. And Ramanurti S., Statistical Field Theory, Physics Today, vol. 41, issue 12, p. 110, 1988.

24. Beck, C. [1991] "Higher correlation functions of chaotic dynamical systems-a graph theoretical approach", Nonlinearity, 4, p. 1131.; Beck C. and Schlogl F. (1993), Thermodynamics of chaotic systems an introduction, Cambridge University Press.; Beck C., (1994), From the Perron-Frobenius equation to the Fokker-Planck equation, Journal of Statistical Physics, 79, 5-6, 875-894; Beck, C. [1995] "Chaotic quantization of field theories", Nonlinearity, 8, p. 423.; Beck, C. [2001] "Dynamical Foundations of Nonextensive Statistical Mechanics", Phys. Rev. Let., 87, p. 1806011.; Beck, C. [2002] "Nonextensive methods in turbulence and particle physics", Physica A, 305, p. 209.
25. Jensen, R.V., Functional Integral Approach to Classical Statistical Dynamics, Journal of Statistical Physics, 25(2), 183, 1981.
26. Ord, G.N. [1983], Fractal space-time: a geometric analogue of relativistic quantum mechanics, J. Phys. A: Math. Gen., 16, p. 1869.
27. Nigmatullin RR, (1991), Fractional integral and its physical interpretation, Theoretical and Mathematical Physics, 90, 3, 242-251.
28. Aristotle, The Physics, eds. Wicksteed, P.H. and Cornford, F.M., books I-IV, Loeb Classical Library, 1957.
29. Tsallis C., (1988), Possible generalization of Boltzmann-Gibbs statistics, Journal of Statistical Physics, 52,1-2, 479-487.; Tsallis C., (2001), Nonextensive statistical mechanics and thermodynamics: Historical Background and present status, Springer, S.Abe and Y. Okamoto (Eds.):LNP 560, 3-98.; Tsallis C. (2004), Nonextensive statistical mechanics: construction and physical interpretation, Nonextensive entropy – interdisciplinary applications Ed. Murray GM and Tsallis C., Oxford Univ. Press, 1-53; Tsallis C. (2009), Introduction to Non-extensive Statistical Mechanics, Springer.
30. Zelenyi, L. M. & Milovanov, A. V., Fractal Properties of Sunspots, Soviet Astronomy Letters, 17, p. 425, 1991.; b) Zelenyi, L. M. & Milovanov, A. V., Fractal topology and strange kinetics: from percolation theory to problems in cosmic electrodynamics, Pysics-Uspekhi, 47(8), 749-788, 2004.; Zelenyi, L.M., Malova, H.V., Artemyev, A.V., Popov, V.Yu. and Petrukovich, A.A., Thin Current Sheets in Collisionless Plasma: Equilibrium structure, Plasma Instabilities, and Particle Acceleration, Plasma Physics Reports, 37(2), 118-160, 2011.
31. Chang, T., VVedensky, D.D. and Nicoll, J.F., Differential Renormalization-Group Generators for Static and Dynamic Critical Phenomena, Physics Reports, 217(6), 279-360, 1992. Chang, T. [1992] "Low-Dimensional Behavior and Symmetry Braking of Stochastic Systems near Criticality Can these Effects be observed in Space and in the Laboratory", IEEE, 20(6), p. 691-694.; Chang, T., Self-Organized Criticality, multi-fractal spectra, sporadic localized reconnections and intermittent turbulence in the magnetotail, Physics of Plasmas, 6, (1999), 4137.; Chang et al, (2004), Complexity induced anisotropic bimodal intermittent turbulence in space plasmas, Phys. Plasmas 11, 1287.; Chang, T., Tam, S.W.Y., Wu, C-C, & Consolini, G [2003] "Complexity, Forced and/or Self-Organized Criticality, and Topological Phase Transitions in Space Plasmas", Space Sci. Rev., 107, p. 425-445.; Chang, T., Tam, S.W.Y. and Wu, C.-C., Complexity induced anisotropic bimodal intermittent turbulence in space plasmas, Physics of Plasmas, 11(4), 1287, 2004.; Chang, T., Tam, S.W.Y. and Wu, C.-C., Complexity and intermittent turbulence in space plasmas, (eds.) Sharma, A.S. and Kaw, P.K., Nonequilibrium Phenomena in Plasmas, 23-50, 2005.

32. Milovanov, A.V. and Zelenyi, L.M., Functional background of the Tsallis entropy: “coarse-grained” systems and “kappa” distribution functions, Nonlinear Processes in Geophysics, 7, 211-221, 2000.; Milovanov, A.V. and Rasmusse, J.J., Fractional generalization of the Ginzburg-Landaou equation: an unconventional approach to critical phenomena in complex media, Physics Letters A377, 75-80, 2005.; Milovanov, A.V., Dynamic Polarization random walk model and fishbone-like instability for self-organized critical systems, New Journal of Physics, 13, 043034, 2011.
33. Ruzmaikin A.A. (1985), Solar Phys. 100, 125-140.; Ruzmakin AA et al, (1996), Spectral Properties of Solar Convection and Diffusion, ApJ, 471, 1022.
34. Sharma, A.S., Baker, D.N. and Borovsky, J.E., Nonequilibrium phenomena in the magnetosphere, (eds.) Sharma, A.S. and Kaw, P.K., Nonequilibrium Phenomena in Plasmas, 3-22, 2005.; Sharma, A.S., Ukhorski, A.Y. and Sitnov, M.I., Global and multiscale phenomena of the magnetosphere, (eds.) Sharma, A.S. and Kaw, P.K., Nonequilibrium Phenomena in Plasmas, 117-144, 2005.
35. Consolini, G. et al., Multifractal Structure of Auroral Electrojet Index Data, Phys. Rev. Lett. 76, 4082–4085, 1996.; Consolini, G., [1997] "Sandpile cellular automata and magnetospheric dynamics", 8th GIFCO Conference: Cosmic physics in the year 2000, p. 123 - 126.; Consolini G., and Chang T., Magnetic Field Topology and Criticality in Geotail Dynamics: Relevance to Substorm Phenomena, Space Sc. Rev., 95, 309-321, 2001.; Consolini G. et al., On the magnetic field fluctuations during magnetospheric tail current disruption: A statistical approach, J. Geoph. Research, 110, A07202, 2005.
36. Abramenko, V.I., Solar MHD turbulence in regions with various levels of flare activity, Astronomy Reports, Volume 46, Number 2, 161-171, 2002.
37. Pavlos G.P., et al., First and second order non-equilibrium phase transition and evidence for non-extensive Tsallis statistics in Earth’s magnetosphere, Physica A, 390, 2819-2839, 2011.; Pavlos, G.P., Karakatsanis, L.P. and Xenakis, M.N., Tsallis non-extensive statistics, intermittent turbulence, SOC and chaos in the solar plasma. Part one: Sunspot dynamics, Submitted for Publications, http://arxiv.org/abs/1201.6498, 2012.; Pavlos, G.P., Karakatsanis, L.P. and Xenakis, M.N., Sarafopoulos, D. and Pavlos, E.G., Tsallis Statistics and Magnetospheric Self-organization, Physica A, 393, 3069-3080, 2012.
38. Zaslavsky, G.M., Renormalization group theory of anomalous transport in systems with Hamiltoniasn chaos, Chaos 4(1), 25, 1994.; Zaslavsky, G.M., Fractional kinetc equation for Hamiltonian chaos, Physics D 76, 110-122, 1994.; Zaslavsky, G.M., Chaotic dynamics and the origin of statistical laws, American Institute of Physics, S-0031-9228-9908-030-8, 1999.; Zaslavsky, G.M., Chaos, fractional kinetics, and anomalous transport, Physics Reports, 371, 461–580, 2002.
39. Chen W., (2006), Time – space fabric underlying anomalous diffusion, Chaos, Solitons & Fractals, 28 (4), 923–929.
40. Wilson, K.G., The renormalization group: Critical phenomena and the Kondo problem, Reviews of Modern Physics, 47(4), 773, 1975.; Wilson, K.G., The renormalization group and critical phenomena, Reviews of Modern Physics, 55(3), 583, 1983.
41. Binney, J.J., et al., The Theory of Critical Phenomena An introduction to the Renormalization Group, Oxford University Press, 1992.

42. Kogut, J.B., An introduction to lattice gauge theory and spin systems, /review of Modern Physics, 51(4), 659, 1979.
43. Ivancevic, V. and Ivancevic, T.T., Complex Nonlinearity, Chaos, Phase Transitions, Topology Change and Path Integrals, Springer, 2008.
44. Biro, T., Muller, B. & Matinyan, S. [2004] "Chaotic Quantization: Maybe the Lord plays dice, after all?", Lecture Notes in Physics, 633, p. 164.
45. Krommes J.A., Systematic statistical theories of plasma turbulence and intermittency: current status and future prospects, Physics Reports 283, 5-48, 1997.; Krommes J.A., Fundamental statistical descriptions of plasma turbulence in magnetic fields, Physics Reports, 360, 1-352, 2002.
46. Lui A.T.Y., Multiscale phenomena in the near-Earth magnetosphere, Journal of Atmospheric and Solar-Terrestial Physics, 64, 125-143, 2002.
47. Svozil, K. and Zeilinger, A., Dimension of space-time, International Journal of Modern Physics A, Volume 1(4), 971-990, 1986.
48. Antoniadis I, (1998), Fractal geometry of quantum space-time at large scales, Physics Letters B, 444, 284-292.
49. Agop, M. et al., El Naschies's $\varepsilon^{(\infty)}$ space-time, hydrodynamics model of scale relativity theory and some applications, Chaos, Solitons and Fractals, 34, 1704-1723, 2007.
50. Altaisky, M.V. and Sidharth, B.G., p-Adic Physics Below and Above Planck Scales, Chaos, Solitons and Fractals, 10, 167-176, 1999.
51. Lizzi, F., The structure of Spacetime and Noncommutative Geometry, http://arxiv.org/abs/0811.0268, 2002.
52. Majid, S., Quantum groups and noncommutative geometry, Journal of Mathematical Physics, 41(6), 3892, 2000.
53. Ren, F.Y., Liang, J.R., Wang, X.T. and Qio, W.Y., Integrals and derivatives on net fractals, Chaos, Solitons and Fractals, 16, 107-117, 2003
54. Balescu R, (1975), Equilibrium and non-equilibrium statistical mechanicsm, A Wiley Inter. Publ.
55. Burlaga, L.F. and Vinas, A.F., Triangle for the entropic index *q* of non-extensive statistical mechanics observed by Voyager 1 in the distant heliosphere, Physica A, 356, 375-384, 2005.
56. Ferri G.L., Reynoso Savio M.F., Plastino A., "Tsallis q-triplet and the ozone layer", Physica A, 389, p. 1829-1833, 2010.
57. Temam, R., Infinite-Dimensional Dynamical Systems in Mechanics and Physics, Springer, 1988.
58. Carbone, V., Veltri, P. and Bruno, R., Solar wind low-frequency magnetohydrodynamic turbulence: extended self-similarity and scaling laws, Nonlinear Process in Geophysics, 3, 247-261, 1996.
59. Kovas, A.L. [1994] "Nonlinear Dynamics of Spatio-Temporal Processes in Complex Systems", Mathl. Comput. Modelling, 19, p. 47.
60. Mikhailov, A.S. and Loskutov, A.Yu., Foundations of Synergetic II Complex Patterns, Springer, 1991.
61. Voros, Z., On multifractality of high-latitude geomagnetic fluctuations, Ann. Geophysicae, 18, 1273-1282, 2000.; Voros, Z. et al., Multi-scale magnetic field intermittence in the plasma sheet, Annales Geophysicae, 21, 1995, 2003.; Voros, Z.

et al., Magnetic turbulence in the plasma sheet, Journal of Geophysical Research, 109, A11215, 2004.

62. Leubner, M.P. and Voros, Z., A nonextensive entropy approach to solar wind turbulence, The Astrophysical Journal, 618, 547-555, 2005.; Leubner, M.P. and Voros, Z., A nonextensive entropy path to probability distributions in solar wind turbulence, Nonlinear Processes in Geophysics, 12, 171-180, 2005.
63. Dudok de Wit, T. and Krasnosel'skikh, V.V., Non-Gaussian statistics in space plasma turbulence: fractal properties and pitfalls, Nonlinear Processes in Geophysics, 3, 262-273, 1996.
64. Karakatsanis, L.P. & Pavlos, G.P. [2008] "Self Organized Criticality and Chaos into the Solar Activity", Nonlinear Phenomena in Complex Systems, 11(2), p. 280-284; Karakatsanis, L.P., Pavlos, G.P., Iliopoulos, A.C., Tsoutsouras, V.G. & Pavlos E.G. [2011] "Evidence for Coexistence of SOC, Intermittent Turbulence and Low-Dimensional Chaos Processes in Solar Flare Dynamics", Modern Challenges in nonlinear plasma physics: A Festschrift Honoring the Career of Dennis Papadopoulos, AIP, 1320, p.55-64.
65. Born, M., Natural Philosophy of Cause and Chance, Oxford University Press, 1948.
66. YankovVV, (1997), Three rules of nonlinear physics, Physics Reports, 283, 147-160.
67. Hohenberg, P.C. and Halperin, B.I., Theory of dynamics critical phenomena, Reviews of Modern Physics, 49(3), 435, 1977.; Hohenberg, P.C. & Shraiman, B.I. [1989] "Chaotic behavior of an extended system", Physica D, 37, p. 109-115.
68. Elderfield, D., On the resolution of ordering ambiguities associated with the path integral representation of stochastic process, J. Phys. A: Math. Gen., 18, L767-L771, 1985.
69. Haken, H. [1983] Synergetics: Introduction and Advanced Topics, Springer.
70. Kubo R. et al, (1998), Statistical Physics II: Non equilibrium statistical mechanics, Springer.
71. Lenzi et al, (2000), Statistical mechanics based on Renyi entropy, Physica A, 280 (3–4), 337–345.
72. Robledo A., (2004), Unifying laws in multidisciplinary power-law phenomena: fixed –point universality and nonextensive entropy, Nonextensive entropy – interdisciplinary applications Ed. Murray GM and Tsallis C., Oxford Univ. Press, 63-77.
73. Halsey et al, (1986), Fractal measures and their singularities: the characterization of strange sets, Physical Review A, 33,2, 1141 – 1151.
74. Theiler J., Estimating fractal dimension, JOSA A, Vol. 7, Issue 6, pp. 1055-1073, 1990.
75. Paladin G. and Vulpiani A., (1987), Anomalous scaling laws in multifractal objects, Physics report, 156,4, 147 – 225.
76. Meneveau C. and K.R. Sreenivasan, The multifractal spectrum of the dissipation field in turbulent flows, Nuclear Physics B (Proc. Suppl.) 2 (1987) 49-76.; Meneveau C. and Sreenivasan KR, (1991), The multifractal spectrum of the dissipation field in turbulent flows, Nuclear Physics B,2, 49-76.
77. Umarov S. et al. (2007), A generalization of the central limit theorem concistent with non-extensive statistical mechanics, arxiv: cond-mat/0603593v4.

78. Arimitsu T. and N Arimitsu, Tsallis statistics and fully developed turbulence, (2000), J. Phys. A: Math. Gen. 33 L235 doi:10.1088/0305-4470/33/27/101.; Arimitsu T and Arimitsu A, (2001), Analysis of turbulence by statistics based on generalized entropies, Physica A, 295, 177 – 194.

79. Kolmogorov A., The Local Structure of Turbulence in Incompressible Viscous Fluid for Very Large Reynolds' Numbers, Doklady Akademiia Nauk SSSR, vol.30, p.301-305, 1941.

80. Shlesinger, M.F., Zaslavsky, G.M. and Klafter, J., Strange kinetics, Nature, 363, 31, 1993.

81. Moore, R.L., La Rosa, T.N. and Orwing, L.E., The wall of recconection-driven magnetohydrodynamics turbulence in a large solar flare, The Astrophysical Journal, 438, 985-996, 1995.

82. Rempel, E.L. and Chian A.C.-L., Space plasma dynamics: Alfven intermittent chaos, Advances in Space Research, 35, 951-960, 2005.

83. Marsch E. and Tu CY, (1997), Intermittency, non-Gaussian statistics and fractal scaling of MHD fluctuations in the solar wind, Nonlinear Processes in Geophysics 4, 2,101-124.

84. Feynman, R.P., Statistical Mechanics A set of lectures, The Benjamin/Cummings Publishing Company, INC., 1972.